Tidal Interactions in Composite Systems
M.-J. Goupil and J.-P. Zahn (eds)
EAS Publications Series, Vol. ?, 2007

PLANET–DISK INTERACTIONS

Frédéric S. Masset[1, 2]

Abstract. Tides come from the fact that different parts of a system do not fall in exactly the same way in a non-uniform gravity field. In the case of a protoplanetary disk perturbed by an orbiting, prograde protoplanet, the protoplanet tides raise a wake in the disk which causes the orbital elements of the planet to change over time. The most spectacular result of this process is a change in the protoplanet's semi-major axis, which can decrease by orders of magnitude on timescales shorter than the disk lifetime. This drift in the semi-major axis is called planetary migration, and is the most important aspect of planet–disk interactions. In this chapter, we first describe how the planet and disk exchange angular momentum and energy at the Lindblad and corotation resonances. Next we review the various types of planetary migration that have so far been contemplated: type I migration, which corresponds to low-mass planets (less than a few Earth masses) triggering a linear disk response; type II migration, which corresponds to massive planets (typically at least one Jupiter mass) that open up a gap in the disk; "runaway" or type III migration, which corresponds to sub-giant planets that orbit in massive disks; and stochastic or diffusive migration, which is the migration mode of low- or intermediate-mass planets embedded in turbulent disks. Third, we discuss questions linked to the planet eccentricity, in particular how the eccentricity is affected by the planet–disk interaction. Fourth, we discuss the various numerical schemes that have been used to describe planet–disk interactions. We discuss their strengths and weaknesses, and list the results that numerical simulations have achieved over the past decade.

1 Introduction

The importance of the tidal interaction between a protoplanetary disk and a forming planet was first recognized long before the discovery of the first extrasolar

[1] Service d'Astrophysique, Orme des Merisiers, CE-Saclay, 91191 Gif/Yvette Cedex, France, `fmasset@cea.fr`
[2] Instituto de Astronomía, Ciudad Universitaria, Apartado Postal 70-264, Mexico D.F. CP 04510, Mexico

DOI: (will be inserted later)

planet in 1995. Goldreich and Tremaine (1980) discussed the case of Jupiter in a conservative protoplanetary nebula, and found that its semi-major axis should evolve as a result of the gravitational interaction between the planet and the nebula (although they could not determine whether it should increase or decrease). This evolution occurred on a timescale of only $O(10^4)$ yrs, which is extremely short compared to the lifetime of the nebula. Up until the late nineties, the problem of tidal interaction between a low-mass planet and a protoplanetary disk was tackled through analytic torque estimates. The first step in such works consisted of determining the torque between a differentially rotating disk and an external potential, at either a Lindblad resonance or the corotation resonance (Goldreich and Tremaine, 1979). These torque expressions were used as building blocks to give a finely tuned estimate of the tidal torque acting on a protoplanet. In particular, Ward (1986) showed that objects of planetary mass experience a negative torque, which causes their orbit to decay towards the central object on timescales that are short compared to the disk lifetime. Since then, there have been considerable refinements to the initial tidal torque expression. The most up-to-date estimate is that of Tanaka et al. (2002): an expression for the tidal torque, valid in the linear regime, that takes into account both the Lindblad and corotation torques in a three-dimensional, locally isothermal disk.

When the first extrasolar planet was discovered orbiting 51 Peg with a period of 4.23 days (Mayor et al., 1995) at a distance of only 0.052 AU from the central star, theories of orbital migration received renewed attention. None of the reasonable planetary formation scenarios was able to account for the formation of a planetary core that close to the star. It therefore appeared likely that this planet had formed farther out in the protoplanetary disk and then migrated towards the star, along the lines of predictions made by the theoretical work of the eighties (Lin et al., 1996).

Had any doubted that significant planetary migration is common in forming planetary systems, additional clues were provided by the discovery of planetary systems exhibiting low-order mean motion resonance. The most prominent example of this is the system GJ 876, where the two planets have orbital periods of roughly 30 and 60 days. A similar 2 : 1 mean motion resonance has been found in several other multiple planetary systems. [1] Under the effect of differential migration (i.e., the outer planet migrates inwards faster than the inner one), two planets can converge and be captured in a low-order mean motion resonance.

The present chapter is organized as follows:

- In section 3, we present torque expressions for the Lindblad resonances and corotation resonance in some detail. As several derivations of these expressions already exist in the literature, the exercise is not repeated here. Rather, we emphasize and illustrate the properties of these resonances so as to give the reader some insight into the physical meaning of the torque expression.

[1] See the Extrasolar Planets Encyclopedia at `http://exoplanet.eu` for an up-to-date catalog of candidate extrasolar planets.

- In section 4, we list the different migration modes that have been envisaged so far. In section 4.1 we use the torque expressions of section 3 to characterize the migration of low-mass planets in a non-turbulent disk (also called type I migration). In this section we also explain why inward migration is almost unavoidable, even for surface density profiles that would seem at first glance to favor an outward migration. We also address the question of a planetary mass threshold, under which the disk response can be considered linear. In section 4.2 we study the disk response in the strongly non-linear regime, and see how a giant planet can alter the disk surface density profile by opening a gap. Its subsequent migration in the split disk differs markedly from type I migration. We describe the properties of this kind of migration, which is called type II migration, and stress some pertinent open questions. In section 4.3 we present a recently discovered migration mode of sub-giant planets in massive disks, which is based upon the action of the co-orbital corotation torque. Under some circumstances that we shall specify, such objects can undergo a runaway migration either inwards or outwards. This type of migration is therefore simply called "runaway migration", and is also sometimes referred to as type III migration. Finally, in section 4.4 we present the mode called stochastic (or diffusive) migration, which was recently identified in intensive numerical calculations. This migration mode is relevant for planets of low or intermediate ($<\sim 30\,M_\oplus$) mass, embedded in regions of the protoplanetary disk invaded by MHD turbulence arising from the magnetorotational instability. This turbulence leads to large temporal fluctuations in the torque experienced by the planet, and as a result the planet's semi-major axis evolves according to a random walk rather than a monotonic decrease.

- In section 5 we give an overview of the angular momentum and energy exchange between a disk and an eccentric planet. In section 5.1 we see that in addition to the principal Lindblad and corotation resonances, there is another set of resonances at which the disk torque scales with e. These are the first-order Lindblad and corotation resonances, and they have an impact on the eccentricity evolution of the planet. In section 5.2 we use this result to estimate the timescale of eccentricity variation for a low-mass protoplanet. In section 5.3 we consider the case of a planet that opens a clear gap. In this case some resonances are inactive, and the eccentricity budget is affected. This leads us to discuss the fashionable open question of whether planet–disk interactions can be held responsible for the excitation of a giant planet's eccentricity, and therefore whether these interactions could account for the large eccentricities of many giant extrasolar planets. Finally, in section 5.4, we discuss how the type I migration of a low-mass object is affected if its orbit is eccentric.

- In section 6 we present the different families of numerical codes that have so far been employed to simulate the tidal interaction between a protoplanetary disk and a protoplanet. We briefly discuss the qualities and drawbacks of each type. In section 6.1 we give a list of results, both expected and unexpected, that numerical simulations have recently brought to our knowledge of planet–disk interactions. Finally, in section 6.2 we discuss a few more issues related to numerical simulations; either issues related to specific schemes, or those of a conceptual nature (namely, we address the ubiquitous neglect of the disk's self-gravity).

2 Prerequisites

2.1 General considerations regarding protoplanetary disks

In this short section we introduce only those few ideas regarding protoplanetary disks that will be needed in the following sections. The protoplanetary disks that we are interested in are those in the early stages of planetary system formation, corresponding to the T Tauri phase of the central object. They are massive disks (between 10^{-3} and 10^{-1} times the mass of the central star), and essentially gaseous. Their solid content, which is exclusively dust at early times, represents about 1 % of their mass. Their lifetimes typically range from 1 Myr to 10 Myr (Haisch et al., 2001), which sets an upper limit on any planet–disk interaction that may occur over the course of planetary formation. These disks are also quite thin: the pressure scale height H is only a few percent of the distance r from the central object at any given location: $H/r \sim 0.03 - 0.1$. This ratio is often called the *aspect ratio*, and denoted by h. Because they are so thin, these disks are almost Keplerian; the radial pressure gradient is small compared to the centrifugal force, so centrifugal balance is achieved at an angular velocity almost equal to the Keplerian value. The disk thickness is related to the gas sound speed c_s and gas orbital frequency Ω as $H = c_s/\Omega$. Some important frequencies associated with a differentially rotating disk are now given. $A = (1/2)rd\Omega/dr$ is the first Oort's constant, which scales with the amount of shear in the flow. This frequency is zero for a rigid body rotation. In a Keplerian disk, its value is $-(3/4)\Omega$. The second Oort's constant is defined as $B = (1/2r)d(r^2\Omega)/dr$; it is half of the vertical component of the flow vorticity. B also turns out to be $(2r)^{-1}$ times the radial derivative of the flow's specific angular momentum. In a Keplerian disk, its value is $\Omega/4$. Another local frequency is the epicyclic frequency κ, defined by $\kappa^2 = 4\Omega B$. This is the frequency at which an eccentric test particle describes an epicycle about its guiding center, which has a uniform circular trajectory. In a Keplerian disk, the degeneracy $\kappa = \Omega$ ensures that Keplerian orbits are closed. Another quantity that we shall frequently mention hereafter is the potential vorticity of the flow, also called the vortensity, which is the vertical component of the vorticity divided by the surface density.

A frequent approximation consists in using a locally isothermal equation of state for the gas. As a consequence, the shocks excited by planets orbiting in the disk are also considered to be isothermal. Another customary approximation consists of neglecting the disk self-gravity. Toomre's Q parameter (Toomre, 1969) is large in protoplanetary disks ($Q \gg 1$), which suggests that their self-gravity is unimportant. Later we shall discuss issues related to the disk self-gravity in the context of planetary migration, in sections 6.1.1, 6.2.5, and 6.2.6.

Protoplanetary disks are accretion disks, in which the radial transfer of angular momentum is ensured by turbulence (as we shall discuss in section 4.4). The effects of turbulence are often described by the use of Navier-Stokes equations with a finite kinematic shear viscosity ν. This parameter is assumed to depend on the local disk thickness and orbital frequency; the standard approach is to introduce a so-called α-parameterization (Shakura and Sunyaev, 1973): $\nu = \alpha H^2\Omega$, where α is a dimensionless parameter thought to range from 10^{-4} to 10^{-2} in protoplanetary disks.

2.2 Notation and units

In addition to the notation introduced in the previous section, throughout this manuscript we shall denote the disk's surface density by Σ, a planet's semi-major axis by a, its eccentricity by e, its mass by M_p, its orbital frequency by Ω_p, its orbital period by $T_0 = 2\pi/\Omega_p$, and the central object's mass by M_*. We denote by q the planet–star mass ratio M_p/M_*. The location of a fluid element is given by its distance r from the central object, its azimuth ϕ, and its colatitude θ. (ϕ and θ are defined in a spherical coordinate system whose polar axis is perpendicular to the disk's equatorial plane.) We will often assume that the surface density profile of the disk is a power law of the radius: $\Sigma(r) \propto r^{-\zeta}$. We denote by $m_D = \pi\Sigma(r)r^2$ the "local" disk mass, in the sense that this quantity depends on r. μ_D is defined as the ratio of the local disk mass to the mass of the central object: $\mu_D = m_D/M_*$. Whenever a planet's mass is expressed in terms of Earth or Jupiter masses, we assume the central object to have one solar mass.

In many numerical models it is customary to use the planet's initial semi-major axis as the length unit, the mass of the central object as the mass unit, and to choose a time unit such that the gravitational constant $G = 1$. This choice implies that the planet's orbital frequency is also equal to one, so its initial orbital period is 2π. In many cases, it is also customary to express time in terms of "planetary orbits". Although not explicitly stated, this measure is always the *initial* planetary orbital period. The actual number of orbits performed by the planet will differ if the planet migrates. We shall make use of this convention hereafter.

3 Disk torque at an isolated resonance

The gravitational potential of any tidal perturber can always be expressed as a series of azimuthally periodic components parameterized by m, the number of complete cycles in the domain $0 < \phi \leq 2\pi$, each component having a sinusoidal dependence on the azimuth. Hereafter, the expression "m-fold component" will refer to an individual term of this series. The total potential and each of its components rotate with a given pattern speed Ω, so each m-fold component can be written in the form

$$\Phi(r,\phi,\theta,t) = \Phi_m(r,\theta)\cos[m(\phi-\Omega t)+\varphi_m(r,\theta)]. \tag{3.1}$$

$\Phi_m(r,\theta)$ and $\varphi_m(r,\theta)$ are real functions of the radius and colatitude that represent respectively the amplitude and phase of the potential component as a function of r. If we consider the disk to be infinitely thin (the 2D approximation), we can discard the dependence on colatitude and write each component as

$$\Phi(r,\phi,t) = \Phi_m(r)\cos[m(\phi-\Omega t)+\varphi_m(r)]. \tag{3.2}$$

In the particular case of a planet on a fixed circular orbit, one would have $\varphi_m(r) \equiv 0$ and all the potential components would rotate along with the planet: $\Omega \equiv \Omega_p$. The problem of determining the torque between the perturber and the disk, in the linear regime, therefore amounts to determining the torque exerted on the disk by a uniformly rotating $m-$fold potential component. Goldreich and Tremaine (1979) have shown that angular momentum exchange between the perturber and the disk occurs only at the Lindblad and corotation resonances. Lindblad resonances correspond to locations in the disk where the perturber frequency in the matter frame ($\tilde{\omega}(r) = m[\Omega_p - \Omega(r)]$) matches $\pm\kappa(r)$ (the epicyclic frequency). The corotation resonance occurs where the perturber frequency is zero in the matter frame, that is to say at a radius where the disk material rotates along with the perturbing potential. We specify below the torque exerted by a given potential component at both kinds of resonance.

3.1 *Torque at a Lindblad resonance*

3.1.1 Torque expression

We do not re-derive here the expression for the torque at a Lindblad resonance, as it can be found in many places in the literature (Goldreich and Tremaine, 1979; Meyer-Vernet and Sicardy, 1987; Artymowicz, 1993b). Its expression is

$$\Gamma_m = -\frac{m\pi^2\Sigma}{rdD/dr}\left(r\frac{d\Phi_m}{dr}+\frac{2\Omega}{\Omega-\Omega_p}\Phi_m\right)^2, \tag{3.3}$$

where Γ_m is the torque exerted on the disk material by the perturber and $D = \kappa(r)^2 - m^2[\Omega(r)-\Omega_p]^2$ represents a distance to the resonance. In Eq. (3.3), the term in brackets and rdD/dr are both to be evaluated at the resonance location. In a Keplerian disk, rdD/dr is positive at the ILR (Inner Lindblad Resonance, where $\tilde{\omega} = -\kappa$) and negative at the OLR (Outer Lindblad Resonance, where $\tilde{\omega} = +\kappa$). The perturbing potential therefore exerts a negative torque on the disk at the ILR, and a positive torque at the OLR. Newton's third law thus implies that the disk exerts a positive (negative) torque on the perturber at the ILR (OLR).

One can make the following observations regarding Eq. (3.3):

- The torque scales with the disk surface density and the square of the perturbing potential. The latter dependency arises from the fact that $\Gamma_m =$

$\int_{\rm disk} \Sigma \frac{\partial \Phi_m}{\partial \varphi}$. Because only m-fold perturbations of the surface density contribute to the above integral, the integrand is a product of two terms which both scale with the perturbing potential.

- At the exact resonance location (i.e., $D = 0$), $(rdD/dr)^{-1}$ scales with the resonance width. The torque therefore also scales with the resonance width.
- Apart from the surface density and rotation velocity, no other physical quantity related to the disk (the sound speed, for instance) features in the torque expression. In fact, the torque value is independent of the physical processes at work in the disk (Meyer-Vernet and Sicardy, 1987). In the simplest case of a pressureless, inviscid disk without self-gravity, angular momentum exchange occurs at the Lindblad resonances and angular momentum accumulates at their exact locations. To achieve a steady state, some additional process must get rid of the angular momentum deposited at the resonance by the external perturber. Meyer-Vernet and Sicardy (1987) have shown that dissipation (which might be provided by a simple drag $-Q\vec{v}$, or by a shear or bulk viscosity), pressure effects or self-gravity can help the disk transfer angular momentum away from the resonance. This will allow a steady state to be achieved, and hence a torque value that is constant in time. Remarkably, the underlying physics modifies only the shape and width of the resonant region, not this torque value.

3.1.2 Lindblad resonance location

We now wish to define the location of the Lindblad resonances in a Keplerian disk. As stated previously, a Lindblad resonance is found where $\tilde{\omega} = \pm\kappa$ (the upper sign stands for the OLR, while the lower sign stands for the ILR). Using the fact that $\kappa = \Omega$ in a Keplerian disk, we obtain:

$$\Omega(r_{\rm LR}) = \frac{m}{m \pm 1}\Omega_p. \tag{3.4}$$

We can thus make the following observations:

- At a Lindblad resonance, the fluid elements are in mean motion resonance with the planet; the fluid elements complete $m \pm 1$ orbits around the central object while the planet completes m orbits.
- In a Keplerian disk the $m = 1$ potential component does not have an ILR, as the denominator of Eq. (3.4) is zero (lower sign).
- At the Outer (Inner) Lindblad Resonance, the disk material rotates slower (faster) than the perturbing potential. As $\Omega(r)$ is a decreasing function of r in a Keplerian disk, this indicates that the OLR lies outside the corotation radius r_c of the perturber (defined by $\Omega(r_c) = \Omega_p$), whereas the ILR lies inside that radius. This explains their names.

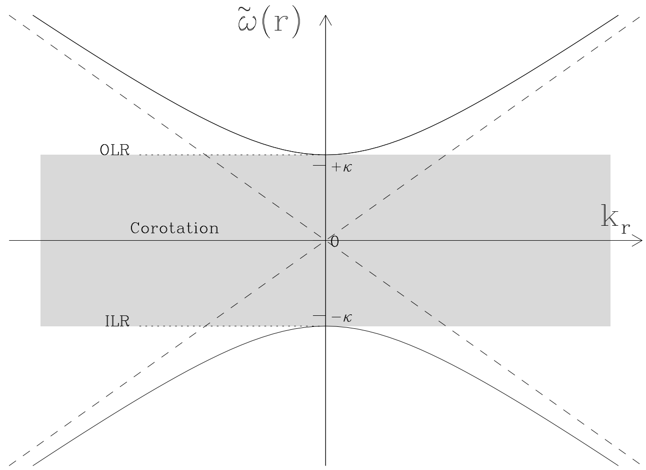

Fig. 1. A graphical representation of the dispersion relation given in Eq. (3.5). The $x-$axis represents the radial wave vector, while the $y-$axis represents the wave frequency in the matter frame. The latter is an increasing function of r, which is zero by definition at the corotation radius. The upper branch reaches a minimum at $\kappa(1+m^2c_s^2/\kappa^2r^2)^{1/2} = \kappa(1+m^2h^2)^{1/2}$, while the lower branch reaches a maximum at $-\kappa(1+m^2h^2)^{1/2}$. The dashed lines show the asymptotic dispersion relation for large k_r. It is the dispersion relation of acoustic waves, propagating inwards or outwards. The gray area shows the band where propagation is forbidden, centered on the corotation resonance.

3.1.3 The special case of a thin, non self-gravitating gaseous disk

Although the torque expression of Eq. (3.3) is independent of any physical processes that remove angular momentum from the resonance, it is instructive to look at the specific case in which pressure waves play this role, since this is the relevant process for protoplanetary disks. The dispersion relation for perturbations in such disks is

$$\tilde{\omega}^2 = \kappa^2 + c_s^2 k^2, \tag{3.5}$$

where k is the wave vector of the perturbations. Eq. (3.5) is represented graphically in Fig. 1. One can see that the waves do not propagate within a band centered on the corotation resonance and enclosing the Inner and Outer Lindblad Resonances. Another notable effect is that the waves cannot even reach the nominal Lindblad resonances located at $\tilde{\omega} = \pm\kappa$; the turnover points are located slightly farther out, since at the Lindblad resonances $k = 1/m$. This is a pressure effect, as the distance of the turning point from the resonance location is linked to the finite sound speed.

Eq. (3.5) implies that within the forbidden band, the radial wave vector is purely imaginary. This indicates that a disturbance in this band exhibits no winding, and decays exponentially over a length scale that depends on its distance from the corotation radius. At corotation, this length scale is equal to the disk height $H = c_s/\kappa$.

In Fig. 2 we show the disk response to a uniformly rotating $m = 3$ potential. This plot was obtained from hydrodynamical calculations for a Keplerian disk, with $h = 0.05$. The calculations were performed on a polar grid, hence the central hole[2]. In Fig 3, we show the amplitude and phase of the $m = 3$ disk response as a function of radius. These plots illustrate most of the features mentioned above, which are:

- The disk wave response is launched at the Lindblad resonances.
- The wave is evanescent in a band between the Lindblad resonances, centered on the corotation resonance.
- In the forbidden band the disturbance displays no winding.

3.2 *Torque at a corotation resonance*

The angular momentum exchange at a corotation resonance and a Lindblad resonance are due to different physical processes. In the latter case the perturbing potential tends to excite epicyclic motion, and (as we have seen in section 3.1.3) the angular momentum deposited is evacuated through pressure-supported waves. On the other hand, we have seen that these waves are evanescent in the corotation region and therefore unable to remove the angular momentum brought by the perturber (Goldreich and Tremaine, 1979).

The physical picture of the flow at a corotation resonance with azimuthal wavenumber m is characterized by a set of m eye-shaped libration islands in which fluid elements move along closed streamlines. These islands are depicted in Fig. 4. The streamlines of this figure were obtained from a numerical simulation of a disk with $h = 0.01$. They closely resemble the streamlines that one could sketch using the following approximation.

One can take the linearized fluid dynamics equations in the corotation region, discard all pressure effects and terms proportional to x (the distance from the corotation radius), and assume that the perturbing potential only depends on ϕ (i.e., that $\Phi(r, \phi, t) = \Phi_0 \cos\{m[\phi - \Omega(r_c)t]\}$, where r_c is the corotation radius). This yields the following expression for the perturbed radial velocity:

$$v_r = \frac{m\Phi_0}{2Br_c}\sin(m\phi'), \tag{3.6}$$

[2]The inner radius of the mesh is 0.4 in this case.

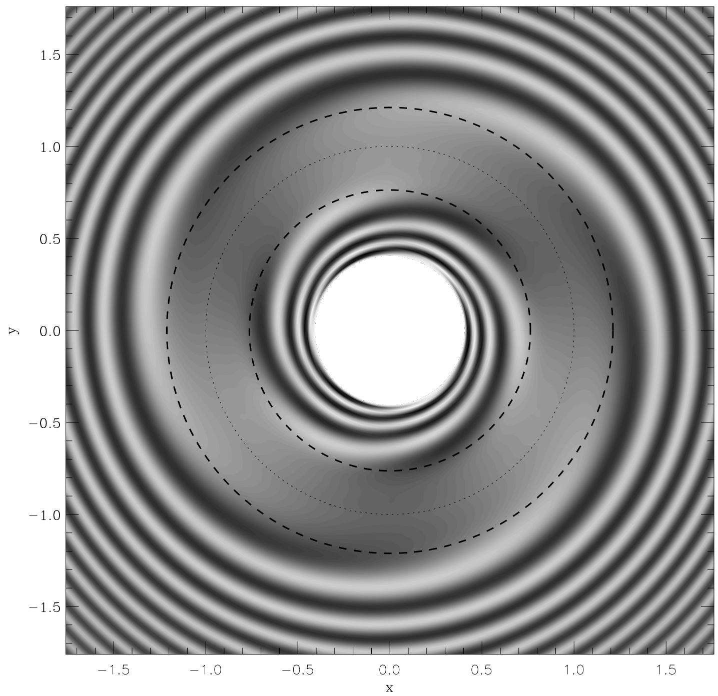

Fig. 2. The radial velocity field of a Keplerian disk torqued by a uniformly rotating $m = 3$ potential. The dotted line shows the perturber's corotation resonance, and the thick dashed lines show its ILR and OLR.

where we introduce the term $\phi' \equiv \phi - \Omega(r_c)t$. The azimuthal velocity is unperturbed: $v_\phi = 2Ax$. The streamlines therefore obey the following equation:

$$\frac{\Phi_0}{AB}\sin^2\left(\frac{m\phi}{2}\right) = x^2 - x_m^2, \tag{3.7}$$

where $x_m > 0$ is a constant of integration, and we drop the $'$ notation on ϕ for the sake of convenience. Without loss of generality, we can restrict ourselves to the case $\Phi_0 > 0$. In this case x_m represents the streamline's maximum distance from the corotation radius, which is reached at $m\phi = 0$ mod. π since $AB < 0$. A streamline intersects the corotation if and only if $x_m^2 < x_c^2 = -\frac{\Phi_0}{AB}$, which implies that the width of the libration islands depicted in Fig. 4 is $w = 2x_c = (32)^{1/2}\delta_\psi$. The last term in this expression is defined as follows:

$$\delta_\psi = [\Phi_0/(-\kappa^2 d\log\Omega/d\log r)]^{1/2} = [\Phi_0/(-8AB)]^{1/2}. \tag{3.8}$$

Streamlines with $x_m < x_c$ are closed and lie within the eye-shaped region, while streamlines with $x_m > x_c$ never reach the corotation radius. These are depicted in

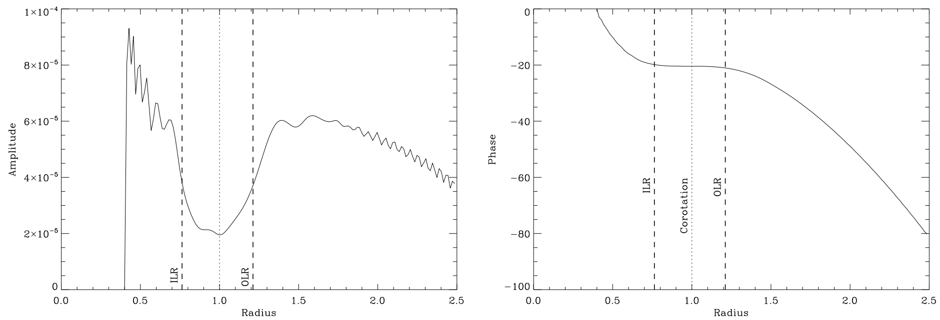

Fig. 3. Amplitude (left) and phase (right) of the radial velocity field for the $m = 3$ tidal response of Fig. 2, as a function of distance from the central object.

the white region of Fig. 4. The streamlines within the eye-shaped islands are said to be in *libration*, which means that the azimuth of a fluid element following such a streamline does not span the whole range $[0, 2\pi]$, and therefore is not a monotonic function of time; its derivative alternates between positive and negative values. On the other hand, fluid elements outside the libration islands are said to be in circulation. This implies a motion with the contrary properties: the azimuth of a fluid element increases or decreases monotonically with time, and spans the whole $[0, 2\pi]$ interval. The streamlines that have $x_m = x_c$ separate these two domains (the libration and circulation regions), and are called the *separatrices*.

We will now list some properties of the corotation torque exerted on a disk by an external m-fold perturbing potential.

First, this torque is proportional to the gradient of Σ/B, evaluated at the corotation radius. Since B is equal to half the flow vorticity, the corotation torque is also proportional to the gradient of the vortensity. The corotation torque is therefore zero in a disk with $\Sigma \propto r^{-3/2}$, such as the minimum mass solar nebula (MMSN).

The corotation torque exerted by an $m-$fold perturbing potential on the disk is

$$\Gamma_C = \frac{\pi^2 m}{2} \left[\frac{\Phi_m^2}{d\Omega/dr} \frac{d}{dr} \left(\frac{\Sigma}{B} \right) \right]_{r_c}, \tag{3.9}$$

where the term in brackets is to be evaluated at the corotation radius.

The libration timescale is much larger than the orbital timescale. As a consequence, on orbital timescales the motion of librating fluid elements can be considered as circular in a non-rotating frame. These fluid elements therefore carry a certain amount of specific angular momentum, which depends only on their radial position. As they librate their radial position oscillates back and forth about the corotation radius, which implies that angular momentum is periodically given to and taken from the perturber. Because the librating fluid elements move within a radially bounded interval, their angular momentum variation must average out to

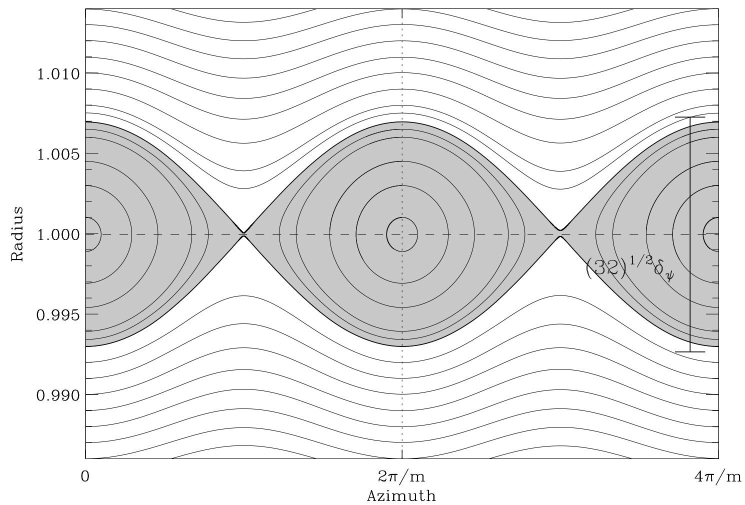

Fig. 4. Streamlines in the (φ, r) plane for an $m = 2$ corotation resonance. The shaded regions are the libration islands. One can notice that the streamlines in the outer and inner regions (white) are circulating, and exhibit radial oscillations. The amplitude of this motion decreases with the streamline's distance from the corotation radius ($r = 1$). At the same time, they do not exhibit any winding; i.e., all streamlines reach their maximum distance from the corotation radius at the same azimuths $\varphi = 0,\ 2\pi/m, \ldots$ This is the expected behavior of evanescent, pressure-supported waves, which have a purely imaginary radial wave-vector (meaning no winding, and an exponential decay over the disk pressure scale length).

zero over timescales large compared to their libration period.

The libration period depends on the streamline. This implies that phase mixing makes the corotation torque tend to zero after a few libration timescales, not only in average but also in its instantaneous value. This is known as the saturation of the corotation torque. It can be avoided if fluid elements can exchange angular momentum not only with the perturber, but also with the remainder of the disk. Viscous stress can extract angular momentum from the libration islands and prevent saturation.

The corotation torque saturation can also be described as follows: when the disk viscosity is close to zero, the vortensity is conserved along a fluid element path. The libration of fluid elements redistributes the vortensity within the libration islands. Once the vortensity has been sufficiently stirred up, even an infinitesimally small amount of viscosity suffices to render the vortensity uniform over the whole libration island. The corotation torque then goes to zero (i.e., saturates), because it scales with the vortensity gradient.

In order to avoid saturation, the viscosity must be high enough to prevent the vortensity from becoming uniform over the libration islands. This is possible if the viscous timescale across these islands is smaller than the libration timescale, as shown by Ogilvie and Lubow (2003). In this case, viscous diffusion across the libration islands permanently imposes the large-scale vortensity gradient over the libration islands.

Finally, it should be noted that saturation properties can not be captured by a linear analysis. Saturation requires a finite libration time, and thus a finite resonance width. In the linear limit the corotation torque appears as a discontinuity in the advected angular momentum flux, which would correspond to infinitely narrow, fully unsaturated libration islands with infinite libration times.

4 Planetary migration

The torque expressions given in sections 3.1 and 3.2 are the building blocks that will enable us to evaluate the tidal torque between a planet and a protoplanetary disk. Throughout this section, we assume for the sake of simplicity that the planet is on a fixed, circular orbit. The study of eccentric planets is deferred to section 5. Note that when a planet migrates, its osculating orbit has a non-vanishing eccentricity; this complication, however, is usually neglected.

4.1 Type I migration

We first consider the case of a low-mass planet (we will specify later how small this is), so that the overall disk response can be treated as a linear superposition of its responses to individual Fourier components of the potential. Each component torques the disk at its Lindblad and corotation resonances. We denote by Γ^m_{ILR} the torque of the m^{th} potential component at its own ILR, and adopt similar notation for the torques at the Outer Lindblad Resonance (Γ^m_{OLR}) and corotation resonance (Γ^m_{CR}). The total tidal torque exerted by the disk on the planet, which is equal and opposite to the torque exerted by the planet on the disk, can therefore be written as

$$\Gamma = \sum_{m>0} \Gamma_{ILR} + \sum_{m>0} \Gamma_{OLR} + \sum_{m>0} \Gamma_{CR}. \tag{4.1}$$

The first series in this sum is the total Inner Lindblad torque, and the second is the total Outer Lindblad torque. The absolute value of either term is also called the one-sided Lindblad torque. The last term is called the corotation torque. The sum of the two Lindblad torques is generally referred to as the *differential Lindblad torque.*

4.1.1 Differential Lindblad torque

In order to add the Lindblad torques at the inner and outer resonances, one must know the effective location of these resonances. Since the planet is considered to be on a fixed circular orbit, all of the Fourier components of the potential have the same pattern frequency as the planet. Their ILRs will thus all be inside the planet's orbit, while their OLRs will be outside. From Eq. (3.4) one can see that the Lindblad resonances approach the corotation radius as $m \to \infty$. However, we have also seen in section 3.1.3 that the waves launched by the potential components are slightly offset from the resonance locations. In particular, as $m \to \infty$ the turning point locations tend to pile up at a radius given by:

$$r = r_c \pm \frac{\Omega}{2A} H \tag{4.2}$$

These points of accumulation correspond to the radius at which the flow becomes supersonic in the corotating frame (Goodman and Rafikov, 2001). In the case of a Keplerian disk, these points are located $\pm(2/3)H$ away from the corotation radius. This has an important consequence: there is a sharp cut-off in the high-m torque components (for $m \gg r/H$) (Artymowicz, 1993b), since the high-m potential components become localized in increasingly narrow annuli around the perturber orbit. The value of a potential component at the accumulation point (where the torque is exerted) therefore tends to zero as m tends to infinity.

Fig. 5 illustrates the one-sided Lindblad torques. In particular, one can see that the cutoff occurs at larger m in a thinner disk (the outer torque value peaks at $m \sim 8-9$ for $h = 0.07$, while it peaks at $m \sim 21-22$ for $h = 0.03$). Also, for both disk aspect ratios there is a very apparent mismatch between the inner and the outer torques; the former is systematically smaller than the later. If we consider the torque of the disk acting on the planet, then the outer torque is negative and the inner torque is positive; the total torque on the planet is therefore negative. As a consequence, migration is directed inwards and the orbit decays towards the central object (Ward, 1986).

Note that the one-sided Lindblad torques scale as h^{-3}. This scaling can be recovered from the following simple argument: the individual Lindblad torques given by Eq (3.3) scale with m^2. The one-sided torque is obtained by summing the series up to a cut-off value $\propto r/H$; hence, this sum scales with $(r/H)^3$.

One can also note in Fig. 5 that the mismatch between the two torques is larger in the thicker disk. Indeed, it can be shown that this relative difference scales with the disk thickness (Ward, 1997). Since the one-sided torques scale as h^{-3}, the migration rate scales as h^{-2}.

There are several reasons for this torque asymmetry, which conspire to make the differential Lindblad torque a sizable fraction of the one-sided torque in a disk with $h = O(10^{-1})$ (Ward, 1997). In particular, for any given m value the inner Lindblad resonance lies further from the planet's orbit than the outer Lindblad resonance. This is very apparent in Fig. 3.

Tanaka et al. (2002) have given the most up-to-date estimate of the differential Lindblad torque. They examine the cases of a vertically resolved, isothermal, three-dimensional disk, and an infinitely thin, isothermal disk. These results are respectively:

$$\Gamma_{LR}^{3D} = -(2.340 - 0.099\zeta)q^2\Sigma\Omega_p^2 a^4 h^{-2} \tag{4.3}$$

$$\Gamma_{LR}^{2D} = -(3.200 + 1.468\zeta)q^2\Sigma\Omega_p^2 a^4 h^{-2} \tag{4.4}$$

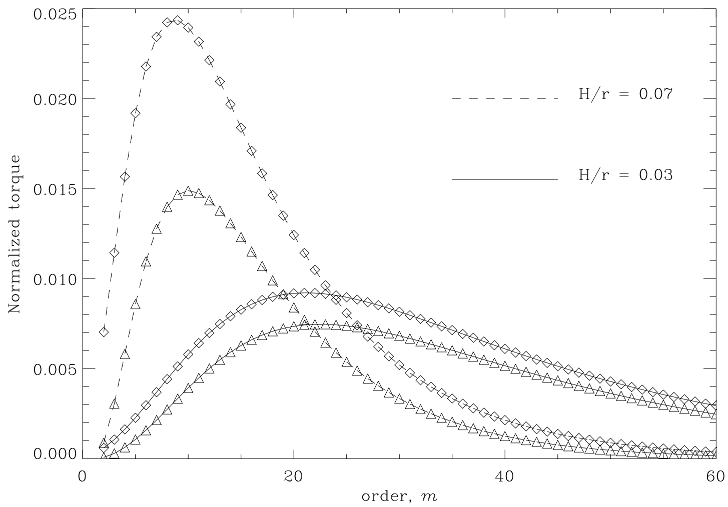

Fig. 5. The absolute value of individual inner (triangle) and outer (diamond) torques in $h = 0.07$ and $h = 0.03$ disks, as a function of m. The torques are normalized to the value $\Gamma_0 = \pi q^2 \Sigma a^4 \Omega_p^2 h^{-3}$. Since one-sided Lindblad torques scale as h^{-3}, the total areas under each curve are of the same order of magnitude.

$$ \tag{4.5}$$

From these estimates, one can infer the migration timescale of the planet. This calculation is only approximate, as it neglects the corotation torque exerted on the planet. As we shall see later, however, the corotation torque is not large enough to change the order of magnitude of the total torque except in very particular circumstances (the steep surface density profile that can be found at the edge of a cavity, for instance, or in a mildly non-linear regime). Since the rate of angular momentum loss by a planet with mass M_p and migration rate $\dot{a}$ is given by $2Ba\dot{a}M_p$, we can infer the migration timescale $\tau_{\rm mig} = a/\dot{a}$ as follows:

$$\tau_{\rm mig} = \frac{h^2}{4Cq\mu_D} T_0, \tag{4.6}$$

where C is a dimensionless coefficient that is an affine function of ζ ($C = 2.340 - 0.099\zeta$, in the isothermal 3D case). We refer the reader to section 2.2 for other definitions. Let us calculate the approximate migration timescale for a 10 $M_\oplus$ mass planet orbiting at 5 AU from a solar mass star, embedded in a minimum mass planetary nebula for which we assume $h = 0.07$. The reduced mass of the disk is $\mu_D = 1.4 \cdot 10^{-3}$, so the migration timescale $\tau_{\rm mig}$ is approximately $3 \times 10^4/C$ orbits or $3 \times 10^5/C$ years. A more precise estimate depends on the value of $C >\sim 1$, which depends on the surface density and temperature profiles.

As long as these functions are smooth and can be approximated by power laws, however, the migration timescale will have the same order of magnitude. In the case that we consider here, this timescale is much shorter than the disk lifetime. This result has actually been a bottleneck for the theory of planet formation. The mass doubling time of a protoplanet with mass $M_p \sim 10\ M_\oplus$ is much larger than the timescale for it to migrate all the way to the central object. This would seem to imply that the process of gas accretion, which converts such objects into giant planets, can occur only after the planet has been brought close to its parent star. In this respect, the existence of giant planets with orbital radii much larger than those of the "hot Jupiters" so far detected remains an unsolved problem.

4.1.2 Pressure buffer

One remarkable feature of Eqs. (4.3) and (4.4) is the differential Lindblad torque's weak dependence on the slope of the surface density function in the 3D case. In the 2D case, the differential Lindblad torque actually increases as one increases the surface density slope. This is quite the opposite of what one would naively expect, since as one increases the slope the surface density increases at the Inner Lindblad Resonances and decreases at the Outer Lindblad Resonances. As one increases the surface density gradient, however, one simultaneously increases the radial pressure gradient. This effect makes it easier for the centrifugal force to achieve radial equilibrium, making the disk more and more sub-Keplerian. As a consequence, the Outer Lindblad Resonances approach the planet's orbit while the Inner Lindblad Resonances recede from it. This process plays against the more obvious effect of the surface density. In an isothermal 3D disk, the two effects approximately compensate for each other; the resonance shift effect dominates, however, in an isothermal 2D disk. This effect is known as the pressure buffer (Ward, 1997; Tanaka et al., 2002), and frustrates any reasonable attempt to decrease the differential Lindblad torque by tuning the power law indices of the surface density and temperature profiles. It also makes an inward type I migration inevitable. We mention a recent work by Menou and Goodman (2004), however, who exploit the differential Lindblad torque's extreme sensitivity to the location of the Lindblad resonances. These authors consider realistic models of T Tauri α-disks instead of the customary power law models, and show that type I migration can be significantly slowed at some locations in the disk, in particular at opacity transitions. In a different vein, Terquem (2003) considers a disk threaded by a toroidal magnetic field, and shows that the planet torques the disk at the location of magnetic resonance located on each side of the corotation radius. In certain circumstances, the total torque felt by the planet is positive, hence the planet migrates outwards. Although the situation considered by Terquem (Terquem, 2003) is in principle unstable to the magneto-rotational instability (MRI, see section 4.4), the MRI is inhibited in 2D calculations, which allowed Fromang et al. (2005) to undertake 2D numerical simulations of the situation considered by Terquem (2003). These simulations essentially confirmed the analytic predictions of Terquem (2003).

4.1.3 Wake properties

Thus far the planetary torque has been evaluated by summing torques at individual resonances. Further insight into the disk response can be gained by examining the planet's wake, which is due to the simultaneous action of all resonances; in other words, the wake is the superposition of all individual responses to the potential components. Ogilvie and Lubow (2002) have shown that these waves constructively interfere to yield a one-armed spiral response, such as the one shown in Fig. 6. More precisely, they have shown that in the outer disk all waves with different m values add constructively except for the lowest modes ($m \leq 2$, for a protoplanetary disk with $h = 0.1$). In the inner disk the potential components also constructively interfere, but as $r \to 0$ the constructive interference fails for all m.

The waves excited by any given potential component can be written as

$$\xi(r, \phi, t) = \xi_0(r) \exp\left\{ i \left[\int k_r(r) dr + m(\phi - \Omega_p t) \right] \right\} + c.c., \tag{4.7}$$

where ξ is any perturbed quantity associated with the wave, $\xi_0(r)$ is its amplitude, and $k_r(r)$ is the radial wave vector. If at a given instant in time t, one stands at a location defined by r and ϕ and then moves by varying these quantities by dr and $d\phi$, then the wave phase varies by $k_r(r)dr + md\phi$. One thus remains on an isophase surface as long as dr and $d\phi$ fulfill the relation $dr/d\phi = -m/k_r(r)$. The pitch angle β of the wave (and consequently of the wake, owing to the constructive interference mentioned above) is given by $\tan\beta = |dr/(rd\phi)|$, so $\beta = \tan^{-1}(m/k_r r)$. In the limit of large m and for a tightly wound wave, Eq. (3.5) yields the relation $m^2(\Omega - \Omega_p)^2 \approx c_s^2 k(r)^2$. From this we can deduce the pitch angle $\beta = \tan^{-1}[c_s/(r|\Omega - \Omega_p|)]$. As a consequence, we see that the wave (and hence the wake) becomes more and more tightly wound as we recede from the corotation radius, which is already apparent from an examination of Fig. 2, and also that the wave (and wake) will be more tightly wound in a disk with lower sound speed (i.e., in a thinner disk). Finally, we note that as expected the above expression for the pitch angle is independent of m, which is a necessary condition if all the waves with different m are to interfere constructively. As we have seen in Fig. 5, the tidal torque is dominated by waves with $m_{\max} \sim r/(2H)$. The azimuthal width of the wake is therefore $w_1 \sim 2\pi r/m_{\max} \sim 4\pi H$, while the wake width measured perpendicular to the spiral arm is $w_1 \sin\beta \sim 4\pi r h^2 \Omega/|\Omega - \Omega_p| \sim 4\pi r h^2$. In thin ($h < 0.1$) protoplanetary disks this width can be extremely small (of the order of $10^{-2}r$, for $h = 0.03$), which underscores the need for high-resolution numerical simulations of planet–disk interactions.

4.1.4 Co-orbital corotation torque

In the preceding section we only considered the torque exerted at the Lindblad resonances. Notwithstanding saturation issues, the corotation torque (the third term of Eq. 4.1) remains to be evaluated. In the linear limit this term can be evaluated just as we evaluated the Lindblad torque, i.e., by summing the torques

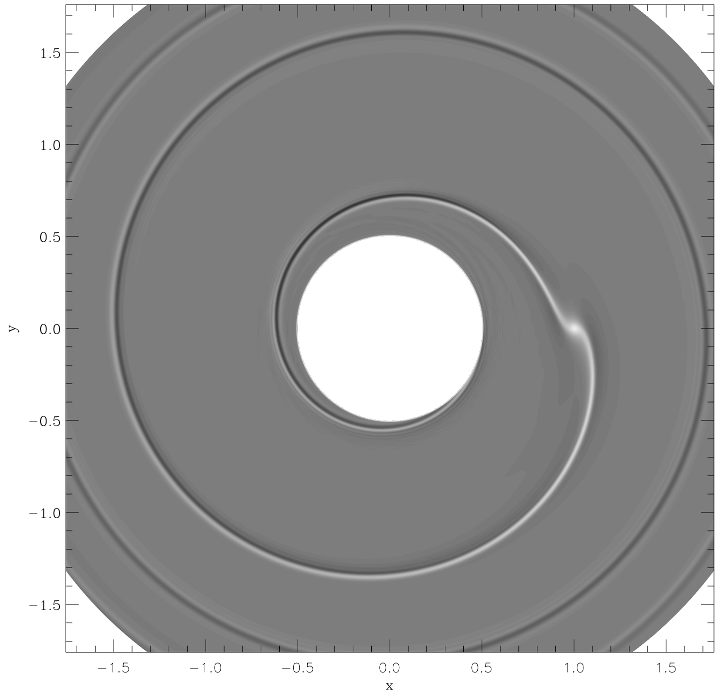

Fig. 6. The surface density response to an embedded low-mass planet, in a disk with uniform aspect ratio $h = 0.05$. The wake has a characteristic one-armed spiral shape.

at individual resonances for all m. All these corotation resonances share the same location: the planet corotation radius, which is very close to the planet orbit (and coincides with the orbit exactly if there is no radial pressure gradient). As a consequence, this torque is called the co-orbital corotation torque.

An estimate of the corotation torque has been made by Tanaka et al. (2002), using an improved expression for the torque at an isolated resonance (see Eq. 3.9). They find the following expressions for the (fully unsaturated) coorbital corotation torque:

$$\Gamma_{CR}^{3D} = (0.976 - 0.640\zeta) q^2 \Sigma \Omega_p^2 a^4 h^{-2} \tag{4.8}$$

$$\Gamma_{CR}^{2D} = (2.040 - 1.360\zeta) q^2 \Sigma \Omega_p^2 a^4 h^{-2} \tag{4.9}$$

We can make the following comments on Eqs. (4.8) and (4.9):

- Their functional dependence on disk and planet parameters is the same as that of the differential Lindblad torques given in Eqs. (4.3) and (4.4). The relative strength of the Lindblad and corotation torques therefore depends on neither the planet mass (provided it is small enough that we stay in the linear regime) nor the disk thickness. Comparing these torques therefore amounts to comparing their numerical coefficients, which are a function of ζ.

- An examination of the coefficients shows that for any reasonable value of ζ, the differential Lindblad torque has a larger absolute value than the corotation torque. Therefore, as anticipated in section 3.1, the differential Lindblad torque dictates the direction and timescale of planetary migration.

- We notice that Eqs. (4.8) and (4.9) yield a positive value for the corotation torque when $\zeta = 0$, while this value vanishes for $\zeta = 3/2$. The latter result could be expected, since the corotation torque scales with the vortensity ($2B/\Sigma$) gradient at the corotation radius. When the disk rotation profile is unperturbed we have $B \propto r^{-3/2}$, so the gradient of the vortensity is zero for $\zeta = 3/2$. In disks with shallower surface density profiles ($\zeta < 3/2$), the corotation torque is a positive quantity that tends to slow down migration. We finally note that in a three dimensional disk, the corotation torque cancellation is only approximate in the case of a flat vortensity profile. This is due to the excitation of $n \neq 0$ waves in these disks, which contribute in a minute proportion to the total torque. The corotation torque associated to these waves does not vanish for $\zeta = 3/2$ (Tanaka, priv. comm.).

Some insight into the dynamics of the coorbital region can be gained by evaluating the horseshoe drag on the planet. The horseshoe region of a protoplanet orbiting within a gaseous protoplanetary disk resembles the horseshoe region of the restricted three-body problem (hereafter RTBP, see Murray and Dermott (2000), p. 63 *et sq.*). This region can be seen in Fig. 7, which shows streamlines in the corotating frame of a high-mass planet for a disk with $h = 0.04$. Ward (1991) has evaluated the drag exerted by this region on the planet. It corresponds to the total rate of angular momentum exchange between the planet and all the fluid elements that perform a horseshoe U-turn across the planet orbit. Fluid elements executing such U-turns behind the planet gain angular momentum as they switch from the inner leg to the outer leg of their streamline, and therefore exert a negative torque on the planet. Similarly, fluid elements executing a horseshoe U-turn in front of the planet exert a positive torque. As was shown by Ward (1991), these contributions do not cancel each other out if there is a radial gradient of vortensity. Moreover, Ward (1992) has shown that the horseshoe drag and corotation torque have the same functional dependence on the disk parameters, provided that the horseshoe zone width is properly evaluated. Finally, Masset et al. (2006a) have shown that the horseshoe drag and the co-orbital corotation torque (as given by the estimates of Tanaka et al., 2002) are in excellent agreement, even though the two quantities have no reason to coincide exactly[3]. If x_s is half of the horseshoe

[3] A possible reason for this can be seen by looking at planets with very low masses. In this limit the width of the horseshoe zone tends to zero, whereas the disk region contributing to the

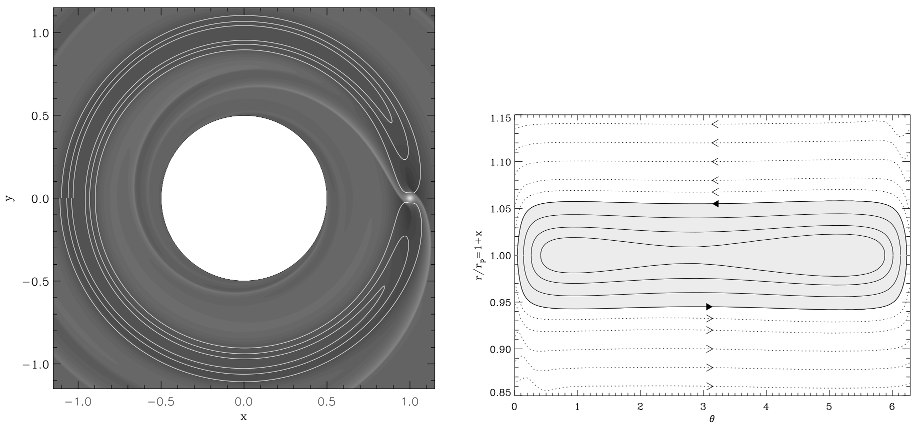

Fig. 7. Horseshoe streamlines of a high-mass planet held on a fixed circular orbit, shown in the $x - y$ plane (left) and $r - \phi$ plane (right). The shaded area in the right-hand plot indicates the whole set of horseshoe streamlines, i.e., the horseshoe region. The region owes its name to the aspect of the streamlines in the corotating frame (left).

zone width, then the horseshoe drag is given by the following expression (Ward, 1991):

$$\Gamma_{HS} = \frac{3}{4}\Sigma\Omega_p^2 x_s^4 \left[\frac{d\log(\Sigma/B)}{d\log r}\right]. \tag{4.10}$$

The co-orbital corotation torque is prone to saturation, in much the same way as the corotation torque from an isolated resonance. Libration in the horseshoe region tends to flatten out the vortensity profile, which in turn tends to cancel out the corotation torque. Saturation, however, is a non-linear effect; it relies upon a finite libration region width and libration time. It would be incorrect to sum the contributions of individual, partially saturated corotation resonances to determine the degree of saturation of the coorbital corotation torque. The latter is actually more saturated than what such an estimate would yield. Rather, an estimate of the co-orbital corotation torque saturation can be obtained by evaluating the steady-state horseshoe drag in a viscous disk (Masset, 2001). Whenever there is radial drift between the disk material and the planet, whether due to the disk viscous drift, planet migration, or a combination of these effects, the horseshoe zone changes its shape as seen in the co-moving frame[4]. More precisely, the horseshoe zone adopts an asymmetric shape as seen in Fig. 8, such that material can flow on horseshoe U-turns from the outer to the inner disk (or vice-versa, depending

corotation torque typically extends over a distance H from the corotation, on both sides of the latter.

[4]The frame that is in *instantaneous* corotation with the planet, and migrates along with it.

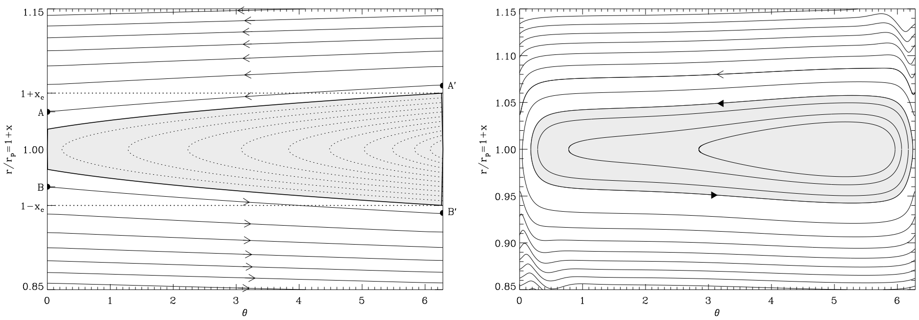

Fig. 8. Horseshoe streamlines in the corotating frame of a viscous disk. The left-hand plot shows the streamlines of the toy model presented in the text, while the right-hand plot shows streamlines from a numerical simulation of a planet in the disk. In both cases the gray area represents the set of fluid elements trapped in the co-orbital region, while the *unique* streamline in the white region represents the path of a fluid element that initially circulates in the outer disk, executes one horseshoe U-turn in front of the planet ($\phi >\sim 0$), losing some angular momentum, and finally circulates in the inner disk. The asymmetry of the horseshoe region is clear (its left side is narrower than its right side), and this allows material to flow from the outer to the inner disk.

on the drift sign). The left-hand plot shows the streamlines of a very simple toy model, in which we approximate the action of the planet on the flow according to the following prescription:

1. The planet acts only on fluid elements at $\phi = 0 \pmod{2\pi}$, in conjunction with the planet.
2. If in conjunction the distance $|x|$ between the fluid element and the orbit is smaller than the threshold value x_s (the half-width of the horseshoe region), then the fluid element is "reflected" with respect to the planet orbit and sent to $(\phi, -x)$. Otherwise, no action is taken on the fluid element. This is meant to mimic the U-turn of fluid elements at the ends of the streamlines in the horseshoe region.
3. The fluid element velocity is always assumed to be equal to the velocity of the unperturbed disk.

In the inviscid case, this oversimplified model reproduces the main properties of the co-orbital region: rectangular, librating streamlines in the horseshoe region (whose width is $2x_s$) and circulating, circular streamlines in the outer and inner disk. There is no wake, however. In a disk with uniform (non-zero) viscosity and surface density, the fluid element velocity in the corotating frame, to lowest order in x/a, is given by

$$\dot{x} = -\frac{3}{2}\frac{\nu}{a} \quad \text{and} \quad \dot{\phi} = -\frac{3}{2}\frac{\Omega_p}{a}x. \tag{4.11}$$

This integrates to

$$\phi = \frac{1}{2}\frac{\Omega_p}{\nu}x^2 + \phi_0. \tag{4.12}$$

The streamlines are therefore parabolic arcs in the $\phi - r$ plane. When the planet–disk drift is slow enough, the streamlines of the horseshoe region can be approximated as straight lines over most of their length. There is a limiting case in which the separatrix of the trapped region (represented by a thick solid line in Fig. 8) reaches the corotation radius. Using Eq. (4.12), one finds that this occurs when $\nu \geq \frac{\Omega_p x_s^2}{4\pi}$. Above this critical value of the viscosity, the planet–disk drift time across the horseshoe region is shorter than the horseshoe libration time. We shall examine the consequences of rapid planet–disk drift on the coorbital flow topology in more detail later, in section 4.3. For the moment we limit ourselves to the case of low viscosity, so that we can consider the streamlines to be at a fixed distance from the corotation radius. We can exploit the fact that elements in the shaded region of Fig. 8 are trapped, to subdivide the horseshoe drag into two components:

- The torque exerted by this trapped region on the planet. As the angular momentum of this region is constant in the steady state[5], the torque that it exerts on the planet is equal to the torque exerted by the remainder of the disk on this region (as there cannot be a net flux of angular momentum into this region). Neglecting the disk self-gravity and the pressure torque exerted on the trapped region, this torque reduces to the viscous torque exerted on the separatrices of the trapped region.

- The torque exerted by the fluid elements that execute a horseshoe U-turn but are not in the trapped (shaded) region. These fluid elements are those which pass from the outer disk to the inner disk, thereby yielding a positive torque on the planet which scales with the mass flux across the coorbital region.

Using this decomposition of the horseshoe drag, along with an adequate description of the libration and viscous diffusion inside the horseshoe region, Masset (2001) has found an expression for the horseshoe drag in the steady state regime that depends on the viscosity. Initially this expression was derived for a planet orbiting in a disk with a flat surface density profile, but the result can be generalized to power law surface density profiles:

$$\Gamma_{\rm HS} = \frac{3}{4}\Sigma\Omega_p^2 x_s^4 \frac{d\log(\Sigma/B)}{d\log r}\mathcal{F}(z_s), \tag{4.13}$$

where z_s is defined by

$$z_s = x_s\left(\frac{\Omega_p}{2\pi\nu a}\right)^{1/3} \tag{4.14}$$

[5]It is a closed system with a fixed position.

and

$$\mathcal{F}(z_s) = \frac{4}{z_s^3} - \frac{4g(z_s)}{z_s^4 g'(z_s)}. \tag{4.15}$$

In the last expression, g is any linear combination of the Airy functions Ai and Bi that cancels out for $z = 0$, such as

$$g(z) = \mathrm{Bi}(z) - \sqrt{3}\mathrm{Ai}(z). \tag{4.16}$$

We can use the expansion $g(z)/g'(z) = z - (1/4)z^4 + o(z^4)$ to find the horseshoe drag in the low z_s (*i.e.,* high viscosity) limit. This gives $\lim \mathcal{F}_{z\to 0} = 1$, so we recover the horseshoe drag of Eq. (4.10). This makes sense, as the large viscosity smoothes out local surface density variations. At any instant in time the initial, unperturbed surface density profile thus prevails, and one can derive Eq. (4.10) by direct integration along the horseshoe streamlines. In the low-viscosity limit one can make use of the fact that $\lim g(z)/g'(z)_{z\to\infty} = 0$ so that $\mathcal{F}(z) = 4z_s^{-3} + o(z_s^{-4})$, which gives the following expression for the horseshoe drag:

$$\Gamma_{\mathrm{HS}\ (\nu\to 0)} \sim 6\pi\nu a\Sigma\Omega_p x_s \frac{d\log(\Sigma/B)}{d\log r}. \tag{4.17}$$

In the low-viscosity limit, the horseshoe drag is thus proportional to the viscosity (Balmforth and Korycansky, 2001). It is zero in an inviscid disk, corresponding to a complete saturation of the horseshoe region torque.

We mention that in the case of a deeply embedded object (one for which the planetary Hill radius is much smaller than the disk thickness, as we shall see in subsequent sections) the width of the horseshoe region scales as $q^{1/2}$ (Masset et al., 2006a), so that the horseshoe drag scales as q^2. The same is true of the coorbital corotation torque. Masset et al. (2006a) have found from a set of numerical calculations that although the horseshoe drag does not account for all of the co-orbital corotation torque, it nevertheless represents a large fraction of it. The horseshoe drag is therefore a good approximation to the coorbital corotation torque.

There is a balance between the action of libration, which tends to flatten the vortensity profile, and that of viscous diffusion, which tends to restore its large-scale gradient. In the above analysis, this balance is quantified by assuming a laminar disk obeying the Navier-Stokes equations. Under these assumptions, one can estimate the critical viscosity required to prevent corotation torque saturation (or the saturation of an isolated resonance that is not co-orbital, as we shall see in more detail in section 5.1). It is not clear whether this picture also holds when the viscosity is due to turbulence (see section 4.4) on scales larger than the libration region. All that is needed to avoid corotation torque saturation is to bring "fresh" vortensity from the inner or outer disk into the libration region on timescales less than that of the libration. The standard approach, which is based on a comparison of the libration and viscous timescales across the libration region, is certainly correct when the largest turbulent scale is smaller than the libration zone width. Under this scenario the vortensity enters the libration region in a diffusive manner, but this approach is unlikely to be adequate when the turbulence scale is larger than the libration region. In this case, which for example can occur if there is MHD turbulence, one instead has to compare the libration timescale to the advection timescale across the libration region at the average turbulent speed. This approach favors de-saturation, and seems to imply that preventing the corotation torque saturation is easier than suggested by a comparison of the libration and viscous diffusion timescales.

4.1.5 Type I and the onset of non-linear effects

Type I migration corresponds by definition to a regime where the disk response is correctly described by linear analysis. One can notice that if the disk viscosity is low enough, linear analysis will always break down at some distance from the orbit. Indeed, the planet's tidal field excites density waves at the Lindblad resonances, which propagate away from the orbit. As they travel their profile steepens, in much the same way that an acoustic wave will evolve in a homogeneous gas at rest. Ultimately this profile steepening will lead to the appearance of shocks, so linear analysis must always fail at some distance from the orbit which depends on the planet mass. This does not imply that type I migration does not exist. Rather, this underscores the need to define type I migration as migration in a regime for which the disk response remains linear in the vicinity of the planet (i.e., where the waves are launched by the tidal field) so that the total torque is correctly predicted by linear analysis. The ultimate fate of the waves does not matter, provided they are damped far away from the excitation region. Goodman and Rafikov (2001) have provided an analytic description of how profile steepening occurs for the wakes excited by low-mass planets. They arrived at the following results:

- The excitation region can be separated from the shock if the planet mass is smaller than $M_1 = c_s^3/(2|A|G)$. Note that M_1 is the mass at which the planetary Bondi radius (GM_1/c_s^2) becomes larger than the distance between the corotation and wake excitation radii $(c_s/2|A|)$. For $M_p > M_1$, the shock begins immediately and their analysis fails.

- The shock develops at a distance d from the orbit that is given by $d \approx 0.93\left(\frac{\gamma+1}{12/5}\frac{M_p}{M_1}\right)^{-2/5} H$, where γ is the adiabatic index of the gas. It is not surprising that this distance scales with the disk thickness, and also gets shorter as M_p increases. We note that in an unsheared medium, the distance at which profile steepening gives way to shocks is inversely proportional to the initial amplitude of the wave. Here, in a differentially rotating disk, this distance scales with amplitude to the power $-2/5$; even at very low planet masses, the wake thus becomes a shock at relatively short distances from the orbit. For example, in a disk with $h = 0.05$ M_1 amounts to 28 $M_\oplus$, and the wake becomes a shock at $d \approx 3.6H$ from a 1 $M_\oplus$ planet. To put it another way, whenever tidal migration is a relevant process, for a planet embedded in a protoplanetary disk with a realistic aspect ratio, profile steepening will lead to the formation of a shock at some distance from the orbit that is at most a few times the disk thickness. Note, however, that the distance quoted above is still much larger than the excitation region of the wake. The latter peaks at a distance $\pm 4/3H$ from the orbit, so the migration mode adopted by such objects can safely be assumed to be type I.

- Once the wake becomes a shock, its angular momentum flux decays as $|x|^{-5/4}$ (for $|x| \gg d$)
- Azimuthal slices show that as one recedes from the excitation region, the profile adopts an $N-$wave shape.

We comment that in numerical simulations of low-mass objects embedded in thin disks, the mesh resolution may be insufficient to keep proper track of the wake profile evolution as it recedes from the planet and becomes more and more tightly wound. Provided the resolution is sufficient over the wake excitation region, however, the tidal torque should be correctly accounted for and the migration rate should be correct. One should still keep in mind that if the resolution is not sufficient, the wake could become artificially damped by the grid, closer to the planet than it otherwise would by shock formation.

We note that M_1 is also the mass at which the Hill radius, given by $R_H = (GM_p/4|A|\Omega)^{1/3}$, is equal to $(\Omega/2\sqrt{2}|A|)^{2/3} \approx 0.61H$ in a Keplerian disk. Through a reduction of the flow equation to dimensionless form, Korycansky and Papaloizou (1996) have found a dimensionless parameter that determines the flow non-linearity: $\mathcal{M} = q^{1/3}/h = 3^{1/3}R_H/H$. In a Keplerian disk, one has $M_p/M_1 = (3/2)\mathcal{M}^3$. As $\mathcal{M} \to 0$, the flow becomes linear and the planet undergoes type I migration. When $\mathcal{M}$ is comparable to unity, the flow becomes non-linear in the vicinity of the planet. The onset of non-linearity had long been thought to correspond to the clearance of a gap around the planet's orbit (see section 4.2). The so-called thermal criterion for gap opening corresponds to $R_H > H$ (i.e., $\mathcal{M} = 1.44$); when the planetary Hill sphere "emerges" from the disk, the planet begins to open a gap (we shall examine the gap opening mechanism in more detail in section 4.2). This justifies the qualification "deeply embedded" for objects which have a Roche lobe smaller than the disk thickness, and for which the flow perturbation remains linear so that they undergo type I migration. Recently, Masset et al. (2006a) have found that non-linearities occur in the flow for values of the dimensionless parameter smaller than that quoted above for gap clearance. Indeed, they find a significant increase in the width of the horseshoe region for $q/h^3 \sim 0.6$, which in turn yields an enhancement of the horseshoe drag and consequently of the co-orbital corotation torque. This growth of the co-orbital region is linked to the flow's transition from a low-mass situation, in which there is no Roche lobe, to a high-mass situation and the appearance of circumplanetary streamlines (i.e., a Roche lobe). This may have important consequences for planetary migration in shallow disks (*i.e.,* disks whose surface density profile $\Sigma \propto r^{-\zeta}$ has $\zeta < 3/2$). In such disks the vortensity gradient across the orbit is positive, and so is the co-orbital corotation torque. As we can see in Eqs. (4.3-4.4) and Eqs. (4.8-4.9), although the differential Lindblad torque

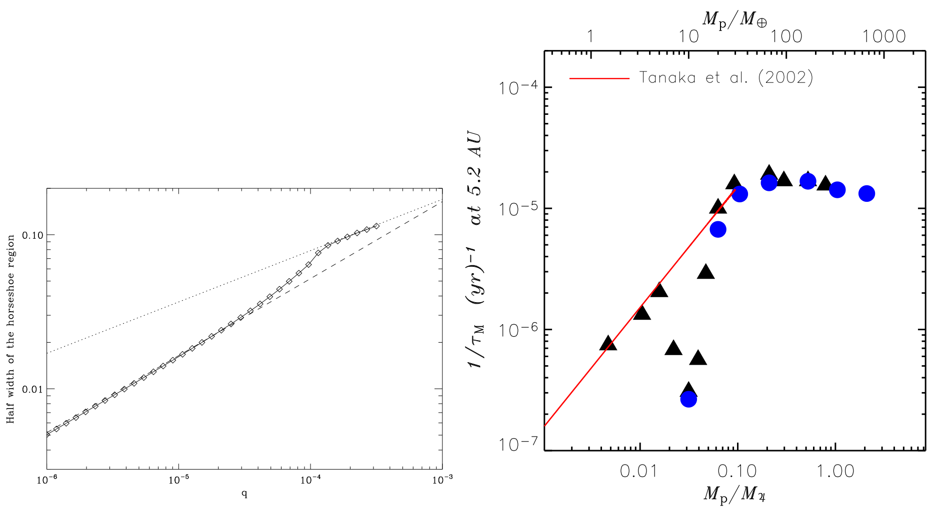

Fig. 9. Left: half-width of the horseshoe region as a function of the planet mass in a disk with $h = 0.05$. For low planet masses this width scales as $q^{1/2}$ (dashed line), while for higher masses one recovers the $q^{1/3}$ scaling of the restricted three-body problem (dotted line). At the transition between these two regions, around $q \sim 10^{-4}$, the horseshoe width is larger than a linear analysis of the planet–disk interaction would predict. Consequently, the co-orbital corotation torque is also larger than that predicted by linear analysis. Right: the inverse of the migration timescale τ_M as a function of the planet mass, for a disk with the same aspect ratio ($h = 0.05$). One can clearly see an *offset* between this drift rate and the predictions of linear analysis (solid line) for a planet mass around 10 $M_\oplus$. This offset corresponds in this case to a slowing down of the migration by one order of magnitude with respect to the type I estimate. This plot is derived from the results of 3D calculations by D'Angelo et al. (2003). The different symbol shapes refer to different prescriptions for the potential's softening length.

dominates the co-orbital corotation torque they nevertheless have same order of magnitude. Therefore, if the corotation torque is sufficiently enhanced, it may cancel out the total torque and halt the migration. Fig. 9 shows how important this effect can be on the migration of protocores with $M_p \sim 10\ M_\oplus$, whose type I migration drift would otherwise be extremely large and jeopardize the possibility of accreting a gaseous envelope.

We mention in passing that in certain circumstances, the corotation torque can overcome the Lindblad torque even in a linear situation. This is the case at the edge of a cavity, even a shallow one, as was shown by Masset et al. (2006b). The sharp raise in surface density at the edge favors a strong, positive corotation torque, and allows for the existence of a stable fixed point where the total torque cancels out, and which acts as a planet trap.

Table 1. Flow properties for different values of the dimensionless parameters that characterize the degree of non-linearity. $R_B = GM_p/c_s^2$ is the planetary Bondi radius. The last column gives the planet mass in Earth masses, assuming a disk with $h = 0.04$ around a central star with one solar mass (in which case $M_1 = 14\ M_\oplus$).

	R_H/H	$\mathcal{M}$	M_p/M_1	R_B/H	$M_p/M_\oplus$
Linear regime	$\to 0$	$\to 0$	$\to 0$	$\to 0$	$\to 0$
Offset maximum	0.58	0.84	0.9	0.6	13
Gap clearance	1.0	1.44	4.5	3.0	64

In Table 1 we summarize the different (and equivalent) dimensionless parameters that can be used to characterize flow non-linearity. Values for these parameters are given for the linear regime, for the regime of maximum *offset* described above (when the corotation torque is enhanced with respect to its linearly predicted value), and at gap clearance (the thermal criterion described above).

4.2 Type II migration

Section 4.1 introduced the concept of planetary migration by examining the planet–disk interaction under a linear analysis. In section 4.1.5 we began to address the non-linear effects as well, by investigating their onset conditions. In this section, we are concerned with a flow that is markedly non-linear. The planet mass in this case is above some threshold that we shall specify later. As we shall see, a large mass planet may open up a gap in the disk around its orbit, with important consequences on its migration.

4.2.1 Shock appearance and horseshoe asymmetry

As we have seen in section 4.1.5, the wake excited by a planet eventually turns into a shock, which cedes the angular momentum of the planet back to the background flow. The location at which profile steepening produces a shock depends on the planet mass; the larger the mass, the closer the shock will be to the orbit. For planets above some critical mass, the wake becomes a shock within the excitation region. Under these circumstances, the fluid elements circulating just outside the co-orbital region receive a kick of angular momentum every time they cross the wake. This is represented in Fig. 10. The fluid elements C_1 and C_2, circulating respectively inside and outside of the planet orbit, recede from the orbit after they cross the wake. Paths of undisturbed circulation for these fluid elements are indicated by the dashed lines; their actual trajectories (streamlines) are shown as solid white lines. Another consequence of the adjacent shock is that the horseshoe U-turns are not symmetric. Fig. 10 also shows streamlines of the librating fluid elements L_1 and L_2. They are mapped after a horseshoe U-turn to the points L_1'

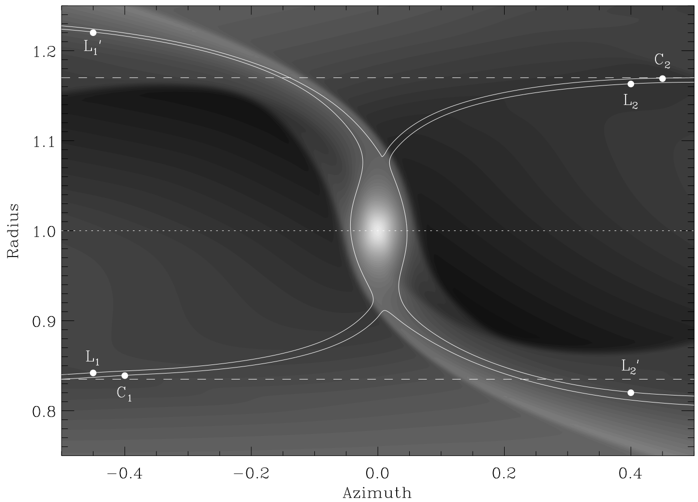

Fig. 10. Asymmetry of the horseshoe region. The circulating fluid elements C_2 (moving towards the left) and C_1 (moving towards the right) recede from the orbit after crossing the shock excited by the planet. Similarly, the librating fluid elements recede from the orbit after executing their horseshoe U-turns (see main text for details). This particular example shows streamlines of the flow in the corotating frame of a 2 M_J planet in a disk with $h = 0.05$. The planet is on a fixed circular orbit, and this snapshot was taken after 22.5 orbits.

and L_2', which are located farther away from the planet orbit than L_1 and L_2. A fluid element initially located inside the libration region thus progressively recedes from the orbit as it performs a sequence of horseshoe U-turns, until it ends up in the inner disk or the outer disk (Lubow et al., 1999). The co-orbital region is thereby emptied, and an annular gap eventually appears around the orbit. The timescale for emptying the co-orbital region can readily be estimated from Fig. 10. After each horseshoe U-turn, the distance of a fluid element from the orbit increases by an amount between 10 and 20 %. The characteristic emptying time of the horseshoe region is therefore between 5 and 10 times half the libration time, which is given by $\tau_{\rm lib}/2 = 2\pi a/(3/2)\Omega_p x_s = (2/3)T_o(a/x_s)$. Here we can estimate from the figure that $x_s \approx 0.16$, so $\tau_{\rm lib}/2 \approx 4\ T_0$. As a consequence, in this particular example, the co-orbital region will be emptied after about 20 to 40 orbits. This simple estimate also shows that the smaller the planet mass, the longer the gap clearance timescale. Indeed, as the planet mass decreases, the horseshoe region becomes more and more symmetric so that more libration times are needed to get rid of the co-orbital material. At the same time, the libration time itself increases. For a 1 M_J planet orbiting in a $h = 0.05$ disk, the clearance timescale of the gap is about 100 orbits.

4.2.2 Steady state flow and gap opening criteria

The situation depicted in Fig. 10 can be a steady state only if the separatrix of the horseshoe region is closed, which implies that the fluid element L'_1, as it follows its streamline, must eventually be mapped to the location of L_2. If this is not the case then the co-orbital region will always lose material, which cannot correspond to a steady state situation. In a viscous disk, however, the process of emptying the co-orbital region will eventually fulfill this condition. As expelled material accumulates just beyond the outer separatrix, a large surface density gradient is built up, which in turn yields a large, negative viscous torque on any fluid elements in this gradient. The fluid elements can therefore drift significantly inward over half a libration time. When the surface density gradient is large enough, the fluid elements drift inwards over the radial range required to close the streamline. Note that this is a self-regulating process: if too much material is expelled from the co-orbital region then the viscous drift of fluid elements near the separatrix becomes larger than the radial kick that they receive as they cross the wake. Material then flows towards the horseshoe region, which establishes a milder surface density gradient and closes the separatrix.

Classically, the gap opening conditions once consisted of two independent criteria (Lin and Papaloizou, 1979; Lin and Papaloizou, 1993; Bryden et al., 1999) that needed to be simultaneously fulfilled. The first, referred to as the thermal criterion (since it imposes a limit on the disk thickness, and hence on the disk temperature), was previously mentioned in section 4.1.5 and requires that the wake becomes a shock just as it is excited. The flow must therefore be strongly nonlinear in the planet's vicinity, and the parameter R_H/H must be larger than some critical value. This critical value is ~ 1, although its precise value can be slightly different. The second criterion is that the viscosity is sufficiently low, so that the surface density jump across the edges of the excavated region is a sizable fraction of the unperturbed surface density. This condition, which is known as the viscous criterion, is expressed as (Lin and Papaloizou, 1979; Lin and Papaloizou, 1986a; Papaloizou and Lin, 1984; Lin and Papaloizou, 1993; Bryden et al., 1999)

$$q > \frac{40}{\mathcal{R}} \tag{4.18}$$

where $\mathcal{R} = a^2\Omega_p/\nu$ is the Reynolds number.

Crida et al. (2006a) have used another condition, namely that the circulating streamline just outside the separatrix should be closed, to derive the gap surface density profile semi-analytically. They require that the integral of the viscous, gravitational, and pressure torques cancels out over one synodic period of a given fluid element. They provide an ansatz expression for the pressure torque that is approximately valid for a reasonable range of planetary masses and disk thicknesses, and derive the following criterion for gap opening:

$$\frac{3}{4}\frac{H}{R_H} + \frac{50}{q\mathcal{R}} < 1. \tag{4.19}$$

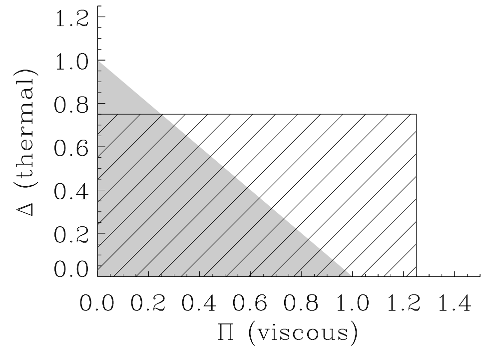

Fig. 11. Graphical representation of the gap opening criteria. The hatched rectangle shows the parameter set (Π, Δ) for which the two standard gap opening criteria (thermal and viscous) are satisfied, while the gray triangle shows the parameter space for which the criterion of Crida et al. (2006a) is satisfied. Π and Δ are defined in the text.

Eq. (4.19) is obtained by assuming that the residual surface density is 10 % of the unperturbed surface density. One can note that this equation is a mixture of the two standard criteria. If one sets $\Delta = \frac{3}{4}\frac{H}{R_H}$ and $\Pi = \frac{50}{q\mathcal{R}}$, then the standard criteria can be read as $\Delta < \frac{3}{4}$ and $\Pi < \frac{5}{4}$. The new criterion, however, is $\Delta + \Pi < 1$. Broadly speaking, this criterion is approximately equivalent to the previous two (see Fig. 11) except in the case where both are only marginally fulfilled. In this corner of the parameter space, the resulting gap is too shallow to be included in criterion (4.19).

As described above, the characteristic time to clear a gap is essentially the time required to build up a surface density gradient that closes the horseshoe separatrix. After this relatively short timescale (on the order of 10^2 orbits), however, nothing ensures that the resulting surface density distribution is a steady state. Rather, the overdense regions located on each side of the gap, which arise from the pileup of co-orbital material evacuated from the gap, will spread radially away from the gap. This process occurs over the disk viscous timescale $\sim r^2/\nu$, which can be much longer than the gap clearance timescale. For a disk with $\alpha = 10^{-3}$ and $h = 0.05$, the viscous timescale is on the order of 6×10^4 orbits. Crida et al. (2006a) have emphasized these two timescales in their analysis of the gap clearance. In particular, they have found that the shorter timescale corresponds to the establishment of a relatively constant profile in $(1/\Sigma)d\Sigma/dr$, while the longer timescale corresponds to the relaxation of the surface density profile over the whole disk. Fig. 12 shows the appearance of a gap opened by a giant planet in a protoplanetary disk.

As we have seen in section 4.1.5, the wake always turns into a shock at some distance from the planet even if it can be correctly described by linear analysis in

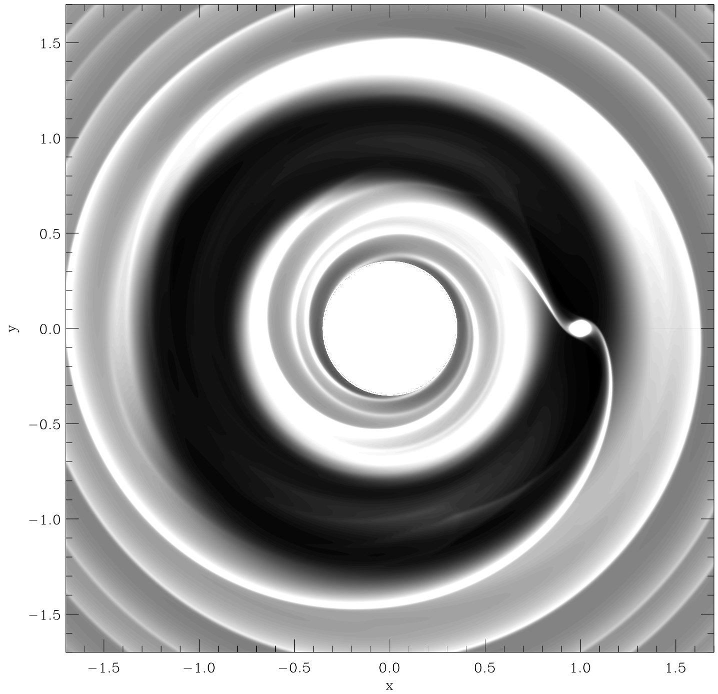

Fig. 12. The gap opened by a 2 M_J planet in a disk with aspect ratio $h = 0.04$ and uniform kinematic viscosity $\nu = 10^{-5}$ (these parameters give $\alpha = 6 \times 10^{-3}$ at the planet's orbit), after $t = 50$ orbits. The gray level represents the gas surface density.

the excitation region. This suggests that a deeply embedded planet which does not fulfill the thermal criterion can still open a gap, whose half-width will be the distance between the orbit and the appearance of the shock (Rafikov, 2002). This has been observed in numerical simulations, but we recall the word of caution given in section 4.1.5: if the resolution is too low, then the wake damping will occur too close to the orbit. The gap will then be too narrow, and open on a much shorter timescale than it would if the resolution were sufficient.

4.2.3 Migration of planets that open a gap

The migration of a planet that has cleared a gap should differ markedly from the type I scenario. Many of the Lindblad resonances fall inside the gap and are therefore inactive, and the emptying of the co-orbital region means that the co-orbital corotation torque will be negligible. One would therefore expect that the resulting migration rate is smaller than the type I estimate.

Actually, a "clean" gap (i.e., a gap with little residual surface density) splits the disk material into an outer disk and an inner disk. Therefore, the planet must drift inwards at the same rate that the outer disk spreads inwards. In other words, the migration rate of a giant planet that has opened a gap in the disk is the same as the viscous drift rate of the disk (Lin and Papaloizou, 1986b). This type of migration is referred to as type II migration (Nelson et al., 2000, and refs. therein). It is usually said that in this regime, the planet's orbit is locked to the disk's viscous evolution. The migration drift rate of the planet is therefore

$$\frac{da}{dt} \sim -\frac{\nu}{a}, \tag{4.20}$$

and its migration time is

$$\tau_{\rm mig} \sim \frac{a^2}{\nu}. \tag{4.21}$$

For a $M_p = 1\ M_J$ planet that undergoes type II migration in a disk with $h = 0.04$ and $\alpha = 6\cdot 10^{-3}$, the migration time starting from $a = 5$ AU is about $1.6\cdot 10^4$ orbits. This corresponds to $\sim 1.6 \cdot 10^5$ years, if the central object has one solar mass.

Using two-dimensional numerical simulations, Nelson et al. (2000) have shown that the migration of giant planets (with masses greater than or equal to one Jupiter mass) in a viscous disk obeys the scenario outlined above, at least broadly speaking. In particular, they found that the timescale of variation in the planet's semi-major axis is similar to the viscous timescale of the disk.

They also used a prescription to represent gas accretion onto the planetary core. This was made possible by removing some mass from the inner Roche lobe at every timestep, and adding the mass and angular momentum thus removed to the point-like mass of the planet. The specific angular momentum of the planet may therefore also vary due to the effects of accretion. The corresponding torque is called the accretion torque. We note in passing that this accretion torque is similar to the corotation torque in a number of ways. Both correspond to material flowing near the horseshoe separatrices, but in the case of accretion this material eventually reaches the location of the planet. Where in previous scenarios a mass unit would perform a full horseshoe U-turn (changing its semi-major axis by $2x_s$ and exchanging an amount of angular momentum equal to $4Bax_s$), the semi-major axis of an accreted mass unit only changes by x_s and the accretion torque thus scales as $2Bax_s$. Not surprisingly, Nelson et al. (2000) have found that enabling accretion slightly slowed the planet's migration. The effect is slight, however; it neither stops nor significantly changes the planet's migration rate. We recall that in a disk with uniform surface density (Nelson et al. used such a disk in most of their calculations) the corotation torque is a positive quantity. Nelson and Benz (2003b), who simulated planets in disks with much steeper surface density profiles[6], have found that in this case the accretion torque is a negative quantity.

[6]Initially their profiles were $\Sigma \propto r^{-3/2}$, yielding a zero corotation torque, but after relaxation of the disk they end up with an accumulation of material in the inner disk that is compatible with a negative corotation torque.

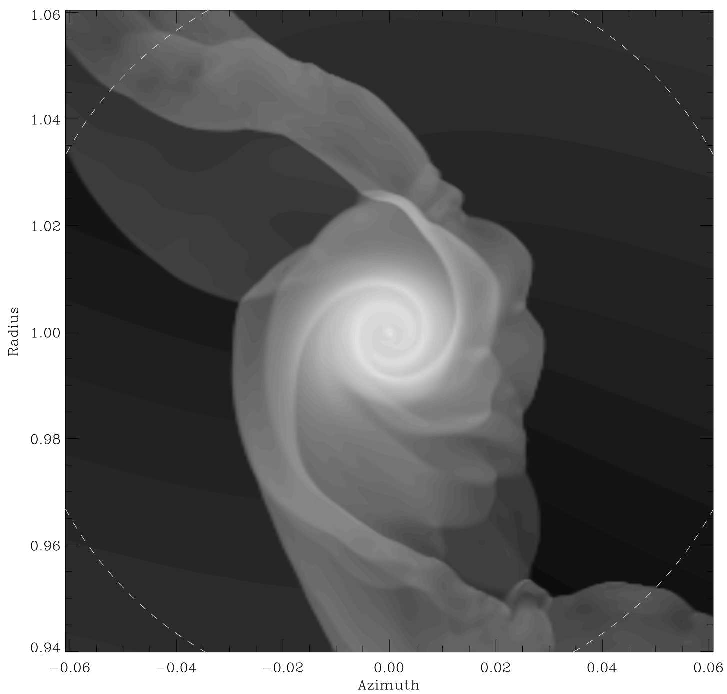

Fig. 13. Surface density within the Hill radius (dashed line) of a 1 M_J protoplanet orbiting in a disk with aspect ratio $h = 0.0.5$, only one orbital period after the introduction of the planet into the disk. This plot comes from a two-dimensional, nested grid Godunov code using an exact isothermal Riemann solver. The $m = 2$ spiral structure in the inner Roche lobe is very apparent. The potential softening length used in this calculation is $\varepsilon = 1.4 \cdot 10^{-3}a$, while the resolution is $8.4 \cdot 10^{-4}a$

It is still only a small fraction of the total torque exerted by the disk on the planet, however.

The accreted gas tends to form a prograde circumplanetary disk inside the Roche lobe. Within this disk, a prominent $m = 2$ spiral shock is excited by the dominant ($m = 2$) tidal component of the primary. This shock appears quite strong in two-dimensional calculations, but is much weaker in three-dimensional calculations (D'Angelo et al., 2002; D'Angelo et al., 2003b). This process drives the accretion of circumplanetary disk material onto the planet. Fig. 13 is a high-resolution image of the surface density response in the inner Roche lobe of a 1 M_J protoplanet, soon after the planet's potential was introduced into an initially unperturbed disk.

As a giant protoplanet accretes the gas flowing through its gap, its mass increases. The tidal truncation of the outer and inner disk thus becomes steeper, and the gap widens. As a consequence, the rate of gas accretion onto the planet decreases. This suggests that planetary gas accretion is a self-limiting process. Nelson et al. (2000) have obtained final masses for their giant planets up to a few Jupiter masses (about 5 M_J). Lubow et al. (1999) have found that the planetary accretion rate is significantly smaller than the rate at which the nebula can bring material to the orbit, for planet masses above $\sim 6\ M_J$. Although these results certainly depend on the disk viscosity, the disk thickness, and the adopted prescription for accretion, taken together they nevertheless suggest an upper mass limit in the range of $5 - 10\ M_J$. This result is of the same order of magnitude as the larger masses inferred for known extrasolar planets.

All the above results have been obtained by assuming that the effective viscosity of the disk is adequately modeled by the Navier–Stokes equation. In this approach the kinematic viscosity is chosen to account for the accretion rates inferred from observations of T Tauri objects. Papaloizou et al. (2004a) have performed much more numerically demanding calculations; instead of resorting to the purely hydrodynamical scheme of including an *ad hoc* kinematic viscosity, their model describes the self-sustained magnetohydrodynamic (MHD) turbulence arising from the magnetorotational instability (MRI).

They find that a giant protoplanet still opens a gap in the disk, in much the same manner as in a disk modeled by the Navier–Stokes equations. In particular, the mass limit for gap opening has approximately the same value in both cases (the laminar case[7] and the MHD case). Surprisingly, the gap in a turbulent disk tends to be larger and deeper than in a laminar disk (Papaloizou et al., 2006). The mass accretion rate tends to be larger in the MHD turbulent case, most likely because of magnetic breaking of the circumplanetary disk (Papaloizou et al., 2004a).

In the standard paradigm of type II migration, the planet is supposed to behave like a representative particle of the protoplanetary disk. Its drift rate should therefore equal the radial velocity of the accretion disk *in the absence of the planet*, at the same location. Although the actual drift rate appears to be of the same order of magnitude as the viscous drift rate (Nelson et al., 2000), the details of their calculations show that this paradigm is invalid. The drift rate in a viscous disk with uniform surface density and uniform kinematic viscosity is given by $-\frac{3}{2}\frac{\nu}{r}$, so in such a disk we should expect the type II migration of a giant planet to speed up as it approaches the central object. One could argue that through accretion the planet's mass could exceed that of the surrounding disk, a scenario which favors a slowing down of the planet. The planet also slows down in the non-accreting case, however, which contradicts our expectations of type II migration. This suggests that partitioning the disk into an outer and inner disk that exchange no material is an erroneous concept, at least for the planet masses considered in the work of Nelson et al. (2000). Rather, it appears that a significant flow of material can occur between the outer and inner disks through the horseshoe region, and

[7]Corresponding to a purely hydrodynamical calculation with a non-vanishing kinematic viscosity.

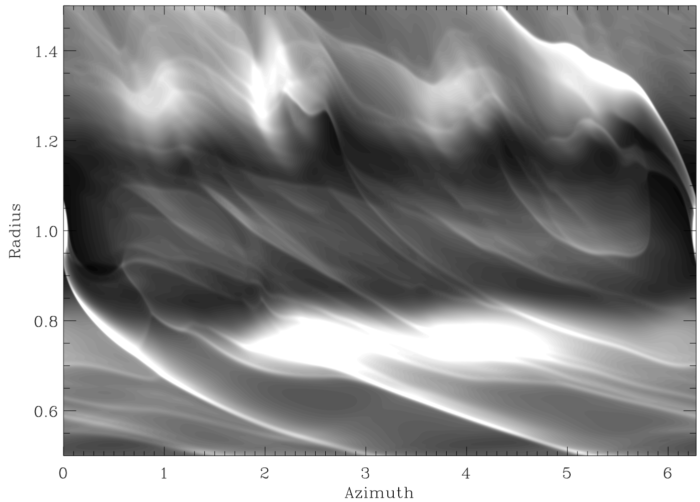

Fig. 14. The surface density of an inviscid disk with aspect ratio $h = 0.04$, perturbed by an $M_p = 1\ M_J$ protoplanet, at time $t = 50$ orbits. Vortices are apparent on both edges of the gap.

that this process decouples the evolution of the planet's semi-major axis from the viscous evolution of the disk. Readers interested in this problem are referred to the recent work by Lubow and D'Angelo (2006) about gas flow across gaps in protoplanetary disks.

If the type II migration rate of a giant planet and the viscous drift rate are of the same order, one should expect giant planet migration to stall in an inviscid disk. This expectation has not yet been confirmed by numerical experiments. When one simulates the response of an inviscid disk to the tidal perturbation of a giant planet, vortices appear along the gap edges (de Val-Borro et al., 2006). In most cases these vortices eventually coalesce into one large vortex on each gap edge. As these vortices circulate along the edges, they induce variations in the torque on the timescale of a few orbital periods. The appearance of vortices is expected at locations where the vortensity profile has an extremum (Lovelace et al., 1999; Li et al., 2000; Li et al., 2001), which can certainly happen on the gap edges. Their persistence results from a balance between two antagonist processes. The first is viscous diffusion, which tends to spread the vorticity extrema. Second, each time a vortex crosses the shock triggered by the planet, it gains a certain amount of vorticity that depends on shock properties such as the pitch angle and Mach number (Koller et al., 2003). Fig. 14 shows vortices on the edges of a gap opened by a giant planet.

Finally, we note that Ward (2003) has contemplated the possibility of outwards type II migration in viscously spreading, truncated disks. In such disks, a significant fraction of the mass in the outer region spreads outwards as it removes angular momentum from the inner regions. A giant planet located in the outward flowing part of the disk would thus undergo an outwards migration. This prediction still awaits confirmation from numerical experiments. Preliminary work by Crida et al. (2006b), who are performing global simulations of a viscously evolving disk over a large radial range (through the use of a hybrid 1D-2D grid), seems however to imply that even giant planets located beyond the critical radius migrate inwards.

4.3 Type III migration

Thus far, the torque acting on a migrating planet has been considered to be independent of the migration rate. This is true of the differential Lindblad torque. However, the corotation torque implies that some material crosses the planet's orbit at the U-turns of horseshoe streamlines. In a non-migrating case, only material trapped in the horseshoe region participates in these U-turns. In the case of a planet migrating inwards (or outwards), however, material from the inner disk (outer disk) has to execute a horseshoe U-turn if it is to flow across the co-orbital region. In doing so, it exerts a corotation torque on the planet that scales with the drift rate. We give below a simplified derivation of the corotation torque's dependency upon the drift rate $\dot{a}$. A more accurate derivation can be found in Masset and Papaloizou (2003). The main difference between these two derivations is as follows. The present derivation can be thought of as being performed in a shearing sheet model (Narayan et al., 1987), in which the corotation torque scales with the gradient of the surface density (there is no vorticity gradient in the shearing sheet). The vortensity gradient, however, as is usual for corotation torque and horseshoe drag effects, features in the derivation of Masset and Papaloizou (2003). We also note that while we emphasized the difference between horseshoe drag and corotation torque in section 4.1, we will not make this distinction here; in this case the corotation torque is dominated by the horseshoe drag of material drifting across the planet's orbit.

As in previous sections, we define x_s as the radial half-width of the horseshoe region. We recall that the amount of specific angular momentum that a fluid element near the separatrix takes from the planet is $4Bax_s$, when it switches from an orbit with radius $a - x_s$ to one with radius $a + x_s$.

The torque exerted on a planet in steady migration, with drift rate $\dot{a}$, by the inner or outer disk elements as they cross the planet's orbit on a horseshoe U-turn, to lowest order in x_s/a, is therefore

$$\Gamma_2 = (2\pi a \Sigma_s \dot{a}) \cdot (4Bax_s). \tag{4.22}$$

We retain the notation of Masset and Papaloizou (2003), where Σ_s is the surface density at the upstream separatrix. The first term in the above equation represents the mass flow rate from the inner disk to the outer disk (or vice-versa, depending on the sign of $\dot{a}$). To evaluate the sum of external torques, we consider the system of the planet and all the trapped, librating fluid elements in its co-orbital region. In other words, we take the entire horseshoe region (with mass M_{HS}) and all the circumplanetary material (with mass M_R), because these parts are engaged in simultaneous migration.

The drift rate of this system is then given by

$$(M_p + M_{HS} + M_R) \cdot (2Ba\dot{a}) = (4\pi a x_s \Sigma_s) \cdot (2Ba\dot{a}) + \Gamma_{LR}. \tag{4.23}$$

This can also be written as

$$m_p \cdot (2Ba\dot{a}) = (4\pi a \Sigma_s x_s - M_{HS}) \cdot (2Ba\dot{a}) + \Gamma_{LR}, \tag{4.24}$$

where $m_p = M_p + M_R$ is the total mass content of the circumplanetary system, which includes the planet and any circumplanetary material. For short we refer to this total as the planet mass, which is justified by the fact that material orbiting in the circumplanetary disk "belongs" to the planet, at least temporarily. Further considerations regarding the definition and extent of this system will be found in section 6.2.6. The first term in the first bracket on the R.H.S. of Eq. (4.24) is the surface area of the horseshoe region multiplied by the upstream separatrix surface density, and hence represents the mass that the horseshoe region *would* have if it had a uniform surface density equal to the upstream surface density. The second term in this bracket is the actual horseshoe region mass. Masset and Papaloizou (2003) referred to the difference between these two terms as the co-orbital mass deficit (CMD), denoted δm. (Note that we could also have included the Roche lobe mass in the co-orbital mass deficit, and used "planet mass" to mean the mass of the point-like object at the center of the Roche lobe. This choice would lead to an equivalent formulation, and the same runaway criterion.) Eq. (4.24) yields the drift rate:

$$\dot{a} = \frac{\Gamma_{LR}}{2Ba(m_p - \delta m)} \tag{4.25}$$

If we consider the range of planetary masses for which the co-orbital region is at least partially depleted, then $\delta m > 0$ and thus the drift rate given by Eq. (4.25) is always larger than the standard estimate (in which one neglects δm). This comes from the fact that co-orbital dynamics alleviate the task of the differential Lindblad torque, by displacing fluid elements from the upstream to the downstream separatrix. The angular momentum they extract from the planet by doing so always favors its migration, whether it is inwards or outwards.

As δm tends to m_p, most of the angular momentum lost by the planet and its co-orbital region is gained by circulating material as it crosses the orbit, making migration increasingly "cost effective".

We comment that the mechanism upon which type III (or runaway) migration is based can be described by the standard formalism of positive feedback loops, as shown in fig. 15.

The open loop gain is $G' = \mathcal{AB} = \delta m / m_p$, so the system stability condition $G' < 1$ here corresponds to $\delta m < m_p$. Above this threshold, one gets runaway migration. Below this threshold, the closed loop gain is given by

$$G = \frac{\mathcal{A}}{1 - \mathcal{AB}}, \tag{4.26}$$

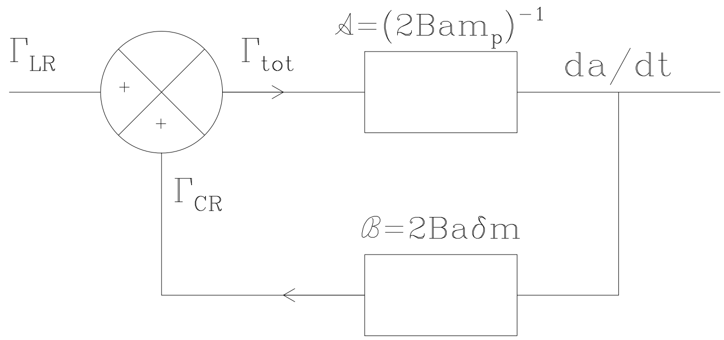

Fig. 15. Schematic representation of the positive feedback loop. The loop latency is $\sim \tau_{lib}$. The total torque felt by the planet, $\Gamma_{\rm tot}$, is the sum of the Lindblad torque $\Gamma_{\rm LR}$ and the corotation torque $\Gamma_{\rm CR}$. This yields the planetary migration rate da/dt, which exerts feedback on the value of the corotation torque through the inner branch of the loop.

which yields Eq. (4.25).

When $\delta m \geq m_p$, the above analysis (which assumes a steady migration, or constant $\dot{a}$) is no longer valid. As we shall see below, the migration enters a runaway regime. The migration rate varies strongly over time, increasing exponentially over the first few libration timescales. An analysis similar to the above calculation may be performed in this case by allowing the corotation torque to depend on the migration rate, except that now one has to take into account the delay τ between mass inflow at the upstream separatrix and its impact on the corotation torque. It takes only a fraction of a libration time for the incoming flow to reach a horseshoe U-turn and exert a torque on the planet. This delay represents the latency of the feedback loop. We can therefore write:

$$\Gamma_{CR}(t) = 2Ba\,\delta m\,\dot{a}(t-\tau), \tag{4.27}$$

where we assume that the migration is still slow enough for the corotation torque to scale with the drift rate. The corotation torque from Eq. (4.27) can then be used in the angular momentum balance equation, which reads as

$$2Bam_p\dot{a} = \Gamma_{LR}(t) + \Gamma_{CR}(t). \tag{4.28}$$

Using Eqs. (4.27) and (4.28), a first-order Taylor expansion in time of $\dot{a}(t-\tau)$ yields the following differential equation for $\dot{a}$:

$$\left(1 - \frac{\delta m}{m_p}\right)\dot{a} + \tau\frac{\delta m}{m_p}\ddot{a} = \frac{\Gamma_{LR}}{2Bm_pa}. \tag{4.29}$$

This can be rewritten as

$$\gamma\dot{a} + \xi\ddot{a} = \frac{\Gamma_{LR}}{2Bm_p a}, \tag{4.30}$$

where $\gamma = 1 - \delta m/m_p$ and $\xi = \tau\delta m/m_p$.

We note in passing that if we take $\tau = \tau_{\rm lib}/4$, where $\tau_{\rm lib} = 4\pi a/(|A|x_s)$ is the time needed to describe a full horseshoe streamline near the separatrix, then $\xi = (\pi a/|A|x_s)\delta m/m_p$. Masset and Papaloizou (2003) find, in their Eq. (A5), that $\xi = (3\pi a/4|A|x_s)\delta m/m_p$. The value they obtain for γ is the same as that used in the present analysis.

The above equation holds as long as the corotation torque scales linearly with the drift rate. It yields two different outcomes, according to the sign of the coefficients on the time derivatives of a. Its general solution is the sum of a constant value for $\dot{a}$, as given by Eq. (4.25), and the general solution to the associated homogeneous differential equation.

- If γ and ξ have same sign, then this general solution is an exponential function that decreases with time. The drift rate then approaches the value given by Eq. (4.25) over a short timescale. This is a regime of steady migration, where the main "engine" is still the differential Lindblad torque. Co-orbital dynamics alleviate its task and speed up the migration.

- If γ and ξ have opposite signs (i.e., if $\gamma < 0$, since ξ is always positive), then the general solution of the homogeneous equation associated with Eq. (4.30) is an exponential that increases with time. The migration rate increases rapidly, hence the "runaway" epithet for this regime, which is also referred to as "type III". The semi-major axis drift will speed up regardless of its direction, which depends on the initial conditions. The condition $\gamma < 0$ translates into $\delta m > m_p$. This means that for a planet to be in the type III migration regime it needs to significantly deplete its co-orbital region. Also, since the co-orbital mass deficit δm scales with the disk surface density, type III migration is favored in massive protoplanetary disks.

In the runaway regime, the e-folding time of the drift rate is $\tau_e = -\xi/\gamma = \tau\delta m/(\delta m - m_p)$. This timescale is of the same order as the libration time, or about ten orbits (depending on the planet mass and the co-orbital mass deficit). The drift rate therefore very quickly reaches large values, for which the assumption of Eq. (4.27) (that the corotation torque is proportional to the drift rate) breaks down. This linear dependence of the corotation torque on the drift rate remains valid as long as the semi-major axis varies by less than the horseshoe zone width over one libration time:

$$|\dot{a}| < \dot{a}_{\rm crit} = \frac{Ax_s^2}{2\pi a}. \tag{4.31}$$

One then has to consider a more general relationship between $\Gamma_{CR}(t)$ and the drift rate. The value of the corotation torque at a given instant t depends on $\dot{a}(t')$ for all $t' < t$, since the vortensity distribution in the co-orbital region depends on the whole migration history of the planet. This makes the problem of determining the semi-major axis evolution almost intractable, unless one resorts to either numerical simulations or simplifying assumptions. One such assumption is that the migration is steady, and that the planet always possesses a given co-orbital mass deficit. Under these conditions, the corotation torque depends only on the (constant) value of $\dot{a}$. One can therefore write the angular momentum balance equation as

$$2Bam_p\dot{a} = \Gamma_{LR} + \Gamma_{CR}(\dot{a}). \tag{4.32}$$

This is an implicit equation for $\dot{a}$. The number of roots depends on the function $\Gamma_{CR}(\dot{a})$.

Under the assumption that the planet possesses a given co-orbital mass deficit, the corotation torque depends linearly on the drift rate provided that migration is slow, i.e., that $\dot{a}$ satisfies inequality (4.31). It then reaches a maximum and slowly decays for larger values of $\dot{a}$ (Masset and Papaloizou, 2003). Note, however, that the exact functional dependence of Γ_{CR} on $\dot{a}$ in the fast migration regime ($|\dot{a}| > \dot{a}_{\rm crit}$) depends on the vortensity depletion profile of the co-orbital region. This is quite different from the slow migration regime, in which the corotation torque depends on depletion only by way of the co-orbital mass deficit. In particular, an examination of Fig. 9 in Masset and Papaloizou (2003) shows that the corotation torque peaks at a slightly larger value than what extrapolation of the linear trend would predict for $\dot{a} = \dot{a}_{\rm crit}$, then decays at large values of $\dot{a}$. These results are different from the results presented in Fig. 16, which were obtained using a planet mass and disk parameters identical to those of Masset and Papaloizou (2003). The resolution is slightly higher, however, in these new results. The most important difference in the new calculations (which were obtained by imposing a disk drift rather than a planet drift, as explained in section 5.6 of Masset and Papaloizou (2003)) is that no preliminary calculations are performed in the absence of a planet/disk drift during which a co-orbital dip and co-orbital mass deficit can be created. Rather, a mass deficit is formed as the planet and disk drift relative to each other. When this drift is large, it is harder for the planet to evacuate a large amount of mass from its co-orbital region. This illustrates how the function $\Gamma_{CR}(\dot{a})$ depends on the manner in which the co-orbital mass deficit has been acquired. Nevertheless, the new results of Fig. 16 share a number of features with the older results presented by Masset and Papaloizou (2003):

- The total torque displays an affine dependence on $\dot{a}$ in the slow migration regime.
- Although their peak values are different, they have the same order of magnitude.
- The torque decays beyond this peak value. The reason for this is twofold: when the co-orbital mass deficit is acquired during the drift, the co-orbital mass deficit is small for large drift rates. The decay is also present, however, when the co-orbital mass deficit is acquired prior to the drift. This occurs when the drift time across the horseshoe region is of the same order as

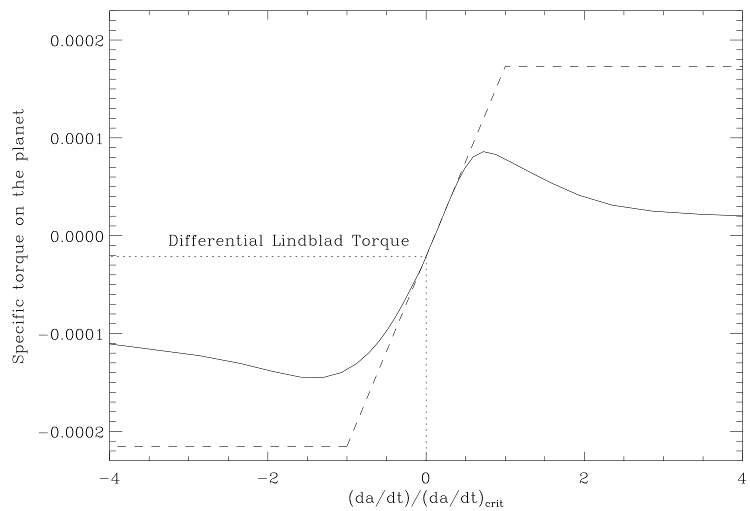

Fig. 16. The total specific torque acting on a Saturn-mass planet in a disk with $h = 0.03$ and surface density profile $\Sigma \propto r^{-3/2}$. The uniform kinematic viscosity is $\nu = 10^{-5}$, while the surface density is 10^{-4} at the planet location. The abscissa shows $\dot{a}/\dot{a}_{\rm crit}$, where $\dot{a}_{\rm crit}$ is evaluated using Eqs. (4.31) and assuming $x_s/a = 0.11$. The dashed line sketches the naive expectation of a linear dependence in the slow migration regime, and a plateau in the fast migration regime.

or shorter than the horseshoe U-turn time. This provides a cutoff on the corotation torque, which accounts for this decay.

Once the corotation torque's dependence on the migration rate is known, through either a toy model or numerical simulations, one can look for the roots of Eq. (4.32). This can be done for any disk mass, since if everything else is fixed the Lindblad torque and the corotation torque are proportional to the surface density of the disk. Depending on the relative slopes of the inertia term (L.H.S. of Eq. [4.32]) and the torque at the origin (R.H.S. of Eq. [4.32]), one can have either one or three roots as depicted in Fig. 17.

When one performs a root search on the results presented in Fig. 16, one obtains the results displayed in Fig. 18. This shows the roots in the $(\Sigma/\Sigma_{\rm crit}, [\dot{a}/\dot{a}_{\rm crit}/(\Sigma/\Sigma_{\rm crit})])$ plane. In this plot, if migration were not modified by the co-orbital dynamics, one would simply get a horizontal line giving the slope of the dependence of $\dot{a}$ on Σ. This is the asymptotic behavior that one gets at low masses. Even for $\Sigma < \Sigma_{\rm crit}$, however, one can see that migration speeds up as one approaches the critical surface density because the co-orbital mass deficit increases. A planet located on the unstable branch (dashed line) will switch to the upper or lower stable branch. As long as it remains in the slow migration regime (shaded area), where the corotation torque scales with the drift rate, the planet will recede from the unstable branch

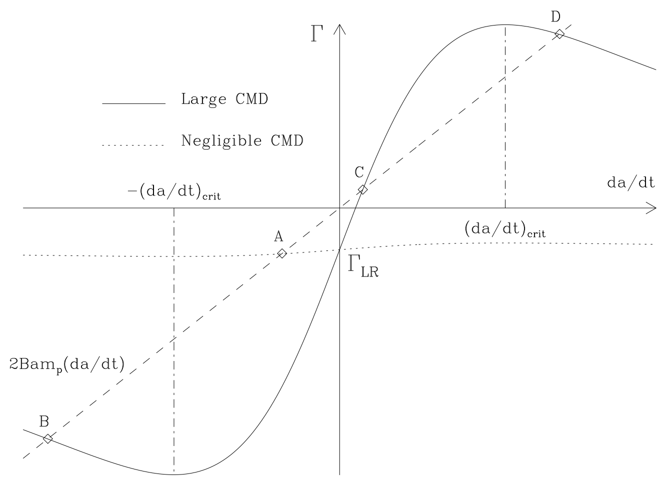

Fig. 17. The solid curve shows the total torque on a planet in a massive disk (with a large co-orbital mass deficit) as a function of the drift rate, assuming steady migration. For $|\dot{a}| \ll \dot{a}_{\rm crit}$ the torque exhibits a linear dependence on $\dot{a}$ (this has been accurately confirmed by numerical experiments). The dotted line shows the torque in a low-mass disk (i.e., with a negligible coorbital mass deficit). In this case the torque is almost independent of the migration rate and is always close to the differential Lindblad torque Γ_{LR}. The dashed line represents the rate at which the planet gains angular momentum as a function of $\dot{a}$, assuming a circular orbit. For any given situation, the steady migration rate of the planet is given by the intersection of the dashed line with the torque curve. For the low-mass disk, the intersection point A is unique and stable. It yields a negative drift rate, controlled by the differential Lindblad torque. For the high-mass disk case (the runaway or type III case), there are 3 points of intersection (B, C, and D). The central point (C) is unstable, while the extreme points (B and D) are stable and correspond to the maximum runaway drift attained by the planet inwards (point B, $\dot{a} < 0$) or outwards (point D, $\dot{a} > 0$).

along the vertical at an exponential rate, as given by the solutions of Eq. (4.30). Note that the appearance of three roots occurs for Σ slightly larger than $\Sigma_{\rm crit}$, rather than for $\Sigma = \Sigma_{\rm crit}$. This is due to the fact that the outwards root ($\dot{a} > 0$) appears when the dashed line is tangential to the torque curve, or equivalently when points C and D in Fig. 17) are superimposed. The slope of the dashed line is then slightly inferior to the slope of the torque curve at $\dot{a} = 0$, so δm is slightly larger than m_p. In the particular case of Fig. 18, one has three roots for $\Sigma > 1.38\Sigma_{\rm crit}$ and one root otherwise. The aspect of the co-orbital mass deficit in the slow and fast migration regimes is shown in Fig. 19. In the fast migration regime, the underdense trapped gas only covers a small fraction of the co-orbital

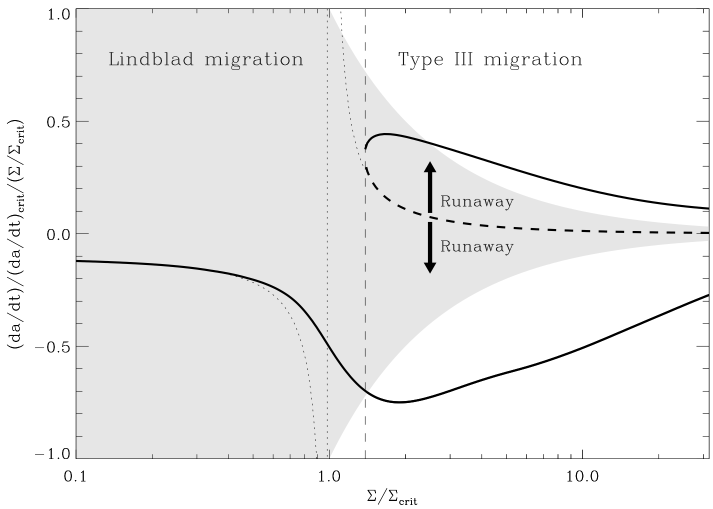

Fig. 18. The normalized steady migration rate as a function of disk mass (in units of the critical disk mass), for the series of calculations presented in Fig. 16. The thick solid branches represent the stable solutions, while the thick dashed branch represents the unstable solution. For low-mass disks there is only one steady drift rate, which is given by the differential Lindblad torque, hence the qualification "Lindblad migration". ("type I migration" would be incorrect, since the surface density profile is perturbed; "steady migration" would also be incorrect, as by hypothesis the migration is steady even for high-mass disks.) The dotted hyperbola is obtained from Eq. (4.25), and connects to the unstable branch in the high-mass regime. The shaded area shows the region of slow migration ($|\dot{a}| < \dot{a}_{\mathrm{crit}}$).

region since the drift time across this region is shorter than the libration time. The shape of the trapped deficit is approximately parabolic in the (φ, r) plane. This can be understood using (for example) the toy model presented by Masset (2001) in that work's section 3.2[8]. This kind of behavior is observed whenever the relative drift between the planet and disk is fast (i.e., faster than $\dot{a}_{\mathrm{crit}}$). An example for viscous disks is given by Masset (2002) in that work's Figs. 7 and 8.

The critical disk mass (above which a planet of given mass undergoes runaway migration) depends on the disk aspect ratio and effective viscosity. This limit has been worked out by Masset and Papaloizou (2003) for various disk aspect ratios and the kinematic viscosity $\nu = 10^{-5}$. We reproduce in Fig. 20 the type III migration domain for a disk with $H/r = 0.04$. We comment that in this work the resulting critical disk mass corresponds to $m_p = \delta m$, not the slightly larger disk

[8]This toy model was developed in the context of viscous drift of the disk, but it is also valid for any relative drift between the disk and the planet.

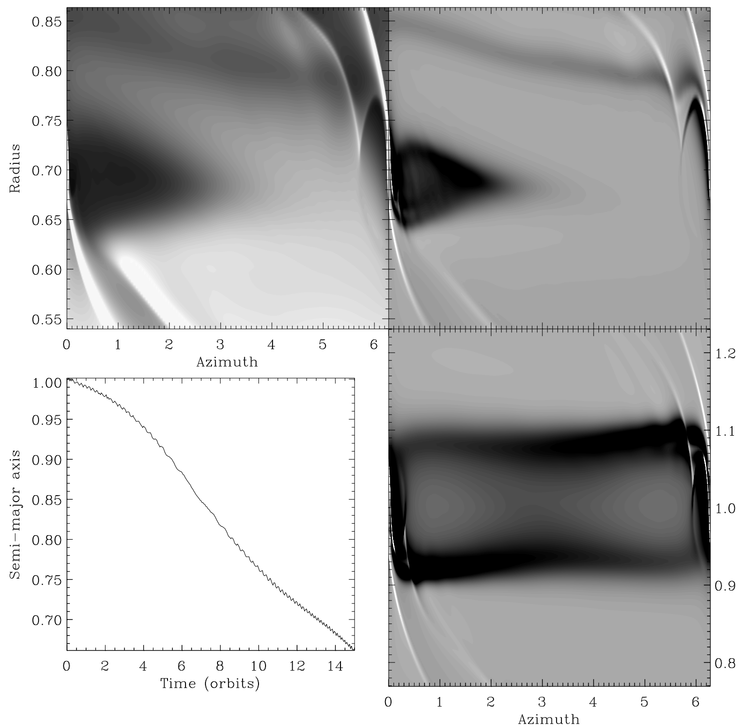

Fig. 19. An example of type III migration for a Saturn-mass planet in a disk with $\Sigma \approx 3\Sigma_{\rm crit}$. The planet is held on a fixed circular orbit for 64 orbits, during which time it acquires a co-orbital mass deficit, then is allowed to migrate freely. The lower right plot shows the distribution of vortensity just before this release, with a negative gray scale (i.e., darker regions indicate higher vortensity). There is an excess of $(\nabla \times \mathbf{v})_z/\Sigma$ in the co-orbital region, and hence a deficit of $\Sigma/(\nabla \times \mathbf{v})_z$. The upper right plot shows the vortensity 13 orbits after the planet's release, while the upper left plot shows the surface density at the same time (on a positive scale). The lower left plot shows the time evolution of the semi-major axis, which displays an initial acceleration followed by saturation to a rapid drift rate of about $0.03a$ orbit^{-1}.

mass (as explained above) for which there exist several steady migration rates. We also stress that the CMD in these calculations is acquired during a prior period, when the planet is held on a fixed circular orbit.

Fig. 20 shows that type III migration is most likely for Saturn-mass planets in sufficiently massive disks (slightly more massive than the MMSN at 10 AU). Papaloizou (2005) has performed local shearing box three dimensional calculations that essentially confirm these findings. However, we recall that the type III migration domain and the diagram given in Fig. 18 both depend heavily upon the

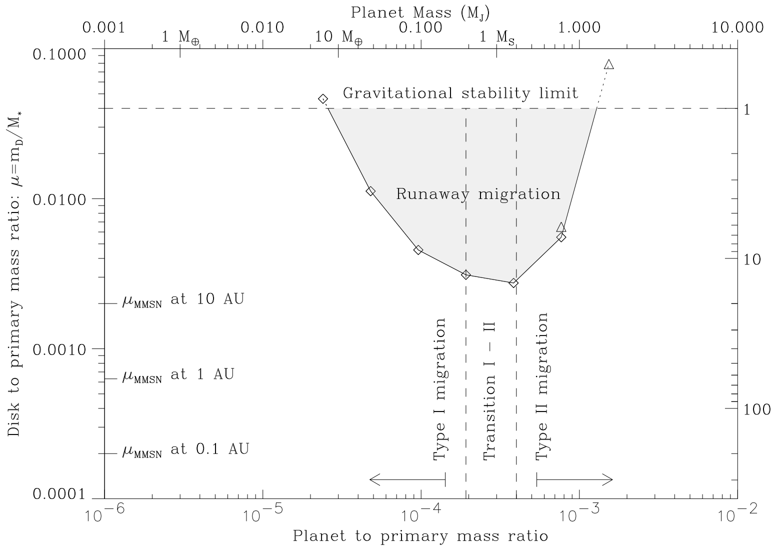

Fig. 20. The runaway limit domain for a disk with $h = 0.04$, $\nu = 10^{-5}$, and surface density profile $\Sigma \propto r^{-3/2}$. The variable $m_D = \pi\Sigma r^2$ is featured on the y-axis. It is meant to represent the local disk mass, and therefore depends on the radius. The right-hand axis tick marks represent Toomre's Q parameter. Runaway migration is most likely for Saturn mass planets, and will occur in disks a few times more massive than the Minimum Mass Solar Nebula. Runaway migration is impossible for massive planets ($M > 1\ M_J$), as the surface density is very low on the upstream separatrix. Low-mass objects ($M < 10\ M_\oplus$) do not deplete their co-orbital region, and therefore also cannot undergo runaway migration.

manner in which a planet acquires its co-orbital mass deficit. If the planet is held on a fixed circular orbit longer than necessary to open the dip (see section 4.2), then the co-orbital mass deficit will depend on the planet mass, the disk thickness, and the disk viscosity. The larger the viscosity and/or disk thickness, the shallower the dip and the smaller the co-orbital mass deficit.

While Figs. 16 and 18 show that type III migration can occur outwards ($\dot{a} > 0$) in principle, Fig. 18 shows that in order for this to occur a planet must begin with a significant positive drift rate (i.e., it must lie "above" the thick dashed line). Otherwise it will reach the lower branch, and eventually undergo an inwards type III migration. Since the drift rate needs to be maintained on the order of the libration timescale for the planet to leave an imprint on the co-orbital vortensity distribution, the "seed migration" to get an outwards runaway migration needs to be sustained over a few tens of orbits. Masset and Papaloizou (2003) have investigated whether one could indeed expect to observe rapid outwards migration in Saturn-mass planets. They have succeeded in obtaining outwards runaway episodes for shallow disk profiles ($\Sigma \propto r^{-\zeta}$, with $\zeta = 0$ or $\zeta = 1/2$), as these natu-

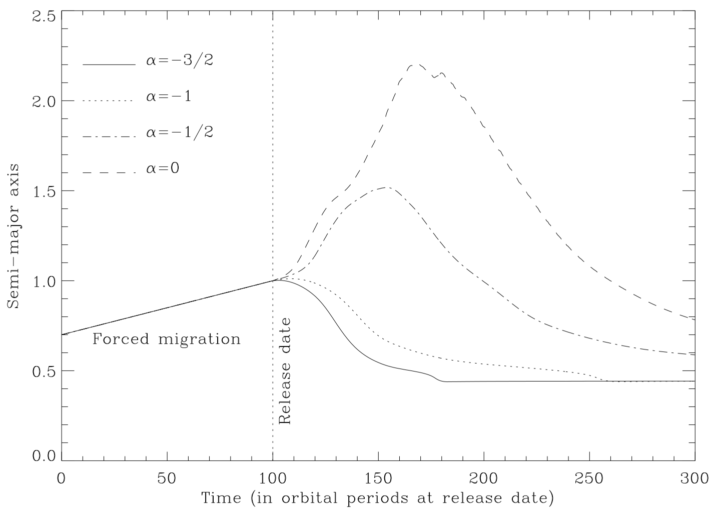

Fig. 21. An outward type III migration is observed for the two shallowest profiles, which increase the semi-major axis respectively by a factor 1.5 and 2.2 over a few tens of orbits.

rally yield a co-orbital mass deficit that increases as the planet migrates outwards. They have also found, however, that outwards migration cannot be sustained indefinitely. Rather, at some point the co-orbital mass deficit is lost and the sense of migration reverses. This effect can be seen in Fig. 21, which shows the release of a planet with $a = 1$ that was previously forced to migrate outwards for 100 orbits. At present there is no criterion that can predict the loss of the co-orbital mass deficit, which is linked to the time variation of $\dot{a}$. In a frame that is comoving and corotating with the planet the streamlines are not closed, which leaves open the possibility that the co-orbital mass deficit can leak into the outer or inner disk.

In the analysis exposed in this section, accretion onto the planet has been neglected. All the disk material that crosses the upstream separatrix is assumed to eventually flow across the downstream separatrix. However, the planet mass at which type III migration is assumed to occur is much larger than the mass threshold for runaway gas accretion onto the planetary core. A fraction of the gas flowing across the co-orbital region should thus be retained by the planet. On the other hand, the mass flow rate across the orbit during a type III episode is extremely high. During the episode shown in Fig. 19, for instance, this rate amounts to $\dot{M} \sim 3 - 4 \cdot 10^{-4}\ M_{*}.\mathrm{orbit}^{-1}$ or almost half a Jupiter mass per orbit. This is much more than the planet can accrete, so only a very small fraction of material crossing the orbit should be diverted onto the planet. In this case, the above analysis should remain essentially valid.

We close this section by mentioning a recent work by D'Angelo et al. (2005), who investigate the dependence of co-orbital torques on the migration rate by means of two- and three-dimensional calculations. They use a resolution much higher than that found in the work of Masset and Papaloizou (2003). The former work essentially finds that if one takes into account the entire content of the circumplanetary material in the torque evaluation, the co-orbital corotation torques do not depend on the drift rate, or at most depend on it very weakly. This conclusion contradicts the findings of Masset and Papaloizou (2003). We stress, however, that both series of calculations lack one essential physical ingredient: the gas self-gravity. While this should be of only minor importance when the mass of the circumplanetary material is small compared to that of the planet (i.e., at low resolution), it should be of considerable relevance in the high resolution case when a massive circumplanetary disk builds up. We therefore restrict ourselves to the statement that three-dimensional, high-resolution numerical simulations including gas self-gravity are needed to properly assess the frequency of type III migration, and refer the reader to section 6.2.4 for a list of numerical artifacts that might alter the results of calculations without self-gravity.

4.4 Stochastic migration

In the previous sections, the protoplanetary disk was considered to be laminar while the accretion of material onto the central object was ensured by an *ad hoc* kinematic viscosity chosen to agree with the mass accretion rate measured for T Tauri stars. The molecular viscosity of protoplanetary disks appears to be insufficient by many orders of magnitude, however, to reproduce the accretion rates typically measured. The source of the high effective viscosity in these disks is thought to be turbulence, although alternate hypotheses have also been contemplated. One example is an outwards flux of angular momentum, resulting from the background flow's interaction with a large collection a low-mass planet wakes. The effect of such a flux can be described in the average sense and on large scales by an effective viscosity term (Goodman and Rafikov, 2001). Turbulence can have a number of origins. Magnetorotational instability (MRI), for example, has been identified as a powerful source of MHD turbulence in magnetized disks (Balbus and Hawley, 1991; Hawley and Balbus, 1991; Hawley and Balbus, 1992). Other sources have been suggested, such as hydrodynamic turbulence (Dubrulle et al., 2005; Klahr and Bodenheimer, 2003) or turbulence resulting from a Kelvin-Helmholtz instability, which is due to the vertical gas shear arising from dust sedimentation (Johansen et al., 2006). Only MHD turbulence, however, has been intensively studied by numerical simulations in the context of planet–disk interactions. We thus have torque statistics only for this case. In the current section, we will focus exclusively on the interaction of a planet with a disk invaded by MHD turbulence.

Magnetorotational instability can develop only in regions of the disk where the matter and magnetic field are coupled, which requires a sufficiently high (albeit weak) ionization rate. In the planet-forming region ($1 - 10$ AU), it is thought that only the upper layers of the disk are ionized by X-rays from the central star or cosmic rays (Gammie, 1996; Fromang et al., 2002). The bulk of the disk, however, should be ionized outside this region. This has led Gammie (1996) to the concept of layered accretion: the upper layers of the region between 1 and 10 AU participate in accretion onto the central star, whereas its magnetically inactive equatorial parts, usually called the *dead zone*, do not participate in the inwards flow of disk material.

There already exist a large number of works describing numerical simulations that self-consistently describe an MHD turbulent disk with embedded planets (Nelson and Papaloizou, 2004; Papaloizou et al., 2004b; Nelson and Papaloizou, 2003; Nelson, 2005; Winters et al., 2003). They have provided valuable information on the tidal interaction between a planet and the disk. They exclusively consider a fully magnetized disk (hence with no dead zone), however, without any vertical stratification for reasons of computational cost. Fromang and Nelson (2006) have recently performed global MHD simulations of stratified, turbulent disks. However, they have not yet considered the interaction of an embedded planet with such a disk.

Not surprisingly, the torque felt by a planet in a turbulent disk displays large temporal fluctuations. One can assign an order of magnitude to the amplitude of these fluctuations by considering an overdense region of size H, located at a distance H from the planet such that the perturbed density in this region is of the same order as the unperturbed density. This yields an order of magnitude for the torque fluctuations of $G\Sigma a$ (Nelson and Papaloizou, 2004; Nelson, 2005).

Nelson and Papaloizou (2003) and Papaloizou, Nelson and Snellgrove (2004b) have investigated the flow morphology in the vicinity of a giant planet that opens a gap, and have verified that the gap opening is controlled by the same dimensionless parameter that controls clearance in a Navier–Stokes disk (see section 4.2).

Nelson and Papaloizou (2004) and Nelson (2005) have investigated the migration of embedded planets in turbulent disks. Laughlin et al. (2004) have also investigated this problem, but rather than tackling it through self-consistent numerical simulations they performed a two-dimensional calculation which mimicked the effects of turbulence using a time-varying, non-axisymmetric potential acting on the gas disk, rather than directly on the planet. They calibrate the properties of this potential using a preliminary 3D MHD calculation with no embedded planet. The migration of low-mass planets embedded in turbulent disks under this model is significantly different from the type I migration expected for laminar disks. The large torque variations due to turbulence induce the planet's semi-major axis to evolve on a random walk rather than systematically decay.

One question that is still open is whether the total torque felt by a planet in a turbulent disk can be decomposed into a laminar torque and the effect of fluctuations arising from the turbulence. We shall call the latter component the stochastic torque.

One might expect that the time average of the stochastic torques is negligible compared to the total mean torque (which might be the same as the laminar torque, but this is still unknown), provided that this average is performed over a time interval that is much longer than the turbulence recurrence time. Under this assumption, the behavior of the planet should exhibit a systematic trend reminiscent of type I migration. Nelson (2005) has investigated the statistical properties of these torque fluctuations, finding significant power at low frequencies, corresponding to timescales comparable to the simulation time. As a consequence, in many of his calculations no systematic trend is observed; stochastic migration dominates type I migration over the entire run time of his calculations, or about 150 orbits. The reason for such significant power at very low frequencies is still unknown.

We also note that the amplitude of the specific stochastic torque is independent (or nearly so) of the planet mass, whereas the specific wake torque scales with the planet mass. Hence, above some planet mass threshold systematic effects should dominate stochastic effects (averaged over an appropriate time interval) while the opposite should hold below this threshold. We note that this critical value should not depend on the disk mass, since the wake and stochastic torques both scale with the disk mass. Nelson (2005) found that for planets up to $\sim 10\ M_\oplus$ the stochastic migration overcomes the systematic trend (over a simulation run time of 150 orbits), whereas systematic effects are dominant for larger masses. We mention however the recent work by Fromang and Nelson (2006), who argue that density fluctuations are smaller in a stratified, turbulent disk than in the unstratified models currently used to assess stochastic torques. This argument suggests that systematic effects could be dominant at masses even lower than $10\ M_\oplus$.

As pointed out by Johnson et al. (2006), if the turbulence has a finite correlation time then the stochastic (or diffusive) migration of low-mass planets can be reduced to an advection-diffusion equation. They show that diffusion always reduces the mean migration time of the planets, although a fraction of them still "survive" an extended period of migration.

5 Eccentricity evolution of protoplanets

When a planet possesses some finite eccentricity e, the azimuthal Fourier transforms of its potential contain terms that do not corotate with the planet and can in principle excite a response in the disk. (A wave-like response at the Lindblad resonances, and an evanescent response at the corotation resonances.) The angular momentum and energy imparted to the disk by these new components will affect the angular momentum and energy budget of the planet. The ratio of the disk's incoming energy flux to its incoming angular momentum flux at these resonances is not, however, equal to the ratio of the planet's energy variation to its angular momentum variation. This follows because the forcing pattern frequency is not the same as the orbital frequency. The planet will react to this imbalance by adjusting its eccentricity. We shall now see how some of these new resonances can excite the eccentricity, while others dampen it. We then discuss the total budget in two different cases (for low-mass objects in section 5.2, and for giant planets in section 5.3).

We consider the angular momentum and energy budget of a planet with mass M_p, semi-major axis a, and eccentricity e, which is assumed to be on a Keplerian orbit. Its total energy is E_p and its angular momentum is J_p:

$$E_p = -\frac{GM_* M_p}{2a} \tag{5.1}$$

$$J_p = M_p \sqrt{GM_* a(1-e^2)} \tag{5.2}$$

Their time derivatives are therefore

$$\dot{E}_p = \frac{GM_* M_p}{2a^2} \dot{a} \tag{5.3}$$

and

$$\dot{J}_p = \frac{M_p}{2} \sqrt{\frac{GM_*(1-e^2)}{a}} \dot{a} - \frac{\Omega_p M_p e a^2}{\sqrt{1-e^2}} \dot{e}, \tag{5.4}$$

which are related as follows:

$$\dot{J}_p = \Omega_p^{-1} \sqrt{1-e^2} \dot{E}_p - \frac{\Omega_p M_p e a^2}{\sqrt{1-e^2}} \dot{e}. \tag{5.5}$$

We assume in the following discussion that the planet excites only one disturbance in the disk, with pattern frequency Ω_d. If one labels the energy and angular momentum fluxes into this disturbance as F_E and F_H, then energy and angular momentum conservation respectively yield the conditions

$$\dot{E}_p + F_E = 0 \tag{5.6}$$

and

$$\dot{J}_p + F_H = 0. \tag{5.7}$$

We also have the following general relationship between the energy flux, the angular momentum flux, and the pattern speed of the disturbance:

$$F_E = \Omega_d F_H \tag{5.8}$$

By combining Eqs. (5.5) through (5.8), one can arrive at the following equation:

$$\frac{M_p}{2} \frac{\Omega_p a^2}{\sqrt{1-e^2}} \frac{de^2}{dt} = \left(1 - \frac{\Omega_d}{\Omega_p}\sqrt{1-e^2}\right) F_H. \tag{5.9}$$

Eq. (5.9) relates the time variation of e^2 to the torque F_H exerted on the disk by a perturbing potential with pattern frequency Ω_d. We note that the azimuthal wavenumber m does not appear in this equation, which applies to *any* disturbance with pattern speed Ω_d. If F_H is unknown, however, it may be useful to consider the azimuthal components of the perturbing potential separately and make use of Eq. (3.3) or Eq. (3.9). Before applying this equation to the so-called first-order resonances, where a planet with finite eccentricity excites a disk response, it is of interest to consider the impact of the principal resonances (those which have already been extensively considered in section 3) where the planet triggers a response even on a circular orbit. To address this question we first assume that the planet possesses a small eccentricity e, and then expand Eq. (5.9) to second order in e. Since we are now considering the principal resonances, we have $\Omega_d = \Omega_p$. This yields the equation

$$\frac{1}{e}\frac{de}{dt} = \frac{F_H}{2M_p\Omega_p a^2}. \qquad (5.10)$$

As F_H is the torque of disturbances with pattern speed Ω_p, it corresponds to the wake torque (and is also the torque exerted by the perturber on the disk). It is therefore (generally) positive, and this is also the torque that makes the planet migrate (generally) inwards. The quantity $F_H/(M_p a\Omega_p/2)$ is also $-\dot{a}$ in a Keplerian disk, assuming the eccentricity is small enough that only torques exerted at principal resonances drive the migration. We therefore have $\dot{e}/e = -(1/4)\dot{a}/a$. Notwithstanding the role of first-order resonances, which we shall study in section 5.1, the principal resonances will also drive (if migration is inwards) or dampen (if migration is outwards) the eccentricity over a timescale that is four times the migration timescale (Goldreich and Sari, 2003). One can also consider the roles of various resonances separately. The principal outer Lindblad resonances, which have $F_H > 0$, excite the eccentricity; the principal inner Lindblad resonances, which have $F_H < 0$, dampen the eccentricity. Finally, the principal (co-orbital) corotation resonances excite the eccentricity if the gradient of vortensity is negative at the corotation radius, and dampen it otherwise. Since planets generally migrate inwards, their eccentricity will be excited by the principal resonances. The timescale for this excitation is, however, rather long. As we shall see in the next section, it is completely dominated by the effect of the first-order resonances.

5.1 First-order resonances

When the planet has a finite eccentricity e, some of its m-fold components have a pattern speed different from the planet's. We will not present a tedious derivation of the amplitude of these terms, which can be found in the literature (Goldreich and Tremaine, 1980). For our purposes, it suffices to know that in addition to the potential terms with pattern speed Ω_p (which exist even if the orbit is circular, and have already been mentioned in section 3), there are also potential terms that scale with e and have pattern speeds of $\Omega_p \pm \kappa_p/m$, where κ_p is the planet epicyclic frequency. Here is a qualitative justification of this statement: a planet with finite eccentricity e describes an epicycle counter to its rotation, with frequency κ_p, as seen in the frame that corotates with the planet's guiding center (the corotating frame). In this frame all the azimuthal Fourier components therefore oscillate with period $2\pi/\kappa_p$, and the temporal Fourier transform thus involves frequencies that are multiples of $\pm\kappa_p$. In particular, when e is small the potential variation at a given location in the corotating frame is sinusoidal in time. The temporal Fourier transform of a given azimuthal potential component essentially amounts to its average value plus the fundamental mode, with frequency $\pm\kappa_p$ in the corotating frame. This frequency translates into a pattern frequency of $\pm\kappa_p/m$ in the corotating frame, and hence a pattern frequency of $\Omega_p \pm \kappa_p/m$ in the inertial frame.

We shall now call the resonances (Lindblad and corotation) of these potential components the first-order resonances, since the amplitude of the perturbing potential is first-order in the eccentricity. We will refer to a potential component with pattern speed $\Omega_p + \kappa_p/m$ as a fast first-order term. Components with pattern speed $\Omega_p - \kappa_p/m$) will be referred to as slow first-order terms.

We can now locate the Lindblad and corotation resonances of a first-order term. The Lindblad resonances are found by noting that the Doppler shifted frequency of the perturbing term is equal to $\pm\kappa$, the local epicyclic frequency:

$$m\left(\Omega_p \pm \kappa_p/m - \Omega\right) = \pm\kappa, \tag{5.11}$$

where a $+$ sign on the R.H.S. refers to the OLR and a $-$ sign refers to the ILR. The potential is Keplerian, which implies that $\Omega_p = \kappa_p$ and $\Omega = \kappa$, so we are led to the following result for the fast term:

$$\Omega = \frac{m+1}{m \pm 1}\Omega_p. \tag{5.12}$$

For the slow term, we get

$$\Omega = \frac{m-1}{m \pm 1}\Omega_p. \tag{5.13}$$

Similarly, we can find the corotation resonances of the fast and slow terms by substituting $\pm\kappa$ for 0 on the R.H.S. of Eq. (5.11). We find

$$\Omega = \frac{m \pm 1}{m}\Omega_p, \tag{5.14}$$

where a $+$ ($-$) sign on the R.H.S. refers to the fast (slow) term. As one can see, the OLR of the fast term and the ILR of the slow term are both given by $\Omega = \Omega_p$; i.e., they both lie at the corotation radius of the planet. These are called the coorbital Lindblad resonances. It is instructive to consider the ILR location for the principal Fourier component with wavenumber $m+1$. It is given by the equation

$$\Omega = \frac{m+1}{m}\Omega_p, \tag{5.15}$$

and hence coincides with the corotation resonance of the fast first-order term with wavenumber m. Similarly, the OLR location of the principal Fourier component with wavenumber $m-1$ is given by

$$\Omega = \frac{m-1}{m}\Omega_p, \tag{5.16}$$

and hence coincides with the corotation resonance of the slow first-order term with wavenumber m. The effect of each first-order Lindblad resonance on the

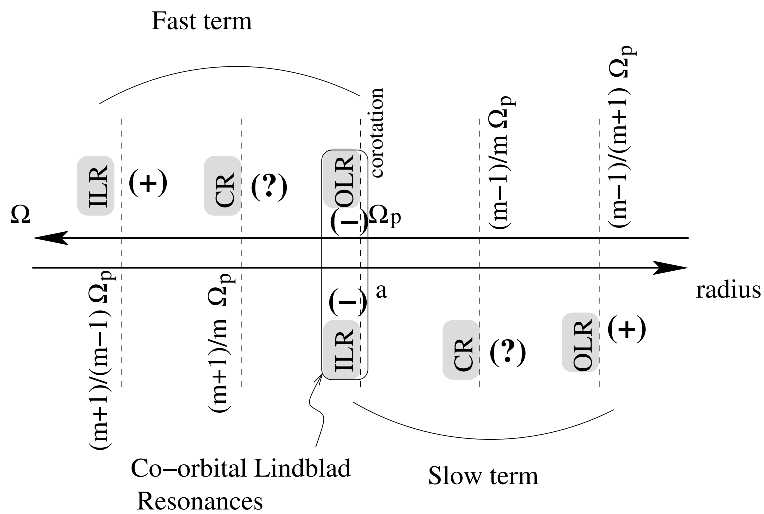

Fig. 22. Resonances of the first-order potential components with azimuthal wavenumber m. The co-orbital Lindblad resonances dampen the eccentricity as indicated by the $(-)$ signs, while the external Lindblad resonances (the ILR of the fast term and OLR of the slow term) excite it as indicated by the $(+)$ signs. The roles of the two corotation resonances cannot be determined *a priori*, and depend on the vortensity profile.

eccentricity is found by using Eq. (5.9). Taking into account Eq. (3.3) and the fact that the perturbing potential scales as GM_pe/a, one can show that $F_H = \lambda(GM_p^2\Sigma a/M_*)e^2$. In this equation λ is a dimensionless coefficient that depends on the resonance; it is positive at an OLR, and negative at an ILR. Eq. (5.9) therefore yields

$$q^{-1}\mu_D^{-1}\frac{T_0}{2}\frac{d\log e}{dt} = \left(1-\frac{\Omega_d}{\Omega_p}\right)\lambda, \tag{5.17}$$

where we have used the fact that $\Omega_d \neq \Omega_p$. The sign of $d\log e/dt$ is the same as that of $(\Omega_p - \Omega_d)\lambda$. The eccentricity is therefore *damped* by the disk at the OLR of the fast term and at the ILR of the slow term, i.e., at the co-orbital Lindblad resonances. Conversely, the eccentricity is excited at the OLR of the slow term and at the ILR of the fast term. The role of a first-order corotation resonance depends on the vortensity gradient at its location. Fig. 22 sums up the locations and effects of the first-order resonances.

5.2 Eccentricity damping of low-mass objects

The eccentricity evolution of an embedded object whose mass is sufficiently small not to alter the disk's surface density profile can be determined by summing the contributions of all first-order resonances. As we have seen, the external Lindblad resonances excite the eccentricity while the co-orbital Lindblad resonances dampen it. The torque at the co-orbital resonances, however, dominates the torque at the external resonances simply because the amplitude of the perturbing potential is largest at the orbit. Artymowicz (1993a) has found that the damping of eccentricity by the co-orbital Lindblad resonances overcomes any excitation due to the external resonances by roughly a factor of 3; i.e.,

$$0 > \frac{1}{e}\frac{de}{dt}\bigg|_{cLR} \approx -3\,\frac{1}{e}\frac{de}{dt}\bigg|_{eLR}. \tag{5.18}$$

In addition to the first-order Lindblad resonances, the effect of the first-order corotation resonances should also be included if they are not saturated. (It is highly unlikely that they are saturated provided that e is small, the planet is a type I migrating object, and the disk has $\alpha \sim$ a few 10^{-3}.) Their effect has been found to be negligible, however, compared to the effect of the first-order Lindblad resonances (Ward, 1988; Artymowicz, 1993a). In addition, the contribution of the inner corotation resonance should approximately cancel out the contribution of the outer corotation resonance if the vortensity profile is sufficiently smooth. This condition ensures that the corotation torques of the fast and slow potential components are of similar strength. (While both torques should have the same sign, their respective potential pattern speeds are slower and faster than the planet's orbital frequency, and will yield opposite contributions to the eccentricity.)

From the above discussion, one can see that the net effect of first-order resonances on a low-mass planet will be to dampen the eccentricity. The timescale for this damping is rather short. Like the migration timescale, it scales with the inverse of the planet mass. However, the timescale for circularization is about 100 times shorter than the migration timescale (Artymowicz, 1993a). This fact justifies our earlier approximation that the migration of embedded planets takes place on a circular orbit, and shows that the principal resonances make a negligible contribution to the eccentricity driving.

5.3 Eccentricity evolution of giant planets

Among the puzzles raised by the statistics of extrasolar giant planets is the origin of their eccentricities. The eccentricities of extrasolar giant planets with periods larger than ~ 10 days exhibit an important scatter. A few systems have values as extreme as 0.9, but the eccentricities of most long-period planets are distributed almost uniformly between 0 and $0.6-0.7$. Several explanations have been envisaged to account for these eccentricities, such as planet-planet interactions (Rasio and Ford, 1996; Ford et al., 2001), external perturbations due to distant binary companions or passing stars (Holman et al., 1997; Mazeh et al., 1997), and planet–disk interactions (Goldreich and Sari, 2003; Ogilvie and Lubow, 2003, and references therein). In this section we contemplate only this last possibility, as alternative explanations do not enter into the framework of this chapter.

The main difference between this analysis and the previous discussion (section 5.2) will be that a giant planet opens up a clean (i.e., low residual surface density) gap in the disk. This has two important consequences:

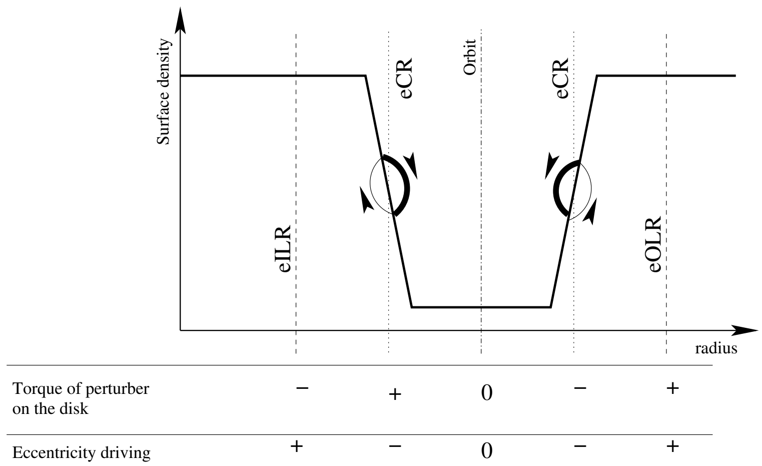

Fig. 23. Location of the first-order external Lindblad resonances (dashed lines) and first-order corotation resonances (CR; dotted lines) with respect to the gap. The inner first-order CR exerts a positive torque on the disk, because more material gets promoted to a higher specific angular momentum than gets degraded to a lower specific angular momentum. This exchange is sketched by the arrows. The opposite is true of the outer first-order CR. The sign of the eccentricity driving can be determined using Eq. (5.17); The first-order CRs are found to dampen the eccentricity.

- The co-orbital Lindblad resonances, which are a powerful source of circularization, are deactivated.
- The corotation resonances, which share their locations with the principal Lindblad resonances, lie on the edges of the gap and therefore at locations where there is a steep vortensity gradient. These gradients (at the outer gap edge and at the inner gap edge) thus yield a corotation torque that dampens the eccentricity. This is illustrated in Fig. 23.

The work of Goldreich and Tremaine (1980) as well as that of Goldreich and Sari (2003), which neglect the possible saturation of the corotation resonances, have shown that the damping effect of the corotation resonances overcomes the excitation from the Lindblad resonances by a small margin of 4.6%. If one assumes that the gap is sufficiently clean that the co-orbital Lindblad resonances are inactive, then only a small degree of saturation in the corotation resonances (4.6%) is required to reverse the balance. In this case the net contribution of the first-order resonances will change from a damping to an excitation. Goldreich and Sari (2003) and Ogilvie and Lubow (2003) have evaluated the conditions under which a giant planet can experience eccentricity growth. The saturation of the corotation resonances is controlled by the ratio of the libration time to the viscous time. The smaller this ratio, the more saturated the resonance will be. If one denotes the width of the libration islands in a given corotation resonance by w, then the libration time scales as $1/w$ while the viscous time scales as w^2/ν. Their ratio therefore scales as νw^{-3}. Since we require saturation of the corotation resonances, we want this ratio to be small; this means that either the viscosity must be small or w must be large. For a disk of given viscosity, the upshot is that the initial eccentricity must be larger than some critical value to yield further eccentricity growth. This is a finite amplitude instability. Ogilvie and Lubow (2003) have examined the case of a Jupiter-mass planet in a disk with aspect ratio $h = 0.05$ and an $\alpha-$parameter of $4 \cdot 10^{-3}$. They find that for these parameters, a sufficient degree of saturation can be achieved in the first-order corotation resonances if the initial eccentricity is larger than $e_{\rm crit} \sim 0.01$.

This analysis, however, suffers from two shortcomings: the possibility of overlap between the libration islands of neighboring corotation resonances, and the fact that the corotation resonances share their location with the principal Lindblad resonances. Masset and Ogilvie (2004) have addressed these potential problems by means of numerical calculations, finding that the saturation properties of a given corotation resonance are essentially unchanged under both conditions.

This seems to suggest that giant planets orbiting in disks of sufficiently low viscosity should experience eccentricity growth if their initial eccentricity is not too small, although it is still unclear just how large their final eccentricity could be. It is probable that eccentricity growth should terminate when the planet begins to graze the edges of its gap, in which case it is unlikely that such a growth mechanism could account for the observed eccentricity distribution of extrasolar giant planets.

We also mention that to date no self-consistent numerical simulation has clearly validated this mechanism as a possible source of eccentricity growth, and in this spirit we recall the word of caution given in the last paragraph of section 4.1.4: saturating a narrow corotation resonance may be more difficult than is implied by the laminar disk models.

Finally, we emphasize that there is another aspect of the eccentricity driving problem: the secular exchange of eccentricity between the planet and the disk. We refer interested readers to the works of Ogilvie (2001), Papaloizou (2002) and Goldreich and Sari (2003) for a study of eccentricity dynamics in planet–disk systems. An estimate of this contribution to the eccentricity evolution can be made through what is called the apsidal resonance (Goldreich and Sari, 2003).

5.4 Migration of an eccentric low-mass planet

Thus far, we only have considered the contribution of first-order resonances to eccentricity growth and damping. As there is a net flux of energy from the planet to the disk at these resonances, they also have an impact on the evolution of the planet's semi-major axis; i.e., they have consequences on migration. Papaloizou and Larwood (2000) have performed a linear calculation of the disk torque for each azimuthal wavenumber m that takes into account as many resonances as necessary to reach convergence (they did not limit themselves to the first-order resonances). They find that the usual dominance of OLRs over ILRs at low eccentricities is reversed when $e > 1.1h$. This is due to the fact that the planet then

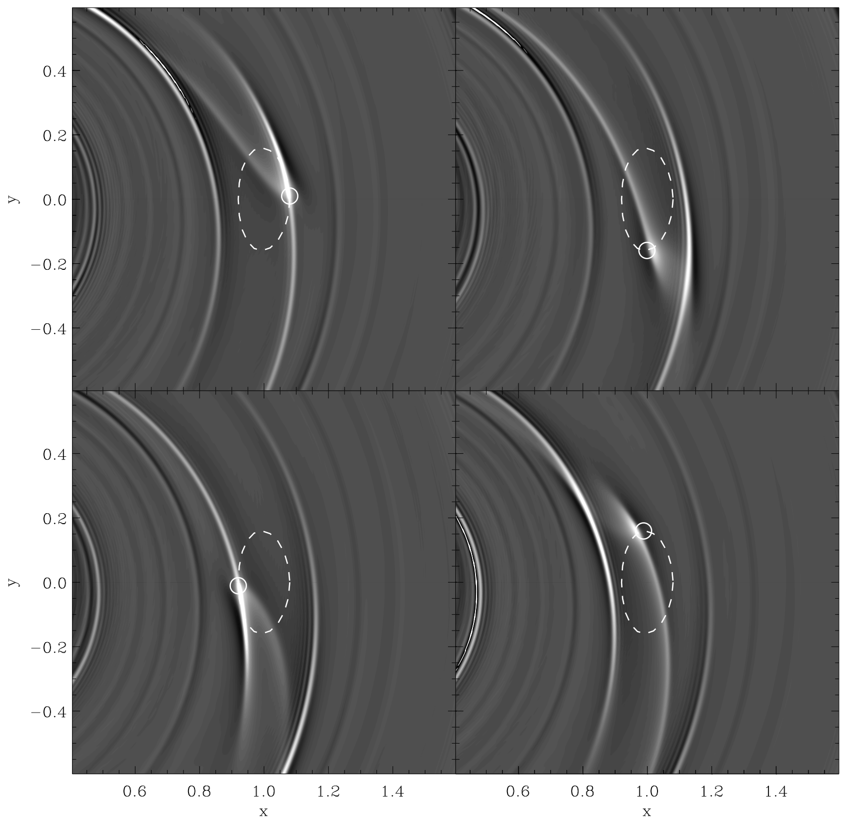

Fig. 24. This figure shows the surface density response to an embedded Earth-mass planet with eccentricity $e = 0.08$. The disk aspect ratio is $h = 0.05$. The dashed line shows the epicycle, which is described clockwise while the orbital motion is counter-clockwise. The solid circle indicates the instantaneous planet location. The sequence is to be read from left to right and from top to bottom. In the left-hand pictures, the planet is at an extremal distance from the central star. One can see that the planet excites an inner wake as it passes its apastron (upper left) and an outer wake as it passes its periastron (lower left).

crosses resonances which do not usually overlap the orbit at low eccentricities. The following considerations, found in Papaloizou and Larwood (2000) provide some insight into their result. When the planet is at the apocenter, it is slower than the ambient disk. Its instantaneous corotation radius lies further out in the disk, so the wake it excites is essentially an inner wake which exerts a positive torque. At the pericenter the planet excites what is essentially an outer wake, which exerts a negative torque. The natural imbalance of order $O(h)$ between inner and outer

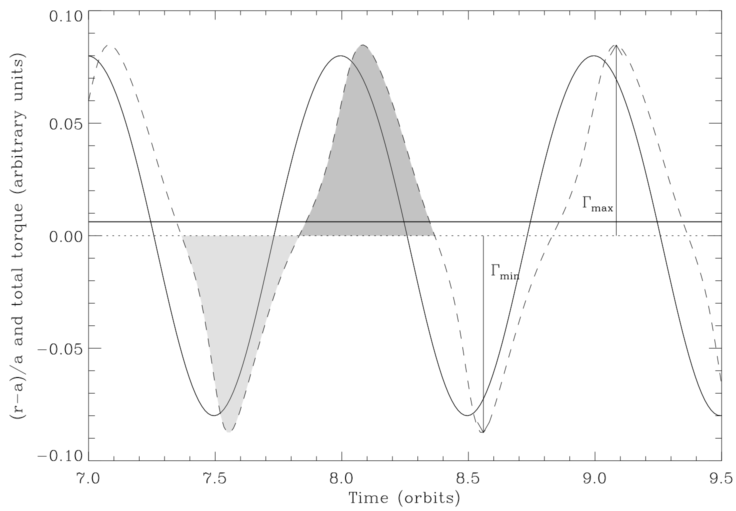

Fig. 25. This figure corresponds to Fig. 24, and shows the torque exerted by the disk on the planet as a function of time (dashed line). The solid line shows the planet's relative radial excursion $(r - a)/a$. As expected, the torque exerted on the planet is positive at the apocenter and negative at the pericenter. There is also a delay between the two curves, which corresponds to the time required to excite an inner or outer wake. A slight imbalance between the negative torque of the outer wake and the positive torque of the inner wake is apparent ($|\Gamma_{\min}| >\sim |\Gamma_{\max}|$), but it is also clear that the planet spends more time far from the central object. As a consequence, the positive contribution to the time-averaged torque (the dark gray shaded region) overcomes the negative contribution (light gray). The time-averaged torque, shown by the horizontal solid line, is therefore a positive quantity.

wakes can be compensated for by the effects of Kepler's second law: the planet spends more time at the apocenter, where it feels the (weaker) positive torque of the inner wake. If e/h is large enough, the planet should feel a positive average torque.[9] This principle is illustrated by the example presented in Figs. 24 and 25.

We note however that a positive torque does not imply that the planet migrates outwards. This would only be the case for a planet on a circular orbit. What dictates the migration rate is in any case the power of the tidal force, since the total energy of the planet exclusively depends on its semi-major axis (which is not the case of the angular momentum). The average power of the tidal force remains negative even for $e \sim h$ (the power of the tidal force involves a scalar product of the force with the planet velocity, which compensates for the effects of Kepler's

[9]The torque exerted by the disk on an eccentric planet is not constant in time as in the circular case, but rather is a time-varying quantity with period $2\pi/\kappa_p$.

second law). The excess of angular momentum transferred to the planet, instead of slowing down its inwards migration, is essentially used to circularize its orbit. One can work out the functional dependence of the circularization timescale in terms of the disk's parameters with the following simple argument : we imagine a situation in which the planetary eccentricity is $e = 1.1h$ and we assume for the sake of simplicity that it migrates at the same rate as if its orbit were circular. We want to know how far the planet migrates by the time it circularizes its orbit. As a simplifying assumption we assume that it conserves its angular momentum (this is an approximation only, since when e becomes lower than $1.1h$, the total torque exerted on the planet becomes negatives, hence it loses angular momentum; nevertheless this simplifying assumption gives us an order of magnitude of the distance δa swept by the planet's semi-major axis before circularization.) We can therefore recast our question in geometrical terms. The surface area of the planetary orbit is constant in time, and it is initially:

$$\mathcal{S} = \pi\sqrt{1-e^2}a^2, \tag{5.19}$$

while it can be expressed as follows, after circularization:

$$\mathcal{S} = \pi(a+\delta a)^2. \tag{5.20}$$

Substituting e by h in Eq. (5.19), neglecting the factor 1.1 since we only look for an order of magnitude, and using Eqs. (5.19) and (5.20) we are led to:

$$\delta a = -ah^2/4, \tag{5.21}$$

which indicates that the planet, independently of its mass, only migrates a small fraction $O(h)$ of the disk local thickness $H = ha$ before it is circularized. The eccentricity damping timescale τ_e can therefore be written as:

$$\tau_e = O\left(\frac{h^2}{4}\tau_{\mathrm{mig}}\right). \tag{5.22}$$

Using Eq. (4.6), we infer the functional dependence $\tau_e \propto h^4/(q\mu_D)$, in agreement with the expression given by Artymowicz (1993a) and by Papaloizou and Larwood (2000).

6 Numerical simulations

This section does not claim to offer a comprehensive overview of the numerical simulation techniques used to model planet–disk interactions, nor of the results obtained (essentially over the past decade) by numericists working in this field. We refer readers interested in this subject to the work of De Val-Borro et al. (2006) and references therein, which covers the gamut of numerical techniques applied thus far to the problem of planet–disk interactions. Rather, in section 6.1 we present a list of recent results that include some relevant physical ingredients not yet considered in this course. Owing to size considerations, these results are only briefly described. In section 6.2 we draw up a brief and partial list of the potential problems and shortcomings that numericists should bear in mind when performing their simulations of planet–disk interactions. Finally, we refer the reader interested in a fast advection algorithm applicable to disks in differential rotation to Masset (2000a) and Masset (2000b).

6.1 Recent results from numerical simulations

6.1.1 Self-gravitating disk calculations

Thus far, very little research has involved the disk's self-gravity in numerical simulations of planet–disk interactions. Boss (2005) has performed many disk simulations in which self-gravity is a key ingredient, but his work treats self-gravity as a trigger for giant planet formation by gravitational instability. His calculations are therefore short, running for only a few dynamical times, and involve only very massive objects. The planets formed in these simulations provoke a strongly non-linear disk response, and any migration effects are probably either marginal or negligible. A notable exception is the work of Nelson and Benz (2003a; 2003b), who have included self-gravity in their two-dimensional numerical calculations of the planet–disk interaction. Nelson and Benz (2003a) find that the migration of a planet that does not open a gap slows down by a factor of ~ 2 or more when the disk self-gravity is included. We will discuss this statement in more detail in section 6.2, in light of the recent analytical work by Pierens and Huré (2005).

6.1.2 Three-dimensional calculations

Until very recently three-dimensional calculations of the planet–disk interaction were a task limited to supercomputers, because of the high resolution and great many timesteps required. Even a single orbit requires quite a large number of timesteps to simulate properly (owing to the Courant, Friedrich and Levy –CFL– condition), and properly evaluating the torque of a migrating planet necessarily involves a large number of orbits.

High-resolution, three-dimensional simulations of planet–disk interactions have recently been performed (independently) by D'Angelo et al. (2003b) and Bate et al. (2003) over a wide range of planet masses. The goal of this research was mainly to compare the resulting torque estimates to the linear calculations of Tanaka et al. (2002). These two works obtained somewhat different results over the intermediate mass interval (see section 4.1.5), but essentially validated the work of Tanaka et al. (2002) in that they agree with the linear predictions for lower planet masses .

In the case of D'Angelo et al. (2003b), such high-resolution calculations were made possible by the use of a nested grid technique. These authors used a code derived from NIRVANA (Ziegler and Yorke, 1997). The nested grid technique consists of subdividing the zones in some region of the mesh (the patch) in order to achieve a higher resolution. Generally a zone will be split into eight sub-zones, doubling the resolution in radius, azimuth and colatitude. This refinement can be repeated recursively within a region that is already at a higher resolution. The resolution attained in the highest level of refinement is therefore 2^{l-1} times higher than that of the base mesh, where l is the total number of levels including the base mesh (D'Angelo et al., 2002; D'Angelo et al., 2003b). The nested grid technique is therefore very well suited to calculations of the disk's tidal interaction with one planet, when performed in the corotating frame. In this frame the planet is fixed with respect to the grid, a condition that while desirable is not necessary. See, for instance, D'Angelo et al. (2005).

Nested grid techniques often use timestep sub-cycling as well. Notwithstanding inhomogeneities in the velocity field and sound speed, the CFL condition becomes twice as demanding at each level of increased refinement. It is therefore a good idea to perform two timesteps on a fine level for every timestep on the previous (coarser) level. This scaling is repeated recursively until the highest refinement level is reached. As an example let us assume a base mesh with two levels of refinement, and denote the levels by A, B, and C. Under sub-cycling, the calculation of one full timestep on the base mesh (A) could imply either of the following calculation sequences: CCBCCBA or ABCCBCC, depending on the implementation.

Bate et al. (2003), who used the ZEUS code (Stone and Norman, 1992), achieved a high resolution by taking finer steps in radius and azimuth in the vicinity of the planet (i.e., near the planet's semi-major axis a and azimuth φ_p). This is not equivalent to the nested grid technique, where the resolution can be made higher in either radius or azimuth even far from the planet. Nevertheless, the resolution achieved by their simulation in the planet's vicinity is comparable to that allowed by a nested grid technique. It also comes at a much higher computational cost, since the technique of timestep sub-cycling used with nested grids cannot be applied. The fine resolution in the planet vicinity thus limits the speed of the calculation over the whole grid.

6.1.3 Simulations involving two giant planets

Thus far we have considered only the interaction of a single planet with the protoplanetary disk. Some extrasolar planetary systems, however, appear to have multiple planets, frequently in a low-order mean motion resonance. It is therefore also of interest to perform calculations involving several giant planets, in order to see (1) how the presence of another planet can affect migration, and (2) whether migration can lock two planets into mean motion resonance.

Kley (2000) has studied the evolution of two planets with initial masses of one Jupiter mass and initial semi-major axes in a 2 to 1 ratio. The planets are allowed to migrate in a fiducial disk with aspect ratio $h = 0.05$ and uniform kinematic viscosity, chosen such that $\alpha = 4 \times 10^{-3}$ at the orbit of the innermost planet. Both planets were allowed to accrete gas from the disk; i.e., material from the inner Roche lobe was attributed to the point-like planet mass at a rate limited by the nebula's capacity to supply material to the planets (Kley, 1999). The outer planet was found to migrate inwards, while the inner planet moved slightly outwards. In other words, the planets underwent convergent migration. At the end of the calculation, after 2500 orbits of the innermost planet, the outer planet had grown to a mass of about 3.2 M_{Jup} while the inner planet had reached a mass of about 2.3 M_{Jup}. This work shows that the migration of an inner giant planet can be halted by the presence of an outer giant planet. The two planets work together to create a large common gap. Under these conditions the inner planet has no outer wake in its immediate vicinity to drive its inwards migration. Since the planets are brought closer together, and since they both reach an important mass, the system could become unstable after the gas is dispersed. Kley (2000) invokes a criterion for stability based on comparing the orbital separation of the two planets to their mutual Hill radius (Gladman, 1993), and concludes that there are two possible long-term outcomes for such a system:

1. The system is unstable. The orbits can cross, and it is possible for a close encounter between the planets to eject one and leave the other in an eccentric orbit. Kley (2000) argues that this process may explain the high eccentricities observed in many extrasolar giant planets.

2. Disk removal occurs early enough for migration to cease before the distance between the planets becomes lower than the minimum value required for stability. The planetary system then remains stable. This outcome could account for the existence of systems such as the outer Solar System, with well-separated giant planets in low-eccentricity orbits.

Masset and Snellgrove (2001) have approached this problem by studying a different case: their outer planet was chosen to have a Saturn mass instead of a Jupiter mass, and the planets were not allowed to accrete material from the disk (on the grounds that planetary accretion rates are poorly constrained). They found the following unexpected behavior:

- Saturn migrated quickly in the early stages of the calculation (it turns out that this was a runaway migration, but this mode was unknown at the epoch of the work). As Jupiter started a much slower type II migration towards the central object, the orbits of the two objects converged quickly. Saturn reached a 2 : 1 mean motion resonance with Jupiter, but did not get trapped there owing to its large migration rate. It did not get trapped at the 5 : 3 mean motion resonance either, but eventually became locked into a 3 : 2 mean motion resonance.

- As long as the planets were locked in this close mean motion resonance, they migrated outwards together.

- The long-term outcome of this scenario, not mentioned in Masset and Snellgrove (2001), may be that Saturn experiences a number of outwards runaway migrations. These results are presented in Fig. 26.

Several effects conspire to sustain the outwards migration of this specific two-planet system, when it is locked into a 3 : 2 mean motion resonance:

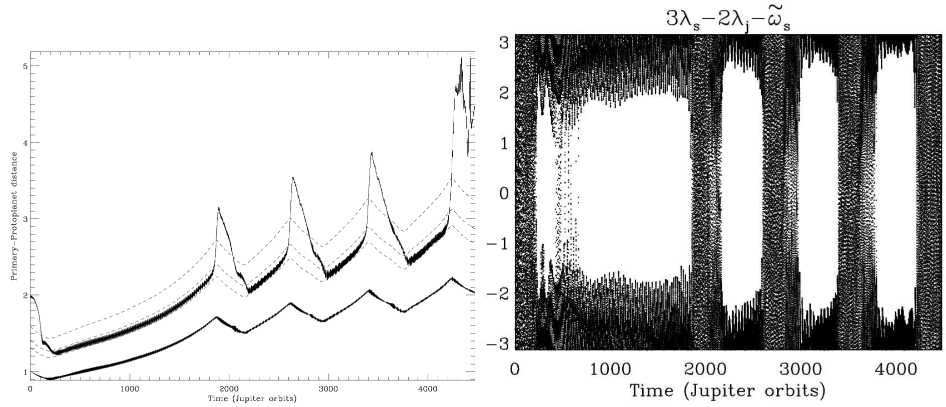

Fig. 26. Left: distance of the protoplanets from the central object as a function of time (in units of Jupiter's initial orbital period). An initial stage of rapid, convergent migration is apparent over the first ~ 200 orbits. The dashed curves represent, from top to bottom, the nominal positions of the 2:1, 5:3 and 3:2 mean motion resonances with Jupiter. Saturn gets locked into a 3:2 mean motion resonance with Jupiter, as can be seen in the right-hand plot from the libration of the resonance angle $\varphi_r = 3\lambda_s - 2\lambda_j - \tilde{\omega}_s$. λ_s (λ_j) in this expression is the mean longitude of Saturn (Jupiter), and $\tilde{\omega}_s$ is the longitude of Saturn's pericenter. Whenever this critical angle does not span the whole $[-\pi, +\pi]$ interval (i.e., the "white areas" on the right-hand plot), it will librate instead of circulating. This means that the planets are trapped in a 3:2 resonance. Note that the other critical angle (not shown here), $\varphi'_r = 3\lambda_s - 2\lambda_j - \tilde{\omega}_j$, librates at the same epochs as φ_r. The outward/inward migration episodes of Saturn around $t = 2000$, $t = 2800$, $t = 3600$, and $t = 4500$ are all runaways, which unlock Saturn from its mean motion resonance with Jupiter.

1. The planets possess a large, common gap, with weak tidal truncation on the outer side (Saturn's side). The gap is also shallower overall on its outer side.
2. The inner wake is launched by Jupiter, the more massive planet. It exerts a larger torque on Jupiter (and ultimately on the locked Jupiter-Saturn system) than the outer wake, which is launched by Saturn. We therefore have an unusual torque imbalance that favors outwards migration.
3. The positive wake torque triggers outwards migration, which can achieve a steady state owing to Saturn's weak tidal truncation. Material from the outer disk flows across the outer horseshoe separatrix of Saturn. This flow has two consequences:
   - It permanently replenishes the inner disk, thereby enabling Jupiter to continue exciting its inner wake.
   - Much in the same way that co-orbital dynamics yield a corotation torque that depends on the migration rate (section 4.3), the flow exerts

a positive torque on the two-planet system and assists the outwards migration. This last effect is however of minor relevance in the present case (Morbidelli and Crida, in prep.)

The conjunction of all these effects allows a sustained outwards migration of this two-planet system. This should be a generic behavior under the following conditions. (i) The outer planet, although giant, should be significantly lighter than the inner one; Masset and Snellgrove (2001) give an estimate of the maximal outer to inner mass ratio. (ii) The thermal gap clearance criterion should be only marginally satisfied by the outer planet, so that tidal truncation is weak at the outer edge of the common gap.

We make the following additional comments on the results of Masset and Snellgrove (2001):

- Planetary accretion can significantly modify these results, both quantitatively and qualitatively. In particular, it can divert a significant fraction of the gas flow across the common gap that should otherwise replenish the inner disk.

- Some attempts to reproduce these results with a similar setup have failed (Kley, priv. comm.), while others have succeeded (Crida, priv. comm.). Presumably, this is because the parameters adopted are only marginally favorable to outwards migration, and depending on the details of the numerical scheme (the torque evaluation, the numerical viscosity, the potential softening length, etc.), one may or may not get a migration reversal. This implies that the particular scenario described by Masset and Snellgrove (2001) should be investigated more thoroughly, as it is affected by details of the numerical scheme. However, it is still a generic behavior that has been observed in many different simulated systems.

- A close (such as the 3 : 2) mean motion resonance seems to be necessary for a light outer planet and a heavy inner planet to create a common gap. No mean motion resonance this close has ever been observed in extrasolar planetary systems, where the most common commensurable ratio is 2 : 1. Neither has the 3 : 2 resonance been observed in numerical simulations involving a more massive outer planet. Rather, planets tend to lock themselves into 2 : 1 or more distant resonances (Nelson and Papaloizou, 2002). It seems that a rapid migration (maybe type III) of the outer planet is necessary to overcome the 2 : 1 resonance and reach deeper mean motion resonances.

As stated above, the most common mean motion resonance observed in extrasolar giant planet systems is the 2 : 1 resonance. The best and most studied example of this resonance is GJ 876, which has motivated many modeling attempts (Snellgrove et al., 2001; Kley et al., 2004; Kley et al., 2005). An interesting challenge of this modeling is to account for the eccentricities observed in this system. It consists of a central star with spectral type M4 V and mass 0.32 $M_{\odot}$, and three planets with periods, $M_p \sin i$ and eccentricities that are respectively: 60.94 ± 0.013

days, $1.935 \pm 0.007\ M_J$ and $e = 0.0249 \pm 0.0026$ for Gliese 876b, 30.1 days, $0.56\ M_J$ and $e = 0.27$ for Gliese 876c and $1.93776 \pm 7 \cdot 10^{-5}$ days, $0.023 \pm 0.003\ M_J$ and $e = 0$ for Gliese 876d. The first two planets are in 2 : 1 orbital resonance. The third planet is lightweight, has a much tighter orbit than the other ones, and should have a negligible influence on their dynamics. It was only recently discovered and was unknown at the epoch of the aforementioned works. The properties of this system must result from a balance between resonant migration, which tends to increase the eccentricities, and the action of coorbital material, which tends to circularize the orbit. Snellgrove et al. (2001) find that for a system with an outer giant planet three times more massive than the inner planet, the inner planet eccentricity is given by $e_1 \sim (0.07 t_c / t_{\rm mig})^{1/2}$. In this expression, t_c is the circularization timescale and $t_{\rm mig}$ is the migration timescale. The smaller t_c is, the more circular the orbit will be. A faster migration (i.e., smaller $t_{\rm mig}$), on the other hand, leads to a more eccentric inner planet. Kley et al. (2004) have revisited this problem, finding that the eccentricity damping obtained from hydrodynamical simulations is not enough to account for GJ 876. Kley et al. (2005) later suggested that the system underwent a moderate resonant migration and simultaneous disk dissipation after capture; the final eccentricity of the inner planet would then be compatible with observations. We refer interested readers to the aforementioned publications for further details.

6.1.4 Simulations with realistic thermodynamics

Numerical simulations of planet–disk interactions customarily use an isothermal equation of state and a fixed, axisymmetric temperature profile (this amounts to fixing the aspect ratio profile). This approach assumes that the internal energy gained through shocks is radiated away with high efficiency. D'Angelo et al. (2003a) have investigated the tidal interaction of a giant planet with a disk described more realistically. They used a two-dimensional disk, and an energy equation that includes both viscous heating and radiative losses. The radiation term is valid in the optically thick and optically thin regimes, and is thus very well suited to thick protoplanetary disks which may become optically thin in a deep gap. Broadly speaking, the results of D'Angelo et al. (2003a) are in agreement with more restricted studies using a locally isothermal equation of state, in terms of both migration rate and accretion rate. By using the nested grid technique (section 6.1.2), they also obtain the properties of the circumplanetary disk: it was generally optically thick, had an aspect ratio of a few tenths, and had a temperature profile scaling as r^{-1} (r being the distance from the planet).

Papaloizou and Nelson (2005) have performed hybrid calculations aimed at describing the evolution of accreting gas giant planets. They used a 1D model to describe the gas surrounding the protoplanet, which can include either radiative or convective transfer. They then solve this model analytically, adopting outer boundary values provided by hydrodynamical, locally isothermal calculations.

Thus far, fully radiative 3D hydrodynamics have almost never been employed in modeling planet–disk interactions. Such a problem is extremely complex and costly in terms of computation time. This kind of calculation could allow one to test the predictions of Jang-Condell and Sasselov (2005), however, who argue that taking into account the temperature perturbations due to shadowing and irradiation of the disk photosphere could significantly reduce the type I migration rate.

Such calculations would also allow one to describe gap clearance in a flaring, irradiated disk (D'Alessio et al., 1998). One unanswered question on this topic is whether irradiation of the gap's outer edge (at high altitudes, since the equatorial region is shadowed by the inner disk) would cause it to puff up significantly. Since the tidal torque on a giant planet due to the inner and outer disks is very sensitive to the disk thickness, giant planets could have their type II migration rate significantly altered by this effect.

At the time of writing these proceedings, however, there have been two notable attempts to carry out fully radiative, hydrodynamic calculations related to the planet–disk problem. Klahr and Kley (2006) consider a Jupiter-mass planet, and study the temperature structure of the disk in the planet's vicinity. They find a significantly different flow structure in the Roche lobe than that predicted by isothermal calculations; a hot bubble appears around the planet rather than a thin, Keplerian, circumplanetary disk.

Another remarkable calculation is the recent radiative hydrodynamics calculation of Paardekooper and Mellema (2006), who consider a low-mass planet embedded in a disk with inefficient radiative cooling. A complex temperature structure develops in the vicinity of the planet over the shear timescale A^{-1}, which seems to yield an underdense region behind the planet. As a consequence, the disk ultimately exerts a positive torque on the planet. A follow-up of these calculations is needed, but this result clearly indicates that radiative transfer effects may prove crucial in resolving the problem of type I drift, which is still far too rapid.

We also note the work of Morohoshi and Tanaka (2003), who consider the case of a low-mass object embedded in an optically thin disk (they argue that grain growth should be sufficient to lower the optical depth by the epoch of planet formation). They find that the temperature downstream of the wake is lower than the unperturbed temperature. This substantial change of the temperature structure in the vicinity of the planet can alter the one-sided torque by ~ 40 % for a 3 $M_\oplus$ planet. This result suggests that the impact of radiation on the differential Lindblad torque may be large.

6.1.5 Three-dimensional MHD calculations

Three-dimensional magneto-hydrodynamic calculations are probably the most computationally expensive calculations ever performed on the topic of planet–disk interactions. We refer the reader to section 4.4 for a discussion of the results of these calculations.

6.1.6 Global disk evolution

One important drawback of 2D and 3D grid calculations is that they necessarily cover a narrow radial range. In particular, they cannot extend very far towards the central object as the timestep becomes severely limited by the CFL condition. This limitation may create some important artifacts in the gap clearance calculations. The inner disk (that is to say, the region between the mesh inner boundary and the gap inner edge) is usually narrower than it should be, and its disappearance through the inner boundary may be strongly altered by the proximity of this boundary. Crida et al. (2006b) have designed a hybrid technique to deal with this problem: the polar 2D grid is extended inwards and outwards by means of a 1D grid at virtually no additional cost. Some care has to be taken that mass and angular momentum are exchanged correctly between the 2D grid and the 1D grid. This requires monitoring the mass flux across the 2D grid boundaries. The mass flux is associated with an angular momentum flux, which can be evaluated using the average angular velocity at the 2D/1D interface. The angular momentum thus gained (lost) by the 1D grid is generally not equal to the angular momentum lost (gained) by the 2D grid at the interface. The difference is transported by non-axisymmetric disturbances (waves), which cannot be described on a 1D grid. Crida et al. (2006b) provide a simple and efficient prescription to handle the angular momentum flux carried by these waves when they reach the 2D/1D interface. Preliminary calculations have shown that these hybrid calculations give essentially the same results as the much more expensive, fully 2D calculations. As mentioned above, this technique can better describe the evolution of the inner disk in type II migration. It can also test the suggestion of Ward (2003) that some planets may resist inwards type II migration in viscous, truncated disks when the outer regions spread viscously outwards. Although in this kind of hybrid scheme the inner radius of the 1D grid can be made as short as the star radius or the star corotation radius, no realistic description of the disk–star interaction is possible. Nevertheless, it does allow a more realistic description of the disk viscous evolution over a wide range of radii, within which the detailed physics of the star–disk connection should be unimportant.

6.2 Potential problems of numerical schemes

We give in this section a partial list of problems that the numericists who simulate planet–disk tidal interactions should bear in mind. First, we list those issues related to specific numerical schemes. Second, we describe a few conceptual problems that are independent of the scheme adopted and mention possible workarounds. Broadly speaking, the numerical schemes can be divided into three families: staggered mesh schemes, Godunov schemes (another variety of mesh scheme), and Lagrangian schemes. As far as planet–disk interactions are concerned, the latter category reduces to Smoothed Particle Hydrodynamics (SPH).

6.2.1 Godunov schemes

Godunov schemes are based on the use of a Riemann solver to predict the fluxes of conserved quantities at interfaces between adjacent zones. They have a number of desirable properties: they properly handle shocks, which fulfill the Rankine-Hugoniot relationships, and they do not need artificial viscosity to stabilize the shocks, which can be spread over one or two zones. As a consequence, for the same number of zones they have an effective resolution slightly better than staggered mesh schemes, which are more diffusive. Furthermore, all the quantities in non-magnetized hydrodynamical simulations are zone-centered, which makes mesh management a simpler task than it is for a staggered mesh scheme.

These schemes have two important problems, however, in the context of planet–disk calculations. Stationary shocks that are nearly aligned with the grid will suffer from a numerical instability of an "odd–even" nature, named the carbuncle instability. This instability makes the tidal wake of a giant planet in a low viscosity disk, when described in the corotating frame, flap like a flag in the wind. This behavior seems to be inevitable in Godunov schemes when the resolution is high and the dissipation is low, but it does not appear in high-resolution simulations with staggered mesh codes. This behavior is still poorly understood. There exist some solvers, however, that are specifically designed to avoid this instability (Pandolfi and D'Ambrosio, 2001).

Another important drawback of Godunov schemes is their generic inability to handle steady states with a source term. As a consequence they are unable to properly describe a Keplerian disk in vertical hydrostatic equilibrium, which may have rather undesirable consequences when modeling its tidal interaction with a protoplanet. We give the simplest possible illustration of this problem: the case of an isothermal, one-dimensional atmosphere with uniform gravity. The analytic solution is a density profile that follows the law $\rho = \rho_0 \exp(-z/H)$, where ρ_0 is the density at ground level, z is the altitude, and $H = c_s^2/g$ is the atmosphere height scale (g being the magnitude of the gravitational field). We can try to describe this atmosphere by means of the simplest possible Godunov scheme, in which the zone-centered values at the beginning of a timestep are used to define the Riemann problems at the interfaces. This scheme thus does not require a slope evaluation or a predictor step. We assume that the scheme does describe the equilibrium profile on a uniformly spaced grid; i.e., the profile consists of a sequence of densities $(\rho_i)_{i\geq 0}$ in a geometric sequence ($\rho_{i+1} = \eta\rho_i$ for any i, where η is a constant that depends on c_s^2, g, and the mesh step δz). The equilibrium profile also includes a sequence of null vertical velocities: $u_i = 0$ for any i. The isothermal Riemann problem at the interface between zone i and zone $i+1$ is therefore defined by the conditions $\rho_L = \rho_i$, $u_L = 0$, $\rho_R = \rho_{i+1}$, and $u_R = 0$. This admits a solution with $u_* > 0$ (since $\rho_L > \rho_R$) and ρ_* such that $\rho_R < \rho_* < \rho_L$. The next Riemann problem is defined by $\rho_L = \eta\rho_i$, $u_L = 0$, $\rho_R = \eta\rho_{i+1}$, and $u_R = 0$, and the solution gives $\eta\rho_*$ for the density and the same velocity u_* that was found in the previous zone. (The isothermal Euler equations are invariant under a uniform scaling of the density by a factor η.) Continuing the pattern, we see that there is a net mass flux into zone i since $\rho_* u_* - \eta\rho_* u_* \neq 0$. Similarly, there is a net momentum flux into this zone which can be compensated for, either approximately or exactly, by an adequate source step. The mass flux, however, cannot be compensated for as there is no source term in the continuity equation. Hydrostatic equilibrium therefore cannot be sustained by this scheme.

Workarounds to this generic problem may consist of embedding the source term (here gravity) in the Riemann solver or using modified states (Zingale et al., 2002). The latter are generally adapted to a given form of the source term. (In the study just cited this is again a uniform gravity field , with the possibility of generalizing to a non-uniform gravity field.) LeVeque (1998) has designed a method that allows a numerically exact description of steady states and their perturbations. It consists of splitting each zone into two regions, in the manner of a river lock. The two parts of the zone define a locally steady state, and the Riemann problem at the interfaces corresponds to the perturbation of this locally steady state. This scheme will work with any source term. It can also be adapted to the case of a Keplerian disk, in which case one enforces both vertical hydrostatic equilibrium and centrifugal balance (Masset, in prep.). Note, however, that such workarounds have a non-negligible computational cost.

Only a few works to date have published results based on a Godunov method. Bryden et al. (1999) as well as Nelson and Benz (2003a; 2003b) have both used PPM codes (a widespread high-order Godunov method) to simulate the tidal interaction of planets with protoplanetary disks. Ciecieląg et al. (2000) have used a two-dimensional Godunov scheme with Adaptive Mesh Refinement (AMR) to study the flow in the vicinity of a giant planet. More recently, Paardekooper and Mellema (2006) have used the RODEO code to perform three-dimensional radiative transfer hydrodynamic calculations for a low-mass object in a protoplanetary disk. A comprehensive list of codes that have been used in the planet–disk interaction problem can be found in de Val-Borro et al. (2006).

6.2.2 Staggered mesh schemes

The best known example of a staggered mesh scheme is the ZEUS code (Stone and Norman, 1992), but a plethora of such schemes have been used in simulations of planet–disk interactions (de Val-Borro et al., 2006). In a staggered mesh scheme, velocities are defined at the center of and perpendicular to the interfaces. Ideally, this is meant to respect the centering of spatial derivatives in the continuity equation and the Euler equation. The main problem is that these codes are not specifically designed to handle shocks, so their treatment is awkward. An artificial viscosity must be introduced to avoid post-shock oscillations that might otherwise render the scheme unstable. These schemes are thus more diffusive than schemes based on Godunov's method.

On the other hand, staggered mesh schemes do not suffer from the carbuncle instability, their implementation is simple, they are faster than Godunov schemes, and they can properly handle steady states with source terms without extra work or computational cost. These advantages explain their wide popularity, and such simulations have considerably improved our knowledge of planet–disk interactions over the past decade.

6.2.3 SPH methods

At first glance, SPH methods do not seem well suited to the description of planet–disk interactions. They are rather diffusive and do not perform as well as grid methods, especially in accounting for sharp features such as steep tidal truncation at the gap edges. They have low resolution by construction in low-density regions such as the interior of a gap. They also yield weaker planetary wakes than grid-based methods do (de Val-Borro et al., 2006), and they are rather slow. However, they enable fully three-dimensional calculations without introducing additional complexity and do not suffer from the boundary condition problems of grid-based codes. And finally yet foremost, their tree-based structure can implement self-gravity in a straightforward manner. Finally, SPH codes also conserve linear momentum, which is an impossible requirement for polar or spherical grid methods; this may be of importance in problems such as eccentric disks where it is crucial to fix the center of mass of the whole system {disk+star+planet}. Self-gravitating SPH schemes may also help find a better workaround to certain inconsistencies exposed in sections 6.2.5 and 6.2.6 which arise in planet–disk simulations without self-gravitating disks. Finally, there exist some SPH schemes specifically designed to describe planetary migration and accretion (Schäfer et al., 2004).

6.2.4 Issues arising in disks without self-gravity

Numerical algorithms commonly simplify the planet–disk interaction by discarding the disk's self-gravity. More precisely, while the planet feels the disk's gravitational force (which is why the planet migrates) and the disk feels the planet's gravitational force (which is why a wake is excited in the disk), a given fluid element of the disk does not feel any force from the other fluid elements of the disk. The usual justification for this simplification, apart from the considerable savings in computation time, is the fact that protoplanetary disks have a large Toomre's Q parameter. Even though the disks are not threatened by gravitational instability, we shall see that neglecting the disk's self-gravity may still have important consequences for planetary migration.

6.2.5 Spurious resonance shift and type I migrating planets

As presented in section 4.1, type I migration results from a relatively small imbalance between the torques at Outer Lindblad Resonances and the torques at Inner Lindblad Resonances. We have seen in section 4.1.2 that the migration is very sensitive to a slight shift in the resonances, such as that provided by the pressure buffer. (Recall that this effect was able to counteract large variations in the surface density slope.) First we note that if the resonances are shifted inwards, then the torques at the OLR are strengthened while the torques at the ILR are weakened.

The migration thus speeds up. Conversely, if the resonances are shifted outwards then migration slows down. Second, we note that if a planet only feels the gravity of the central object (and therefore has a Keplerian orbit) it will be slightly slower than if it feels the gravity of both the central object and the disk. The same thing is true for the disk: a self-gravitating disk rotates slightly faster than the same disk without self-gravity (except in the vicinity of its inner edge).

We stress that in this section we consider the linear case, which is relevant for low-mass, deeply embedded objects. The planet's mass is considered to be infinitesimally small, while the masses of the central star and disk are treated as finite quantities (the latter being much smaller than the former). Our discussion *exclusively* focuses on the locations of the resonances and their impact on the tidal torque, whether or not the disk gravity is taken into account.

Let us now consider the following numerical experiment: a low-mass planet is held on a fixed circular orbit in a disk without self-gravity, and we measure the torque acting on this planet. This corresponds to case A of Fig. 27. This set up could be intended to check the analytical predictions of Tanaka et al. (2002) or Ward (1997), as in these analytical works and many others the disk's self-gravity is also discarded. In this experiment, the planet is placed on a circular orbit with exactly the Keplerian frequency, while any non-Keplerianity of the disk is exclusively accounted for by the radial pressure gradient. One can check in this case that the planetary torque scales with the disk surface density, and that the derived torque agrees with analytical predictions.

We can now perform a second experiment, in which we allow the planet to freely migrate under the action of the disk. In other words, we release the planet and let it "feel" the potential of the disk. This corresponds to case B of Fig. 27. We can make two observations:

1. The migration rate measured for this planet is faster than what the torque evaluation on a fixed circular orbit would predict.

2. The migration rate does not scale with the surface density of the disk. The dependence is steeper than a linear relation, and one only recovers the results of fixed circular orbit calculations as the disk mass tends to zero (Tanigawa and Lin, 2005).

These two (perhaps unexpected) observations can be understood as follows: because the planet now feels the disk gravity, its orbital frequency increases slightly. The disk, on the other hand, retains its former rotation profile in the absence of self-gravity. As a consequence, all resonances shift inwards (as can be seen in case B of Fig. 27) and migration speeds up. This increase in the drift rate is an *artifact*, which arises from the fact that the planet and the disk do not orbit in the same potential. This also explains why the drift rate scales with disk mass more steeply than a linear relationship: although the torque scales with the surface density, the resonance shift also increases as the disk mass increases. If at this stage one introduces the disk's self-gravity, then the disk will tend to rotate slightly faster while the planet retains its angular velocity. The resonances thus

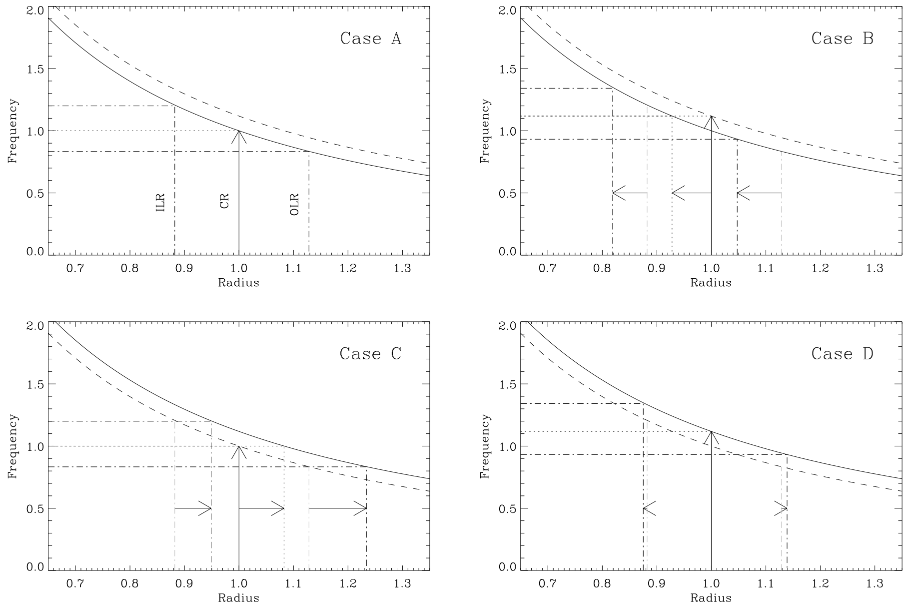

Fig. 27. Resonance locations in the four different cases described in the text. The lower curve in each plot represents a strict Keplerian rotation profile, while the upper curve represents the rotation profile in the potential of the central object and the disk. The disk mass has been exaggerated to improve legibility. The vertical arrow at $r = 1$ indicates the planet's orbital frequency. In the left column this arrow reaches the lower curve, so the planet has a Keplerian frequency in cases A and C. The solid curve indicates the disk's orbital frequency. In the upper row the solid curve is lower, so in these cases (A and B) the disk has a strict Keplerian frequency and feels only the potential of the central object. In the lower row the disk also feels its own potential; i. e., cases C and D correspond to a self-gravitating disk. The location of the corotation resonance is indicated by a dotted line in each case, and corresponds to the intersection of the solid curve with the horizontal line going through the arrow's head; i.e., where the disk's frequency matches the planet's orbital frequency. This resonance coincides with the orbit in cases A and D because the planet and the disk orbit in the same potential (note that for the sake of simplicity, the pressure buffer has been discarded since its effect is the same in all cases). The dash-dotted lines indicate the locations of two arbitrarily chosen Lindblad resonances (the OLR for $m = 4$ and the ILR for $m = 5$). Their original locations (those of case A) are indicated by light gray lines on each diagram. This makes the resonance shift, as indicated by horizontal arrows, more evident.

shift back towards larger radii, and migration slows down. This corresponds to the transition from case B to case D in Fig. 27. The result that the disk's self-gravity slows down the planet drift is in agreement with the findings of Nelson and Benz

(2003a), as well as the statement by Pierens and Huré (2005).

As such, this statement can be confusing, however, in the sense that it compares a self-consistent situation (case D, with self-gravity) to a strongly biased situation. The latter includes an *artificial* shift in the resonances, because the planet "feels" a disk that does not "feel" itself (case B). The resonance shift introduced by releasing the planet and the resonance shift introduced by enabling the disk's self-gravity *almost* cancel each other out. It is much more interesting to compare the final migration rate in a self-gravitating disk to the initial migration rate of a planet held on a fixed circular orbit when both the planet *and* the disk feel only the gravity of the central object. This initial configuration corresponds to the situation contemplated in analytical estimates of migration rates. There is another effect which hitherto has not been contemplated in this analysis, namely the fact that density waves propagate slightly to the inside of their Lindblad resonances in a self-gravitating disk. Pierens and Huré (2005) claim that this effect dominates the resonance shift induced by the introduction of the disk's potential, and argue that the net effect is a slight increase in the drift rate.

To sum up the above results, one can say that applying the disk's gravity to both its own rotation profile and the rotation of the planet yields a slight increase of the migration rate with respect to analytical predictions that consider both planet and disk to orbit in a strictly Keplerian potential. This effect relies on a minute shift of the resonances, and requires a rather substantial disk mass to be noticeable (Pierens and Huré, 2005).

However, if one considers a numerical simulation with a freely migrating planet embedded in a disk without self-gravity (like most of the simulations performed so far), then there is an artificial shift of the resonances that speeds up migration (case B). This shift is much more important than that found in the self-consistent situation, due to a mismatch in the orbital frequencies of the planet and disk. This artifact may lead to overestimates of the drift rate by as much as a factor of two, in the MMSN at $r = 10$ AU.

It is clear that some workaround must be found for the above situation (a planet freely migrating in a disk without self-gravity). We suggest two possible solutions:

- The azimuthal average of the disk surface density could be subtracted from the surface density of a zone before evaluating the force exerted by the disk on the planet. In this case, only non-axisymmetric perturbations in the disk will exert a force on the planet. Notwithstanding these perturbations, the planet will still essentially orbit in a Keplerian potential and its angular speed will remain strictly Keplerian.

- Instead of considering a truly self-gravitating disk, which can be computationally expensive, one can include only the axisymmetric component of the disk's potential. This is feasible because only the resonance shift is important, and this shift is a consequence of changes in the 1D radial profile of orbital velocity. This solution suffices to shift the resonances exactly as if the disk were self-gravitating, and can be implemented at virtually no computational cost (Baruteau and Masset, in prep.).

6.2.6 Inertia issues in disks without self-gravity

Disks without self-gravity raise another issue, this time for high-mass planets possessing a circumplanetary disk. We consider the situation depicted in Fig. 28. We split the gas into two regions: a System of Interest (SOI), and the remainder of the disk. We limit our discussion to the case where the SOI can be treated as closed; i.e., it should not exchange material with the remainder of the disk. As the planet is surrounded by a circumplanetary disk, one should be able to isolate a small region in which the streamlines are closed. If such a region does not exist, the angular momentum budget of the SOI must include the angular momentum flux advected across its boundary. It is nevertheless useful to bear in mind the results to be obtained by assuming that the SOI is strictly closed. In this case we use the term "Circumplanetary Disk" (CPD) to refer to the gas enclosed by the SOI.

The wake imparts a specific torque $\gamma_{\rm wake}(\vec{r})$ everywhere in the SOI. For our purposes we assume that the SOI is sufficiently small that the mass-weighted average of $\gamma_{\rm wake}(\vec{r})$ can be considered equal to $\gamma_{\rm wake}(\vec{r}_p)$, $\vec{r}_p$ being the planet location:

$$\int_{\rm CPD} \rho\gamma_{\rm wake}(\vec{r})d^3\vec{r} = M_{\rm CPD}\gamma_{\rm wake}(\vec{r}_p), \qquad (6.1)$$

where M_{CPD} is the mass of the circumplanetary disk. We now assume further that we have a perfectly conservative scheme, so that the rate of change of angular momentum in a closed system is equal to the total torque applied to its parts. The equation that governs the semi-major axis evolution of the SOI (assuming that its "semi-major" axis is a well defined quantity, corresponding to the semi-major axis of the planet on which the SOI is centered) reads as follows:

$$2Ba(M_p + M_{CPD})\dot{a} = \Gamma_{\overline{SOI}\to p} + \Gamma_{CPD\to p} + \Gamma_{\overline{SOI}\to CPD} + \Gamma_{p\to CPD}, \qquad (6.2)$$

where $\Gamma_{A\to B}$ is the torque exerted by system A on system B, and $\overline{SOI}$ is the region complementary to the SOI, that is to say the remainder of the protoplanetary disk. The first two terms on the R.H.S. of Eq. (6.2) respectively correspond to the torques exerted on the planet (i.e., the first part of the SOI) by the remainder of the disk and the circumplanetary disk. The last two terms of the R.H.S. correspond respectively to the torque exerted on the circumplanetary disk (the second part of the SOI), by the remainder of the disk and the planet. The presence of the second and fourth terms on the R.H.S. may seem surprising, as these torques are internal to the system and should cancel out according to Newton's third law. One would therefore expect that $\Gamma_{CPD\to p} + \Gamma_{p\to CPD} = 0$. Nevertheless, we have already seen that considering a disk without self-gravity may lead to some inconsistencies. In this case one workaround for these inconsistencies is to renounce reciprocity of action. Eq. (6.2) is therefore correct even in such cases because the only assumption upon which it relies is that the scheme is conservative, which is always true.

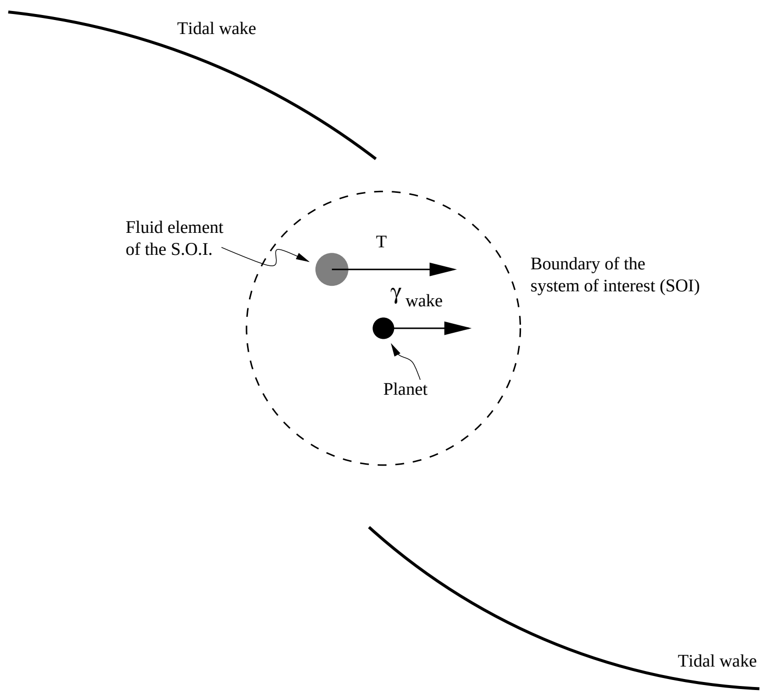

Fig. 28. The System of Interest (SOI), which is the region enclosed by the dashed circle, includes the planet. The gray spot represents an SOI fluid element of mass δm. If the disk is self-gravitating, this fluid element is subject to a torque T from the wake equal to $\delta m\gamma_{\rm wake}$. If the disk is not self-gravitating, this fluid element will not be subject to any torque from the wake.

Now assume that we want to enforce the reciprocity of action, that is to say we force the torque of the disk on the planet to be opposite to the torque of the planet on the disk. Implementing this rule implies that the torque exerted by the disk on the planet must be obtained by taking all the gas into account, including that enclosed within the SOI. Only in this case will the second and fourth terms on the R.H.S. of Eq. (6.2) cancel out, allowing Eq. (6.2) to be recast as:

$$2Ba(M_p + M_{CPD})\dot{a} = M_p\gamma_{\rm wake} + \Gamma_{\overline{SOI}\rightarrow CPD}. \tag{6.3}$$

For the sake of brevity we denote $\gamma_{\rm wake}(\vec{r}_p)$ by $\gamma_{\rm wake}$. If the disk is self-gravitating, then using Eq. (6.1) we have $\Gamma_{\overline{SOI}\rightarrow CPD} = M_{CPD}\gamma_{\rm wake}$, which yields

$$\dot{a}_{SG} = \frac{\gamma_{\rm wake}}{2Ba}. \tag{6.4}$$

This is not surprising, as the whole SOI feels the specific torque $\gamma_{\rm wake}$. On the other hand, if the disk is not self-gravitating then $\Gamma_{\overline{SOI}\rightarrow CPD} = 0$ and using

Eq. (6.2) we obtain:

$$2Ba(M_p + M_{CPD})\dot{a}_{NSG} = M_p\gamma_{\rm wake}. \tag{6.5}$$

We can thus arrive at the expression

$$\dot{a}_{NSG} = \left(\frac{M_p}{M_p + M_{CPD}}\right)\frac{\gamma_{\rm wake}}{2Ba} = \left(\frac{M_p}{M_p + M_{CPD}}\right)\dot{a}_{SG}. \tag{6.6}$$

Migration is slowed down in a disk without self-gravity by the inertia of the circumplanetary disk. This is logical enough; the circumplanetary disk ultimately has to lose angular momentum at the same rate as the planet, but it does not participate directly in exerting a torque on the disk. It contributes to the inertia of the migrating system, but only a subset of this system (the planet) contributes to the torque. The inconsistency introduced in the scheme by ignoring disk self-gravity affects the migration rate in a non-trivial manner, that depends on the way the flow is organized in the vicinity of the planet. If one seeks a workaround for this issue, it will require some prior knowledge of the flow. This issue should be relatively benign when the mass of the circumplanetary disk is small compared to the planet mass. This will be the case at low resolutions or when the disk is lightweight, but otherwise this issue can lead to an important (and artificial) reduction of the migration rate.

We now seek possible workarounds for this issue. In principle we can reconcile the migration rate with a self-gravitating scenario in one of two ways: either we "transform" the mass term on the R.H.S. of Eq. (6.5) into $M_p + M_{CPD}$, or we "transform" the mass term on the L.H.S of Eq. (6.5) into M_p.

- The first case can be easily realized if one "manually" applies the specific torque $\gamma_{\rm wake}$ to the whole circumplanetary disk. This is equivalent to adding an extra term $+\gamma_{\rm wake}M_{CPD}$ to the R.H.S. of Eq. (6.2). This is simply an attempt to re-establish the wake specific torque on the whole migrating system, as depicted in Fig. 28. Preliminary calculations seem to indicate that this approach works fine, in the sense that the migration rate converges to a finite value as one increases the resolution (Pepliński and Artymowicz, in prep.).

- The second case can be realized as follows. We first note that in the case of a disk without self-gravity the only torque exerted on the circumplanetary disk is $\Gamma_{p\to CPD}$. This term is also $2BaM_{CPD}\dot{a}$, since the circumplanetary disk also migrates at the rate $\dot{a}$. Eq. (6.2) can therefore be recast as

  $$2BaM_p\dot{a} = M_p\gamma_{\rm wake} + \Gamma_{CPD\to p}. \tag{6.7}$$

  We see that we recover $\dot{a} = \dot{a}_{SG} = \gamma_{\rm wake}/(2Ba)$ if and only if $\Gamma_{CPD\to p} = 0$. The second workaround is therefore to ensure that the circumplanetary disk does not exert a torque on the planet (whereas the planet's potential is felt by the whole disk). To implement this approach, the torque summation must discard the contribution of the circumplanetary disk. Discarding the SOI alleviates the planet's burden in migrating the mass of the circumplanetary disk. This mass becomes virtually null, and migrates at no cost; the circumplanetary disk essentially becomes a passive spectator of the planet migration.

We make the following comments on this analysis:

- The second workaround has been used by many authors, while to the best of our knowledge the first has not yet been used in any published simulation.
- As stated earlier, these workarounds require a prior knowledge of the flow around the planet so that the SOI can be properly defined. This is a lingering issue. The fraction of the Roche lobe that should be excluded from the torque calculation is still a matter of debate.
- The above analysis assumes that the SOI is strictly closed. The consequences of a flow across the circumplanetary disk boundary on migration are unknown.
- The above analysis assumes that the wake is strictly the same in cases with and without self-gravity, so as to isolate the effects of the circumplanetary disk's inertia. Actually, in the self-gravitating case the mass of the circumplanetary disk also contributes to the excitation of the wake. This only exacerbates the discrepancy between the two cases.
- We have assumed that the mass-weighted average of the wake's specific torque over the system of interest is equal to the specific torque at the planet location. Even if this is not the case, however, both workarounds will enforce a drift rate dictated by the specific torque at the planet location. It is therefore of interest to investigate the extent to which this assumption is reasonable, possibly by means of numerical simulations.
- All the above analysis showing the importance of the disk's self-gravity is valid regardless of Toomre's Q parameter, for both the protoplanetary disk and the circumplanetary disk. No claims whatsoever have been made about the disk temperature or sound speed.
- Discarding the circumplanetary disk torque on the planet is fine as far as re-establishing the balance between gravitation and inertia goes, but it may hide other effects. D'Angelo et al. (2005) have performed an analysis of the torques exerted by the inner Roche lobe on a giant planet at high resolution, in a disk without self-gravity. They considered the particular case of a Saturn-sized planet surrounded by a very heavy disk, and found that as the mesh resolution increases, the mass of the circumplanetary material increases and the migration rate drops. These findings are compatible with the above analysis. However, they also consider the case of a Jupiter-sized planet surrounded by a much lighter disk. In this case they find that the

inner Roche lobe may exert a significant torque on the planet even if the planet does not migrate. Clearly these results cannot be understood in the framework of the above analysis. The origin of this torque is still unknown. In a steady state, the angular momentum given to the planet by the inner Roche lobe (if the latter is closed) has to be compensated by some torque imparted by the remainder of the system. This torque could come from the remainder of the gas or from the central object. The tide raised by the central object seems to be far too small to account for the torque exerted by the inner Roche lobe on the planet (Baruteau, priv. comm.; D'Angelo, priv. comm.), but one can also contemplate the torques exerted by the remainder of the gas on the inner Roche lobe: pressure torque, viscous torque, and the torque arising from the artificial viscosity. If none of these torques can account for the torque exerted by the inner Roche lobe on the planet, we will have to reconsider the conservation properties and reciprocity of action of the numerical scheme on small scales.

7 Acknowledgments

I thank Gennaro D'Angelo and Clément Baruteau for their very thorough reading of a first draft of this work, which significantly improved its content. I also thank Gennaro D'Angelo for providing me with Fig. 9b.

References

Artymowicz, P.: 1993a, *ApJ* **419**, 166
Artymowicz, P.: 1993b, *ApJ* **419**, 155
Balbus, S. A. and Hawley, J. F.: 1991, *ApJ* **376**, 214
Balmforth, N. J. and Korycansky, D. G.: 2001, *MNRAS* **326**, 833
Bate, M. R., Lubow, S. H., Ogilvie, G. I., and Miller, K. A.: 2003, *MNRAS* **341**, 213
Boss, A. P.: 2005, *ApJ* **629**, 535
Bryden, G., Chen, X., Lin, D. N. C., Nelson, R. P., and Papaloizou, J. C. B.: 1999, *ApJ* **514**, 344
Ciecieląg, P., Plewa, T., and Różyczka, M.: 2000, *Astronomische Nachrichten* **321**, 171
Crida, A., Morbidelli, A., and Masset, F.: 2006a, *Icarus* **181**, 587
Crida, A., Morbidelli, A., and Masset, F.: 2006b, *ArXiv Astrophysics e-prints, Accepted for publication in A&A*
D'Alessio, P., Canto, J., Calvet, N., and Lizano, S.: 1998, *ApJ* **500**, 411
D'Angelo, G., Bate, M. R., and Lubow, S. H.: 2005, *MNRAS* **358**, 316
D'Angelo, G., Henning, T., and Kley, W.: 2002, *A&A* **385**, 647
D'Angelo, G., Henning, T., and Kley, W.: 2003a, *ApJ* **599**, 548
D'Angelo, G., Kley, W., and Henning, T.: 2003b, *ApJ* **586**, 540
de Val-Borro, M., Edgar, R. G., Artymowicz, P., Ciecielag, P., Cresswell, P., D'Angelo, G., Delgado-Donate, E. J., Dirksen, G., Fromang, S., Gawryszczak,

A., Klahr, H., Kley, W., Lyra, W., Masset, F., Mellema, G., Nelson, R. P., Paardekooper, S.-J., Peplinski, A., Pierens, A., Plewa, T., Rice, K., Schäfer, C., and Speith, R.: 2006, *MNRAS* pp 695–+

Dubrulle, B., Marié, L., Normand, C., Richard, D., Hersant, F., and Zahn, J.-P.: 2005, *A&A* **429**, 1

Ford, E. B., Havlickova, M., and Rasio, F. A.: 2001, *Icarus* **150**, 303

Fromang, S. and Nelson, R. P.: 2006, *ArXiv Astrophysics e-prints*

Fromang, S., Terquem, C., and Balbus, S. A.: 2002, *MNRAS* **329**, 18

Fromang, S., Terquem, C., and Nelson, R. P.: 2005, *MNRAS* **363**, 943

Gammie, C. F.: 1996, *ApJ* **457**, 355

Gladman, B.: 1993, *Icarus* **106**, 247

Goldreich, P. and Sari, R.: 2003, *ApJ* **585**, 1024

Goldreich, P. and Tremaine, S.: 1979, *ApJ* **233**, 857

Goldreich, P. and Tremaine, S.: 1980, *ApJ* **241**, 425

Goodman, J. and Rafikov, R. R.: 2001, *ApJ* **552**, 793

Haisch, Jr., K. E., Lada, E. A., and Lada, C. J.: 2001, *ApJ* **553**, L153

Hawley, J. F. and Balbus, S. A.: 1991, *ApJ* **376**, 223

Hawley, J. F. and Balbus, S. A.: 1992, *Bulletin of the American Astronomical Society* **24**, 1234

Holman, M., Touma, J., and Tremaine, S.: 1997, *Nature* **386**, 254

Jang-Condell, H. and Sasselov, D. D.: 2005, *ApJ* **619**, 1123

Johansen, A., Henning, T., and Klahr, H.: 2006, *ApJ* **643**, 1219

Johnson, E. T., Goodman, J., and Menou, K.: 2006, *ArXiv Astrophysics e-prints*

Klahr, H. and Kley, W.: 2006, *A&A* **445**, 747

Klahr, H. H. and Bodenheimer, P.: 2003, *ApJ* **582**, 869

Kley, W.: 1999, *MNRAS* **303**, 696

Kley, W.: 2000, *MNRAS* **313**, L47

Kley, W., Lee, M. H., Murray, N., and Peale, S. J.: 2005, *A&A* **437**, 727

Kley, W., Peitz, J., and Bryden, G.: 2004, *A&A* **414**, 735

Koller, J., Li, H., and Lin, D. N. C.: 2003, *ApJ* **596**, L91

Korycansky, D. G. and Papaloizou, J. C. B.: 1996, *ApJS* **105**, 181

Laughlin, G., Steinacker, A., and Adams, F. C.: 2004, *ApJ* **608**, 489

LeVeque, R. J.: 1998, *J. Comput. Phys.* **146**, 346

Li, H., Colgate, S. A., Wendroff, B., and Liska, R.: 2001, *ApJ* **551**, 874

Li, H., Finn, J. M., Lovelace, R. V. E., and Colgate, S. A.: 2000, *ApJ* **533**, 1023

Lin, D. N. C., Bodenheimer, P., and Richardson, D. C.: 1996, *Nature* **380**, 606

Lin, D. N. C. and Papaloizou, J.: 1979, *MNRAS* **186**, 799

Lin, D. N. C. and Papaloizou, J.: 1986a, *ApJ* **307**, 395

Lin, D. N. C. and Papaloizou, J.: 1986b, *ApJ* **309**, 846

Lin, D. N. C. and Papaloizou, J. C. B.: 1993, in E. H. Levy and J. I. Lunine (eds.), *Protostars and Planets III*, pp 749–835

Lovelace, R. V. E., Li, H., Colgate, S. A., and Nelson, A. F.: 1999, *ApJ* **513**, 805

Lubow, S. H. and D'Angelo, G.: 2006, *ApJ* **641**, 526

Lubow, S. H., Seibert, M., and Artymowicz, P.: 1999, *ApJ* **526**, 1001

Masset, F.: 2000a, *A&AS* **141**, 165

Masset, F. and Snellgrove, M.: 2001, *MNRAS* **320**, L55+
Masset, F. S.: 2000b, in G. Garzón, C. Eiroa, D. de Winter, and T. J. Mahoney (eds.), *Disks, Planetesimals, and Planets*, Vol. 219 of *Astronomical Society of the Pacific Conference Series*, pp 75–+
Masset, F. S.: 2001, *ApJ* **558**, 453
Masset, F. S.: 2002, *A&A* **387**, 605
Masset, F. S., D'Angelo, G., and Kley, W.: 2006a, *ApJ* **652**, 730
Masset, F. S., Morbidelli, A., Crida, A., and Ferreira, J.: 2006b, *ApJ* **642**, 478
Masset, F. S. and Ogilvie, G. I.: 2004, *ApJ* **615**, 1000
Masset, F. S. and Papaloizou, J. C. B.: 2003, *ApJ* **588**, 494
Mayor, M., Queloz, D., Marcy, G., Butler, P., Noyes, R., Korzennik, S., Krockenberger, M., Nisenson, P., Brown, T., Kennelly, T., Rowland, C., Horner, S., Burki, G., Burnet, M., and Kunzli, M.: 1995, *IAU Circ.* **6251**, 1
Mazeh, T., Krymolowski, Y., and Rosenfeld, G.: 1997, *ApJ* **477**, L103+
Menou, K. and Goodman, J.: 2004, *ApJ* **606**, 520
Meyer-Vernet, N. and Sicardy, B.: 1987, *Icarus* **69**, 157
Morohoshi, K. and Tanaka, H.: 2003, *MNRAS* **346**, 915
Murray, C. D. and Dermott, S. F.: 2000, *Solar System Dynamics*, Solar System Dynamics, by C.D. Murray and S.F. Dermott. ISBN 0521575974. Cambridge, UK: Cambridge University Press, 2000.
Narayan, R., Goldreich, P., and Goodman, J.: 1987, *MNRAS* **228**, 1
Nelson, A. F. and Benz, W.: 2003a, *ApJ* **589**, 556
Nelson, A. F. and Benz, W.: 2003b, *ApJ* **589**, 578
Nelson, R. P.: 2005, *A&A* **443**, 1067
Nelson, R. P. and Papaloizou, J. C. B.: 2002, *MNRAS* **333**, L26
Nelson, R. P. and Papaloizou, J. C. B.: 2003, *MNRAS* **339**, 993
Nelson, R. P. and Papaloizou, J. C. B.: 2004, *MNRAS* **350**, 849
Nelson, R. P., Papaloizou, J. C. B., Masset, F. S., and Kley, W.: 2000, *MNRAS* **318**, 18
Ogilvie, G. I.: 2001, *MNRAS* **325**, 231
Ogilvie, G. I. and Lubow, S. H.: 2002, *MNRAS* **330**, 950
Ogilvie, G. I. and Lubow, S. H.: 2003, *ApJ* **587**, 398
Paardekooper, S. . and Mellema, G.: 2006, *ArXiv Astrophysics e-prints*
Pandolfi, M. and D'Ambrosio, D.: 2001, *JCP* **166**, 271
Papaloizou, J. and Lin, D. N. C.: 1984, *ApJ* **285**, 818
Papaloizou, J. C. B.: 2002, *A&A* **388**, 615
Papaloizou, J. C. B.: 2005, *Celestial Mechanics and Dynamical Astronomy* **91**, 33
Papaloizou, J. C. B. and Larwood, J. D.: 2000, *MNRAS* **315**, 823
Papaloizou, J. C. B. and Nelson, R. P.: 2005, *A&A* **433**, 247
Papaloizou, J. C. B., Nelson, R. P., Kley, W., Masset, F. S., and Artymowicz, P.: 2006, *ArXiv Astrophysics e-prints*
Papaloizou, J. C. B., Nelson, R. P., and Snellgrove, M. D.: 2004a, *MNRAS* **350**, 829
Papaloizou, J. C. B., Nelson, R. P., and Snellgrove, M. D.: 2004b, *MNRAS* **350**, 829

Pierens, A. and Huré, J.-M.: 2005, *A&A* **433**, L37
Rafikov, R. R.: 2002, *ApJ* **572**, 566
Rasio, F. A. and Ford, E. B.: 1996, *Science* **274**, 954
Schäfer, C., Speith, R., Hipp, M., and Kley, W.: 2004, *A&A* **418**, 325
Shakura, N. I. and Sunyaev, R. A.: 1973, *A&A* **24**, 337
Snellgrove, M. D., Papaloizou, J. C. B., and Nelson, R. P.: 2001, *A&A* **374**, 1092
Stone, J. M. and Norman, M. L.: 1992, *ApJS* **80**, 753
Tanaka, H., Takeuchi, T., and Ward, W. R.: 2002, *ApJ* **565**, 1257
Tanigawa, T. and Lin, D. N. C.: 2005, in *Bulletin of the American Astronomical Society*, Vol. 37 of *Bulletin of the American Astronomical Society*, pp 684–+
Terquem, C. E. J. M. L. J.: 2003, *MNRAS* **341**, 1157
Toomre, A.: 1969, *ApJ* **158**, 899
Ward, W. R.: 1986, *Icarus* **67**, 164
Ward, W. R.: 1988, *Icarus* **73**, 330
Ward, W. R.: 1991, in *Lunar and Planetary Institute Conference Abstracts*, pp 1463–+
Ward, W. R.: 1992, in *Lunar and Planetary Institute Conference Abstracts*, pp 1491–+
Ward, W. R.: 1997, *Icarus* **126**, 261
Ward, W. R.: 2003, in S. Mackwell and E. Stansbery (eds.), *Lunar and Planetary Institute Conference Abstracts*, pp 1736–+
Winters, W. F., Balbus, S. A., and Hawley, J. F.: 2003, *ApJ* **589**, 543
Ziegler, U. and Yorke, H.: 1997, *Computer Physics Communications* **101**, 54
Zingale, M., Dursi, L. J., ZuHone, J., Calder, A. C., Fryxell, B., Plewa, T., Truran, J. W., Caceres, A., Olson, K., Ricker, P. M., Riley, K., Rosner, R., Siegel, A., Timmes, F. X., and Vladimirova, N.: 2002, *ApJS* **143**, 539